Self-Calibrating Rydberg Electrometer for Radio Frequency and Microwave Field Detection

Lingyun Chai

Shanghai, China

Bachelor of Science, Fudan University, 2016

A Dissertation submitted to the Graduate Faculty

of the University of Virginia in Candidacy for the Degree of

Doctor of Philosophy

Department of Physics

University of Virginia

August 2023

Abstract

Accurate detection and characterization of radio frequency (RF) and microwave (MW) electric fields are crucial capabilities for numerous scientific and practical applications. This dissertation describes a self-calibrating electromagnetic field sensor for measuring the amplitude and frequency spectrum of RF fields. The sensor employs Rydberg Rubidium atoms in a room temperature vapor cell and electromagnetically induced transparency (EIT) laser spectroscopy as an optical readout.

The electrometer utilizes non-resonant dressing of Rydberg atoms in combined RF and DC, low frequency (LF), or RF reference electric fields to exploit the exceptionally large field sensitivity (i.e. polarizability) of Rydberg atoms. In the presence of an unknown "signal" and known "reference" fields, the Rydberg excitation spectrum obtained through laser spectroscopy exhibits a primary Rydberg resonance feature Stark-shifted from the zero-field resonance. This primary resonance is flanked by subsidiary resonances (sidebands) whose splittings directly reflect the frequencies of the signal and reference fields.

Spectroscopic measurement of the shift of the primary Rydberg resonance, along with the ratio of the sideband to primary Rydberg resonance amplitudes, enables the determination of the spectral amplitude of the RF field. The instrument offers high sensitivity across a broad spectral range, and is not limited by a resonant or near-resonant atomic response.

Furthermore, it is self-calibrating and does not require detailed knowledge of the signal field frequency for effective operation. Measurements over a wide range of field

amplitudes can be accomplished with the same instrument using Rydberg states with larger principal quantum numbers and a large reference field for weak signal fields, and lower-n Rydberg states and direct AC Stark shift measurements with no reference for the strongest signal fields. Characterization of higher frequency fields (e.g. in the microwave regime) can be accomplished, without requiring rapid laser scanning over a wide frequency range, through the use of low-n Rydberg states and a high frequency reference.

Dedication

To Mom and Dad.

For the endless love, support and encouragement.

Acknowledgments

First and foremost, my special thanks go to my advisor Prof. Bob Jones for his guidance and advice throughout the years, not only limited to the daily research life but also the logical thinking and scientific ethics. I am truly grateful for his patience in guiding me to understand every detail of the theoretical calculations and experiment results. He not only taught me how to operate complicated instruments but also showed me how to fix failing devices. It is fortunate for me to receive his guidance every week during my entire Ph.D. years, as well as the financial support through the research assistantship, including additional funding for attending different academic conferences. The successful completion of this dissertation would not have been possible without Prof. Jones' dedicated efforts in grammar checking, language polishing, error correction, and engaging in thoughtful discussions.

I would like to express my gratitude to Prof. Thomas Gallagher, Prof. Kevin Lehmann and Prof. Peter Schauss for their valuable insights and time serving on my Ph.D dissertation committee. I would like to thank Prof. Schauss again for the commitment in serving on my research committee every year to encourage and keep me on the correct track towards the Ph.D degree. Thanks again to Prof. Gallagher for lending me essential experimental apparatus and engaging in the discussion about the experiment operation.

It is blessed for me to have so many young and talented colleagues in the Jones group. Chengxing He, with whom I shared five years in the lab, taught me how

to operate and design the experimental apparatus, and how to program in R and Python. The weekly Journal club, organized by Sachin Sharma, Ali Azarm, Sanjay Khatri, Chengxing He and myself, provided heated discussion on the frontier of the Physics research and enhanced our understanding of the fundamentals of individual research projects. All of them shared a lot of information with me on finding jobs/-postdocs and how to choose a suitable career path.

I would also like to thank Rick Marshall for maintaining a stable lab environment and Peter Cline for providing organizational and administrative support throughout the Ph.D program. I also had fruitful discussions with Liyu Liu from Prof. Schauss' group, particularly regarding a variety of experiment details.

Last but not least, I would like to thank all of my friends. They are all incredible individuals who have made my daily life vivid in the past seven years in Charlottsville. I owe a debt of gratitude to my parents and my girlfriend in my hometown, Shanghai, for providing the mental support from the very beginning to the very end of this journey.

Contents

List of Figures

List of Tables

List of Abbreviations

AT Autler-Townes

CW continuous-wave

ECDL External cavity diode laser

EIT Electromagnetically Induced transparency

HVAC Heating, ventilation and air conditioning

LF Low frequency

MW Microwave

PID Proportinal-integral-derivative

RF Radio frequency

SHG Second harmonic generation

TA Tapered amplifier

Chapter 1

Introduction

Electromagnetic radiation in the radio frequency (RF), microwave (MW), mm-wave, and THz regimes is the basis for much of modern communication as well as remote sensing and numerous other applications. Accordingly, accurate detection and characterization of such fields is an essential and enabling capability. In this dissertation, we refer to electromagnetic fields with frequencies ranging from 10 MHz to 1 GHz as RF fields, and fields with frequencies ranging from 1 GHz to 1000 GHz as MW fields.

Figure 1.1: Tek P6139A high voltage[1] probe is used for RF frequency and amplitude detection.

RF and MW field detection has traditionally been accomplished with classical sensors and detectors, such RF antennas and MW dishes. There are, however, problems with these traditional detectors. First one is that they can be very susceptible to environmental noise. Second is that they can be invasive and influence the fields that they aim to detect. Yet another one is that accurate calibration is needed for differ-

ent frequencies within the detection bandwidth, and that calibration can also vary with environmental conditions and proximity of the detector to other macroscopic objects in the vicinity. As an example, the RF voltage probes from Tektronix[2] were used to measure the RF voltage across the pair of parallel conducting plates that were employed to create a uniform electric field for the atom-based electrometer. Comparison of the direct probe measurements with the field-response of the Rydberg atoms reveals the substantial variation in the probe calibration that is not accurately reproduced from the published frequency response curves.

Unlike macroscopic sensors, atoms sense local fields on the smallest scales and are inherently identical detectors. Therefore, issues associated with manufacturing variations, aging electronics, and proximity effects can be eliminated.

The atom-based RF/MW electrometer we have developed differs from those recently demonstrated by others in that it is based on non-resonant interactions and, therefore, is inherently broadband and does not require a detailed *prior* knowledge of the frequency of the radiation to be measured. Moreover, it is self-calibrating in any experimental configuration. Although it is not as sensitive as approaches based on Rydberg resonance, it exploits non-linear field mixing of weak signal fields with a stronger reference to enhance its sensitivity which is ultimately limited by the signal to noise of the laser-based EIT absorption spectroscopy.

Before describing in detail the electrometer approach and apparatus, we first review some key properties of Rydberg atoms, and relevant aspects of EIT absorption spectroscopy.

1.1 Atomic and SI units

Atomic units are a system of natural units of measurement which are commonly used for atomic physics and chemistry[3]. Atomic units are defined by setting the values of the reduced Planck constant, elementary charge, Bohr radius, and electron mass to unity[4].

$$\hbar = e = a_0 = m_e = 1 \tag{1.1}$$

From this definition, other units such as energy, time, electric field strength and polarizability can be defined on a scale relevant to typical atomic parameters and processes. Quantities in this dissertation can be converted between SI and atomic units using Table 1.1.

Atomic Unit	SI value
Length	$5.29188210903(80) \times 10^{-11}$m
Time	$2.4188843265857(47) \times 10^{-17}$s^{-1}
Energy	$4.3597447222071(85) \times 10^{-18}$J
Charge	1.602188×10^{-19}C
Electric field	$5.14220674763(78) \times 10^{11} V \cdot$m^{-1}
Electric dipole moment	$8.4783536255(13) \times 10^{-30} C \cdot$m

Table 1.1: Conversion factors for typical atomic units[4].

1.2 Rydberg Atoms

Rydberg atoms are atoms in which one electron is excited to a state with a large principal quantum number ($n > 10$)[5]. In the experiments discussed in this dissertation, the outermost valence electron of an individual ^{85}Rb atom ($5s$ ground state) is excited to an $n \approx 30$ state. Due to the large spatial extent of the electron orbitals and their correspondingly small binding energies, Rydberg atoms have exaggerated properties that scale with powers of n. Among the properties of interest for this dissertation are electric polarizabilities (n^7) for the specific Rydberg states used in the experiments.

Property	n Dependence
Binding energy	n^{-2}
Orbital radius	n^2
Energy between adjacent n states	n^{-3}
Dipole moment	n^2
Radiative lifetime	n^3
Polarizability	n^7

Table 1.2: Properties of Rydberg atoms[5].

1.2.1 Quadratic Stark Shift

The response of the Rydberg atoms under electrical fields are the key aspect for further RF field measurement and characterization. When an external DC electric field of strength F is presented, an atom in the area becomes polarized in the field. If the state of the atom is not degenerate, the energy E acquires an additional energy $\Delta_E(F)$, so its energy in such external field is given by $E(F) = E + \Delta_E(F)$.

If the state of the atom is degenerate with an energy E_{nlm}, where n is the principle quantum number, l is the orbital quantum number and m is the magnetic quantum

number, the state experiences splitting in the electric field into 2l+1 components, since the sub levels corresponding to different values of m acquire different additional energies $\Delta_E(F)$ in the field.

For hydrogen atoms and highly exited hydrogen-like (Rydberg) states of many electron atoms, the external electric field induces a dipole moment when F is small,

$$d_{nlm} = \alpha_{nlm} F \tag{1.2}$$

Here α_{nlm} presents the static polarizability of the atom in the state with the given quantum numbers. The additional energy acquired by hydrogen-like atom in an external field can be written as,

$$\Delta_E(F) = -\frac{1}{2}\alpha_{nlm} F^2 \tag{1.3}$$

where α_{nlm} will be determined by the calculated Stark Map of the Rydberg states we use for RF field detection.

Calculations of the energy shift of ^{85}Rb atoms due to the DC Stark effect were done for several of the experiments and the techniques used can be found in the Starkr package by former group member Brian Richards[6] and Alkali.ne Rydberg Calculator by C.S. Adams[7]. Two plots of quadratic shift are shown in Fig. 1.2 here representing two Rydberg states used in the following experiments.

The polarizability of each Rydberg state is then calculated by the quadratic fitting of the Stark shift vs the external fields as in Fig. 1.2. The range of the external fields need to be limited to avoid the states crossing and mixing.

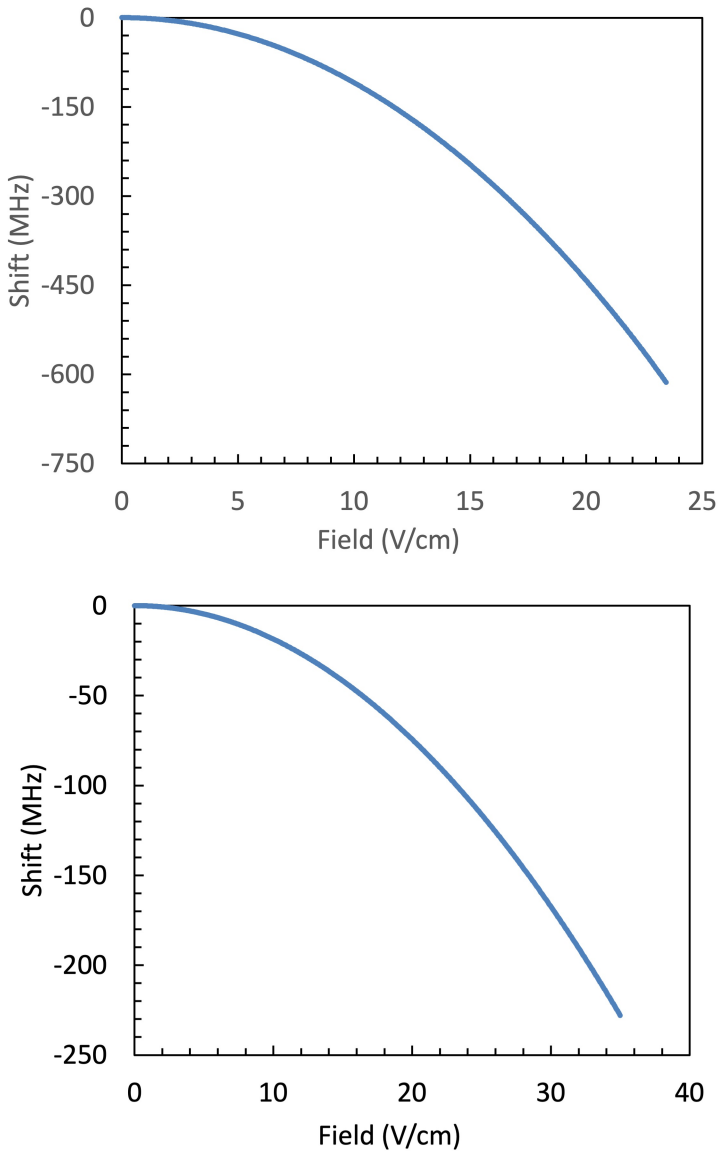

Figure 1.2: Stark map of target state of 85 Rubidium, calculated by Starkr package written in R-language[6]. (top) The $32s$ state polarizability is 2.19MHz/(V/cm)^2 with the field range of 0–24V and (bottom) the $25s$ state polarizability is 0.372MHz/(V/cm)^2 with the field range of 0–35V.

1.3 Field sensing with Rydberg states

The dipole matrix elements between Rydberg states of the same principal quantum number are typically 100 to 1000 times greater than that of the D2 transitions in alkali atoms, scaling as n^2. This property makes Rydberg atoms sensitive to electromagnetic radiation throughout the frequency range spanned by intra-manifold Rydberg-Rydberg state transitions, most notably in the Microwave regions, explored as the new quantum platform of RF and MW detection.

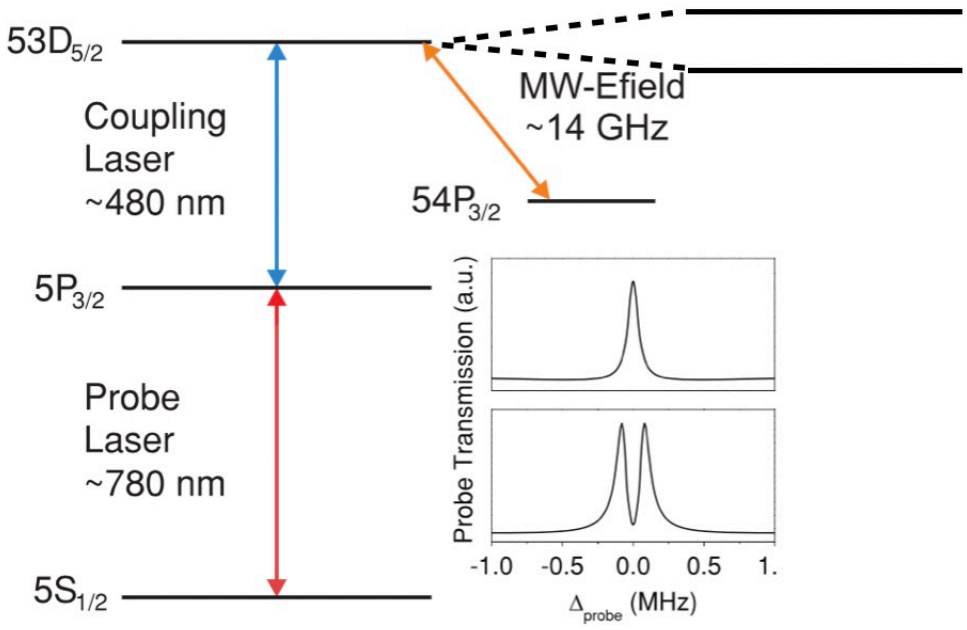

Figure 1.3: Level schemes for microwave electric field sensing[8]. A typical laser configuration for microwave electric field sensing using Rubidium. A coupling laser at 480nm is used in conjunction with a probe laser at 780nm to observe electromagnetically induced transparency. The transmission of the probe laser reflects the influence that a MW field, resonant with a Rydberg-Rydberg transition, has on the upper state of the EIT system. For strong MW fields the coupled Rydberg levels undergo a standard Autler-Townes (AT) splitting, characterized by the Rabi frequency which is proportional to the product of the MW field amplitude and the atomic transition dipole moment.

Rydberg atoms are extremely sensitive to incident radiation fields (MHz-THz) capable of driving resonant dipole-allowed transitions between electronic states. If the field is sufficiently strong, each of the coupled levels is split into an Autler-Townes doublet. This splitting can be readily detected through a variety of Doppler-free absorption spectroscopies including those based on electromagnetic induced transparency (EIT).

Atom-based electromagnetic field sensors which utilize Rydberg states, as introduced above, operate at room temperature and use alkali atoms contained in a vapor cell to detect electromagnetic fields[8]–[11].

The frequency splitting in the Rydberg states doublet corresponds to the Rabi frequency for the Rydberg-Rydberg resonance in the MW field. The Rabi frequency Ω is proportional to the product of the RF/MW field amplitude and the transition dipole moment.

$$2\pi\Delta f = \Omega = \frac{\vec{F}_{rf} \cdot \vec{d}}{\hbar} \tag{1.4}$$

where $\vec{F}_{rf}$ is the vector electric field amplitude and $\vec{d}$ is the Rydberg transition dipole moment.

Assuming a resonant transition can be found that matches the RF or MW frequency to be measured (this can generally be accomplished via Stark tuning of Rydberg states), and the relevant (Stark-tuned) transition dipole moment has been measured or calculated, then the RF or MW field amplitude can be extracted from spectroscopic measurements of the Autler-Townes splitting (or, in cases where the splitting is not resolved within the transition lineshape, from changes in the resonance lineshape). Numerous groups have developed different variants of this resonant Rydberg electrometry scheme, with field sensitivities limited by laser shot noise, atomic colli-

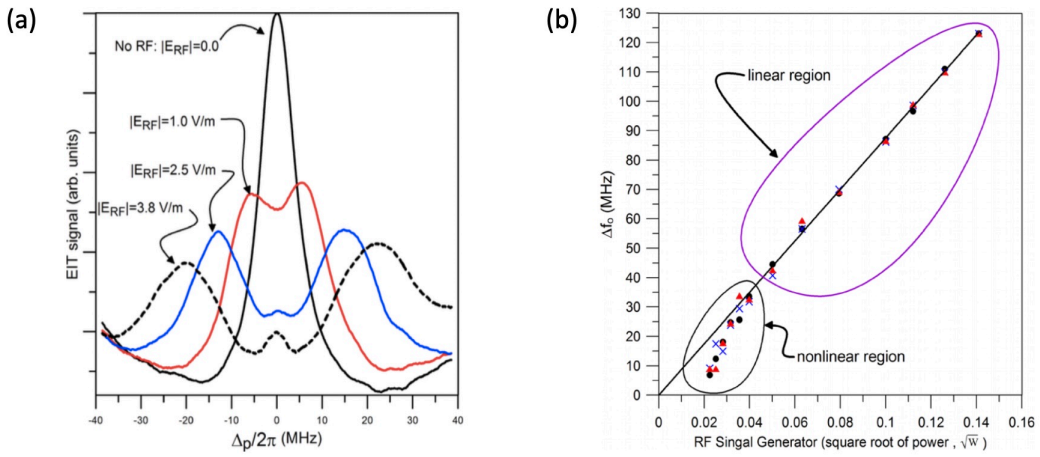

Figure 1.4: Experimental data (from [11]) for RF field detection through Rydberg EIT spectroscopy. (a) EIT signal as a function of probe laser detuning Δ_p. (b) Square root of power $\sqrt{W}$ on the x-axis is proportional to the applied RF E-Field[11].

sions, transit time broadening, and blackbody radiation, as well as residual Doppler shifts of the EIT scheme. Use of amplitude modulation[8], frequency modulation[12], homodyne[9] and heterodyne[13] detection has enabled laser shot-noise-limited performance.

In this thesis, we present a different technique for measuring the amplitude and frequency of radio-frequency fields. Like the resonance-based approach described above, the method utilizes Rydberg atoms in a vapor cell as a detection medium, and electromagnetically induced transparency (EIT) spectroscopy as an optical readout. Unlike the previous schemes[8]–[11] that rely on resonant coupling between Rydberg states, our electrometer is based on non-resonant dressing of the Rydberg atoms in mixed signal (RF/MW) and strong reference (DC, LF, RF/MW) electric fields.

1.4 Electromagnetically Induced transparency

Electromagnetically induced transparency (EIT) is a powerful high-resolution spectroscopic tool for measuring the energies of atomic Rydberg states (particularly low angular momentum Rydberg states that can be optically coupled to low-lying excited states) and level shifts caused by electric fields or other external interactions[14].

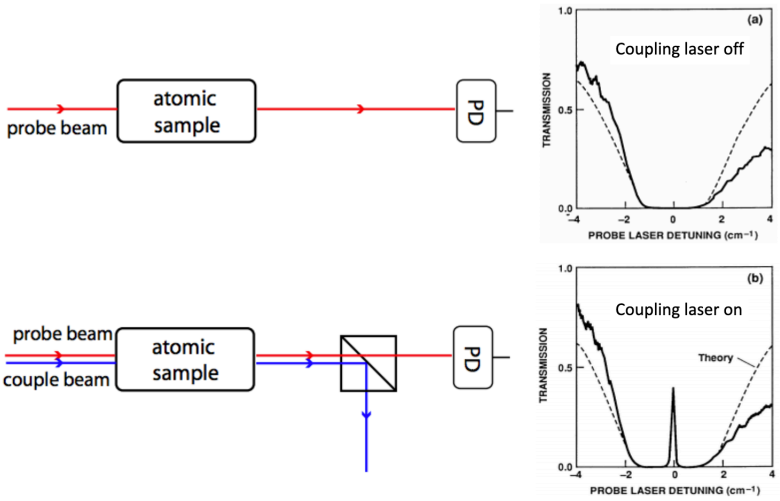

Figure 1.5: First observation of electromagnetically induced transparency in 1995 [15].

EIT spectroscopy is based on the interaction of two optical fields, the probe and coupling lasers, with a three level system, as shown in Fig. 1.6. We can write the laser-dressed interaction Hamilton for the three level system in terms of the relevant Rabi frequencies, $\Omega_{p,c} = \vec{d_{p,c}} \cdot \vec{F_{p,c}}/\hbar$, where $d_{p,c}$ are the transition electronic dipole

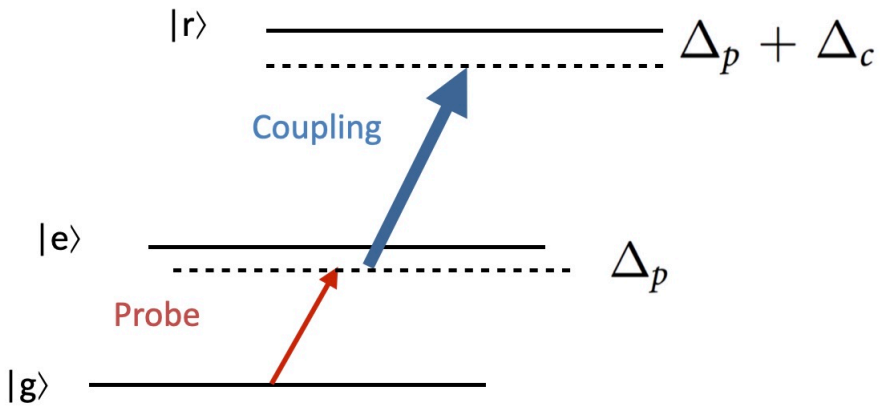

Figure 1.6: Energy diagram of a three level ladder system dressed with probe and coupling lasers.

moments for the respective transitions, and F is the laser field amplitude:

$$\begin{aligned} H &= H_0 + V_1 + V_2 \\ H_0 &= \hbar\omega_g \left|g\right\rangle \left\langle g\right| + \hbar\omega_e \left|e\right\rangle \left\langle e\right| + \hbar\omega_r \left|r\right\rangle \left\langle r\right| \\ V_1 &= \frac{\hbar}{2}\Omega_p e^{-i\omega_p t} \left|e\right\rangle \left\langle g\right| + H.c. \\ V_2 &= \frac{\hbar}{2}\Omega_c e^{-i\omega_c t} \left|r\right\rangle \left\langle e\right| + H.c. \end{aligned} \tag{1.5}$$

Here, ω_p and ω_c are the laser frequencies corresponding to the respective transitions. The rotating-wave approximation is applied for the interaction terms, neglecting terms that lead to rapid phase variations in the transition amplitudes.

The resulting Hamiltonian can be written in matrix form as,

$$H = \frac{\hbar}{2}\begin{pmatrix} 2\omega_g & \Omega_p e^{-i\omega_p t} & 0 \\ \Omega_p^* e^{i\omega_p t} & 2\omega_e & \Omega_c e^{-i\omega_c t} \\ 0 & \Omega_c^* e^{i\omega_c t} & 2\omega_r \end{pmatrix} \tag{1.6}$$

The approximate Hamiltonian in a dressed- state basis corresponding to the ground-

state, the excited state minus one probe laser photon, and the Rydberg state minus one coupling laser photon and one probe laser photon, in the rotating frame is,

$$\tilde{H} = \frac{\hbar}{2}\begin{pmatrix} 0 & \Omega_p & 0 \\ \Omega_p^* & 2\Delta_p & \Omega_c \\ 0 & \Omega_c^* & 2(\Delta_p + \Delta_c) \end{pmatrix} \tag{1.7}$$

where the laser detunings are defined as $\Delta_p = \omega_p - (\omega_e - \omega_g)$ and $\Delta_c = \omega_c - (\omega_r - \omega_e)$. For the experimental condition of a scanning coupling laser with the probe laser locked to the $|g\rangle \rightarrow |e\rangle$ resonance ($\Delta_p = 0, \Delta_c = \Delta$), the eigenstates of the dressed three-level system are,

$$\begin{aligned} |\psi_0\rangle &= A_{g0}\,|g\rangle + A_{e0}\,|e\rangle + A_{r0}\,|r\rangle \\ |\psi_1\rangle &= A_{g1}\,|g\rangle + A_{e1}\,|e\rangle + A_{r1}\,|r\rangle \\ |\psi_2\rangle &= A_{g2}\,|g\rangle + A_{e0}\,|e\rangle + A_{r2}\,|r\rangle \end{aligned} \tag{1.8}$$

where the A_{ij} are determined by diagonalizing the Hamiltonian (Eq. 1.7) and depend on Δ_c, Ω_c, and Ω_p with $\Delta_p = 0$. We can understand the effect of the coupling laser on the probe transition as Δ_c is scanned (our experimental observable) by inspection of the eigenvalues and eigenstate compositions as a function of Δ_p (relative to Ω_p). As examples, the eigenvalues of states 0,1,2 as a function of Δ_c, for particular values of Ω_c and Ω_p, are shown in Fig. 1.7.

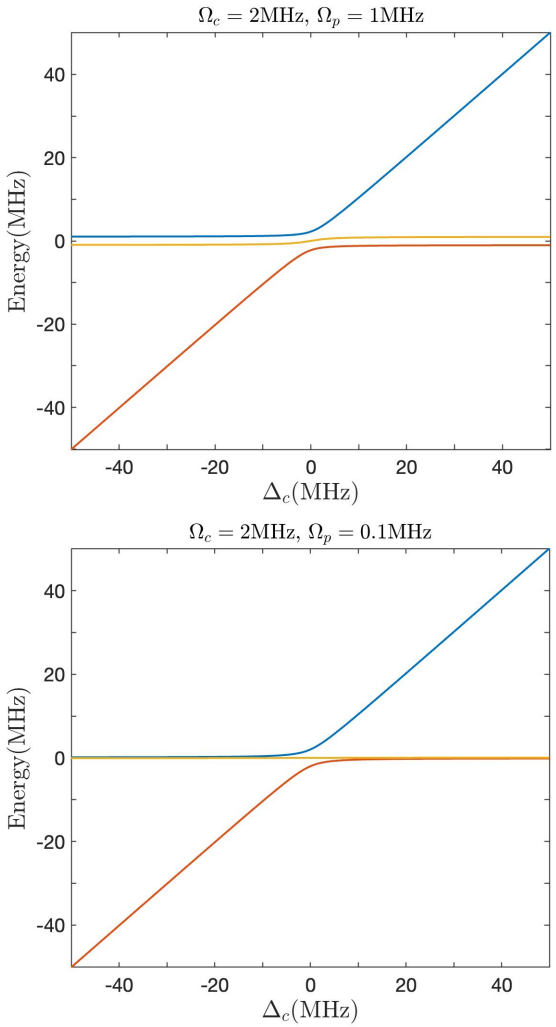

Figure 1.7: Dressed eigenstates as functions of the coupling laser detuning Δ_c. The eigenvalues of states 0,1,2 in Eq. 1.8 are plotted as the blue, yellow, and orange lines. (Top)The Rabi frequencies of the probe laser and coupling laser are set to be comparable to each other Ω_c= 2MHz and Ω_p =1MHz. At large coupling laser detuning (relative to Ω_c), the three level system appears as a strongly-coupled doublet involving equal admixtures of the ground and excited state (split by the Rabi frequency of the probe laser, Ω_p) and a third level, the Rydberg state, which is essentially decoupled from the other levels. Near resonance, for detunings $|\Delta_c| \ll \Omega_c$, all three dressed states are strongly coupled. (Bottom)The Rabi frequencies of the probe laser and coupling lasers are set to $\Omega_c = 2$MHz and $\Omega_p = 0.1$MHz. In this weak probe situation (like that used in the experiment), the case is similar to that in top figure for $|\Delta_c| \gg \Omega_c$. However, for small detunings with $|\Delta_c| \ll \Omega_c$ the excited state and Rydberg state are strongly coupled with each other, creating eigenstates that are decoupled from the ground state, the latter exhibiting essentially zero energy shift. In this regime, the ground state does not couple to the excited state, and there is no (or relatively little) probe laser absorption.

The detailed expressions for the admixture coefficients A_{mn} are somewhat complicated in general, but we can obtain simple expressions for them in the far-detuned and/or near-resonance limits. When $|\Delta_c| \ll \Omega_c$, the eigenstates are approximately

$$\begin{aligned} |\psi_0\rangle &= 1/\sqrt{2}\,|g\rangle + 1/\sqrt{2}\,|e\rangle \\ |\psi_1\rangle &= 1/\sqrt{2}\,|g\rangle - 1/\sqrt{2}\,|e\rangle \\ |\psi_2\rangle &= |r\rangle \end{aligned} \tag{1.9}$$

Similarly, when $|\Delta_c| \gg \Omega_c$, the eigenstates are approximately

$$\begin{aligned} |\psi_0\rangle &= |r\rangle \\ |\psi_1\rangle &= 1/\sqrt{2}\,|g\rangle + 1/\sqrt{2}\,|e\rangle \\ |\psi_2\rangle &= 1/\sqrt{2}\,|g\rangle - 1/\sqrt{2}\,|e\rangle \end{aligned} \tag{1.10}$$

The three eigenstates can be seen as a coupled two-level system with an extra, uncoupled state when the coupling laser is far detuned. The transition probability between the ground and excited state (related to the laser absorption as the experimental observable) can be modeled as the incoherent sum of the product of the ground state population and excited state population in each of the three eigenstates, $\sum(A_{gi}A_{ei})^2$. This model implicitly takes into account decoherence between the eigenstates due to spontaneous emission, which is not included in the Hamiltonian. For large coupling laser detunings the excited state population has a maximum value of 1/2, with zero Rydberg state population, representing maximum probe laser absorption.

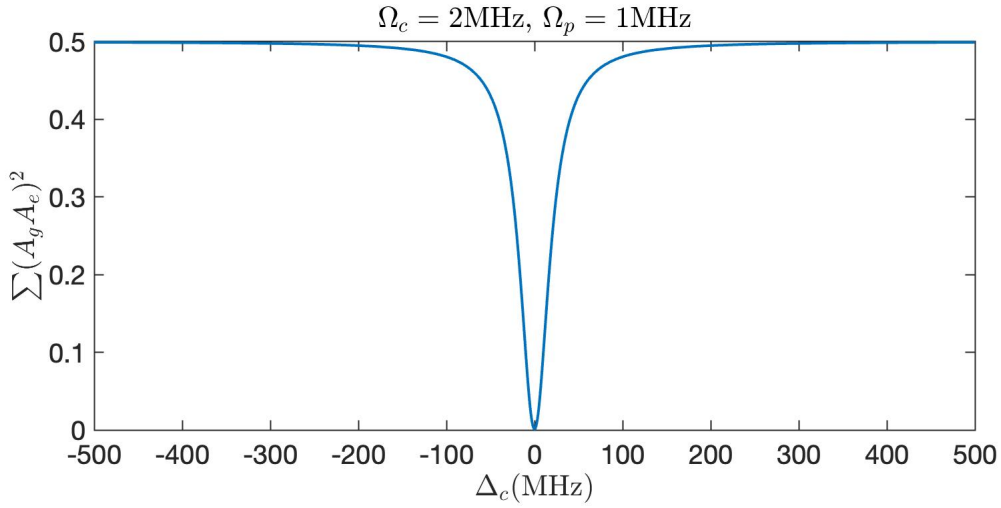

Figure 1.8: Semi-quantitative depiction of the net population in the excited state (and probe laser absorption) as a function of coupling laser detuning Δ_c. The population calculation is based on incoherent addition of the contributions from each dressed eigenstate (the lack of coherence is due to dephasing caused by spontaneous emission between the excited and ground states for real atoms, not explicitly accounted for in the model Hamiltonian), assuming: i) that each eigenstate is populated according to the square of its ground-state admixture coefficient; and ii) that the excited state population within each eigenstate is given by the square of its admixture coefficient. The Rabi frequencies of the probe and coupling lasers are set to $\Omega_c = 2$MHz and Ω_p =1MHz, respectively. When $\Delta_c = 0$, no population appears in the excited state, i.e. there is no probe laser absorption.

For $\Delta_c \ll \Omega_c$ and $\Omega_p \ll \Omega_c$, the eigenstates become,

$$\begin{aligned} |\psi_0\rangle &\approx |g\rangle \\ |\psi_1\rangle &\approx \frac{1}{2}(|r\rangle + |e\rangle) \\ |\psi_2\rangle &\approx \frac{1}{2}(|r\rangle - |e\rangle) \end{aligned} \tag{1.11}$$

Here, the excited and Rydberg states are strongly coupled with each other, and decoupled from the ground state. Accordingly, the product of the ground and excited state admixture coefficients within each eigenstate is negligibly small. The model predicts zero excited state population reflecting minimal probe laser absorption. This

electromagnetically induced transparency is due to the modification of the eigenstate composition when the strength of the optical coupling between the excited and Rydberg states far exceeds that between the ground and excited states. During a frequency scan of the coupling laser (with the probe laser locked on resonance), the probe absorption experiences a minimum (i.e. a transparency maximum) when the coupling laser frequency matches the excited-state to Rydberg resonance. Therefore, EIT spectroscopy is a convenient and sensitive tool for measuring shifts in Rydberg energy levels due to external fields[14].

EIT can also be viewed as the result of destructive quantum interference involving two paths to the excited state, $|g\rangle \rightarrow |e\rangle$ and $|r\rangle \rightarrow |e\rangle$. Since there is no excited-state population, there is no probe light absorption[16].

1.4.1 EIT via Optical-Bloch Equations

A more complete, and quantitatively accurate description of EIT requires that spontaneous emission be properly taken into account. To do this, one can solve the master equation for the density matrix ρ. The following outlines that approach, and provides a brief derivation of the optical susceptibility relevant to the probe laser absorption in the EIT scheme, based on several EIT review papers[16], [17].

The optical-Bloch equations describing the dynamics in a driven three-level system are derived from the master equation,

$$\dot{\rho} = -\frac{i}{\hbar}[\hat{H}, \rho] + \mathcal{L}\rho \tag{1.12}$$

where $\mathcal{L}$ represents the phenomenological decay of the intermediate state and dephas-

ing of the Rydberg state, and the density matrix ρ is defined as,

$$\rho = |\psi\rangle \langle\psi| \tag{1.13}$$

For a three-level atomic system in the state,

$$|\psi\rangle = A_g |g\rangle + A_e |e\rangle + A_r |r\rangle \tag{1.14}$$

The density matrix is:

$$\rho = \begin{pmatrix} \rho_{gg} & \rho_{ge} & \rho_{gr} \\ \rho_{eg} & \rho_{ee} & \rho_{er} \\ \rho_{rg} & \rho_{re} & \rho_{rr} \end{pmatrix} = \begin{pmatrix} A_a A_a^* & A_a A_e^* & A_a A_r^* \\ A_e A_a^* & A_e A_e^* & A_e A_r^* \\ A_r A_a^* & A_r A_e^* & A_r A_r^* \end{pmatrix} \tag{1.15}$$

We introduce new, slowly evolving, matrix elements in the rotating frame using a unitary transformation,

$$\begin{aligned} \rho_{ge} &= \tilde{\rho}_{ge} e^{-i\omega_p t} \\ \rho_{er} &= \tilde{\rho}_{er} e^{-i\omega_c t} \\ \rho_{gr} &= \tilde{\rho}_{er} e^{-i(\omega_c + \omega_p) t} \end{aligned} \tag{1.16}$$

In steady state, $\dot{\rho} = 0$, this yields the three-level optical Bloch equations

$$\begin{aligned} \dot{\tilde{\rho_{eg}}} &= -i\frac{\Omega_p}{2}(\tilde{\rho_{gg}} - \tilde{\rho_{ee}}) + i\Delta_p \tilde{\rho_{eg}} - i\frac{\Omega_c}{2}\tilde{\rho_{rg}} - \gamma\tilde{\rho_{eg}} = 0 \\ \dot{\tilde{\rho_{rg}}} &= i\frac{\Omega_p}{2}\tilde{\rho_{re}} + i(\Delta_p + \Delta_c)\tilde{\rho_{rg}} - i\frac{\Omega_c}{2}\tilde{\rho_{eg}} - \gamma_r\tilde{\rho_{rg}} = 0 \\ \dot{\tilde{\rho_{re}}} &= -i\frac{\Omega_c}{2}(\tilde{\rho_{ee}} - \tilde{\rho_{rr}}) + i\Delta_c \tilde{\rho_{re}} + i\frac{\Omega_p}{2}\tilde{\rho_{rg}} - \gamma'\tilde{\rho_{re}} = 0 \end{aligned} \tag{1.17}$$

where γ, γ' are the decoherence rates for the driven transitions (ground to excited state and excited to Rydberg state). γ_r is the decoherence rate of the Rydberg state

due to two-photon transition (ground to Rydberg state) $\ll \gamma$. Spontaneous emission is assumed to be the main decay mechanism for the excited state so $\gamma = \Gamma/2$, i.e. half of the spontaneous decay rate of the excited state. For scale, in our experiments with Rubidium $5P_{3/2}$ as the excited state, $\gamma = \Gamma/2 = 2\pi \times 3\text{MHz}$.

In the weak probe limit ($|\Omega_p| \ll \gamma$), there is negligible population build-up in the excited state for any coupling laser detuning, therefore, we can assume $\rho_{re} = 0$ and

$$\tilde{\rho_{eg}} = -\frac{i(\gamma_r - i(\Delta_p + \Delta_c))\Omega_p/2}{(\gamma - i\Delta_p)(\gamma_r - i(\Delta_p + \Delta_c)) + \Omega_c^2/4} \tag{1.18}$$

The matrix element ρ_{eg} is related to the complex susceptibility through the polarization relation,

$$P = \frac{1}{2}\epsilon_0 E_p[\chi e^{-i\omega_p t} + c.c.] = -N d_{ge}(\tilde{\rho_{ge}} e^{-i\omega_p t} + c.c.) \tag{1.19}$$

where d_{ge} is the dipole moment of the ground state to excited state transition, N_0 is the atom number density, and we obtain the optical susceptibility that is relevant to the experimental absorption [17],

$$\chi(\Delta_p, \Delta_c) = -2\frac{N_0 d_{ge}^2}{\epsilon_0 \hbar}\frac{\tilde{\rho_{eg}}}{\Omega_p} = \chi_{2level} \times [1 - \frac{\Omega_c^2/4}{(\gamma - i\Delta_p)(\gamma_r - i(\Delta_p + \Delta_c) + \Omega_c^2/4}] \tag{1.20}$$

where χ_{2level} is the susceptibility for the two-level system in the weak probe limit by

$$\chi_{2level} = \frac{N_0 d_{ge}^2}{\epsilon_0 \hbar}\frac{i}{\gamma - i\Delta_p} \tag{1.21}$$

When both lasers are tuned to resonance, minimum absorption is obtained,

$$\chi(\Delta_p = 0, \Delta_c = 0) = \chi_{2level}[1 - \frac{\Omega_c^2}{4\gamma_r\gamma + \Omega_c^2}] \tag{1.22}$$

For an ensemble of atoms at non-zero temperature, the detunings are different for different atoms in the ensemble, due to the Doppler effect. In the standard configuration where the probe and coupling lasers counterpropagate through the sample, the detunings of the two lasers for an atom moving with velocity $\vec{v}$ become,

$$\begin{aligned} \Delta_p &\to \Delta_p + k_p v \\ \Delta_c &\to \Delta_c - k_c v \end{aligned} \tag{1.23}$$

where $k_{p,c} = \dfrac{2\pi}{\lambda_{p,c}}$ are the wave numbers for two lasers, and v is the component of the atom's velocity parallel velocity to the probe laser propagation direction.

To determine the total susceptibility for the atomic sample we integrate over the Boltzmann velocity distribution,

$$\begin{aligned} &\chi(\Delta_p, \Delta_c) = -2\frac{N_0 d_{ge}^2}{\epsilon_0\hbar}\frac{\tilde{\rho_{eg}}}{\Omega_p} \\ &= \int \frac{i(\gamma_r - i(\Delta_p + \Delta_c + k_p v - k_c v))}{(\gamma - i(\Delta_p + k_p v))(\gamma_r - i(\Delta_p + \Delta_c + k_p v - k_c v)) + \Omega_c^2/4} \cdot \\ &\frac{N_0 d_{ge}^2}{\epsilon_0\hbar}\sqrt{\frac{m}{2\pi k_B T}} e^{-\frac{mv^2}{2k_B T}} dv \end{aligned} \tag{1.24}$$

where k_B is the Boltzmann constant, T is the temperature of the Rubidium cell, and m is the mass of Rubidium atom.

In general, the measured power of the transmitted probe beam, which is proportional

to the probability of probe transmission through the vapor cell is given by

$$P = P_0 e^{-\frac{2\pi L}{\lambda_p} Im[\chi(\Delta)]} = P_0 e^{-\alpha L} \tag{1.25}$$

where P_0 is the power of the probe beam entering the cell and L is the length of the cell. In our experiments, the probe absorption is very small, and we can approximate $(P_0 - P)/P_0 \simeq \alpha L$.

Fig. 1.9 shows the imaginary part of the susceptibility vs coupling laser detuning for different probe laser detunings and coupling laser Rabi frequencies. The upper graph in Fig. 1.9 shows the case for an ensemble of stationary atoms at zero temperature, predicting a true zero in the on-resonance absorption, with a broadening of the transparency dip for increasing coupling laser intensity. As Eq. 1.22 indicates, in the strong coupling regime $\Omega_c^2 \gg 4\gamma_r\gamma$, the EIT linewidth is $\Omega_c^2/(4\gamma)$, which differs from the primary result based on the Hamiltonian model where the impact of spontaneous decay was not quantitatively included (in Fig. 1.8).

The lower graph in Fig. 1.9 shows the predicted susceptibility assuming a room temperature Maxwell-Boltzmann velocity distribution. In this case, the susceptibility is not equal to zero on resonance and both the width and magnitude of the transparency window depend on Ω_c.

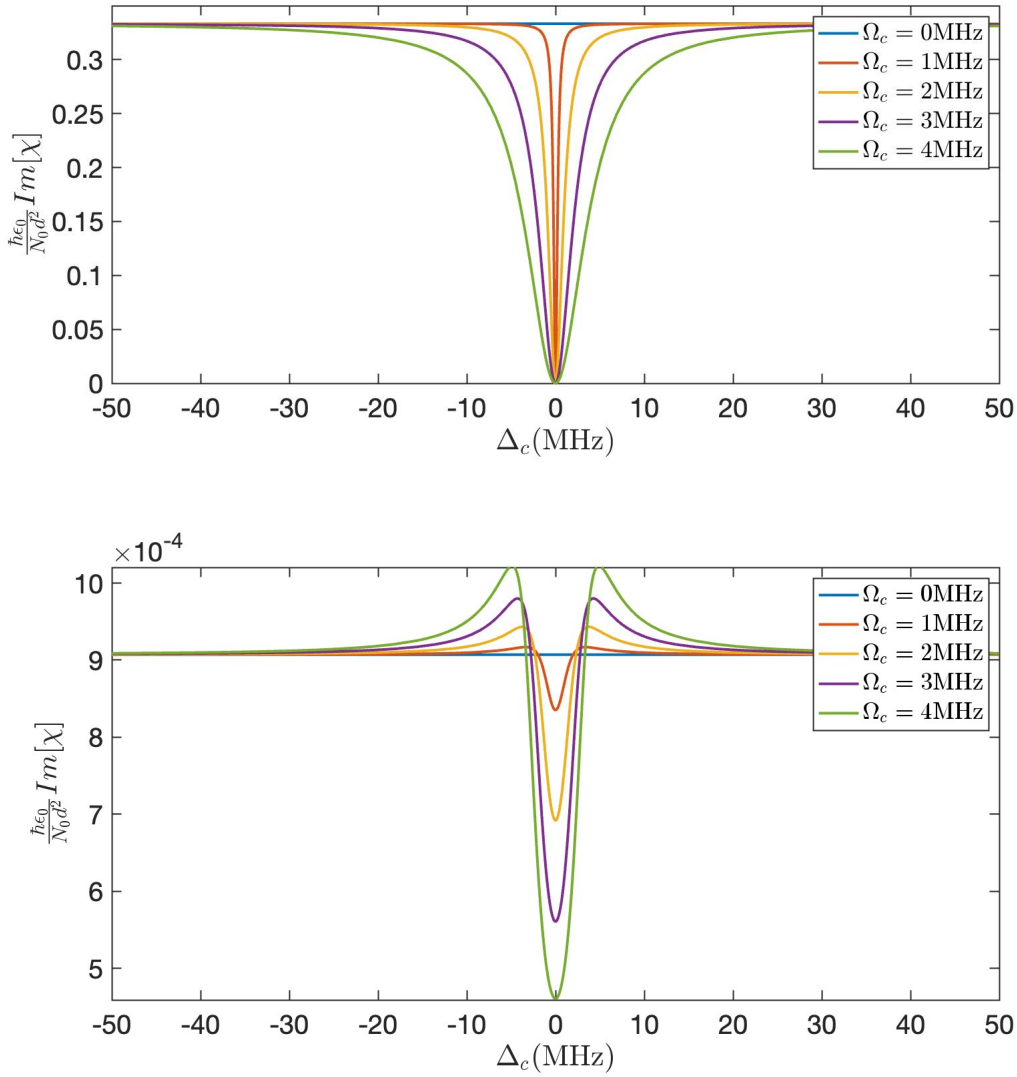

Figure 1.9: Imaginary part of the susceptibility (χ) as a function of coupling laser detuning Δ_c, for $\Delta_p = 0$. The probe transition coherence decay rate is $\gamma = 3$MHz. The two-photon decay rate, $\gamma_r \approx 10^{-6}$MHz, is neglected. (Top) Imaginary part of susceptibility vs coupling laser detuning for different coupling Rabi frequencies and stationary atoms. This shows the transparency window at the two photon resonance condition. Any increase in the coupling Rabi frequency solely broadens the feature. (Bottom) Imaginary part of susceptibility vs the coupling laser detuning including the Doppler shifts for a distribution of atoms at room temperature. The EIT dip is broadened and weakened by the residual Doppler shift from Eq. 1.23. Both the amplitude and width increase as function of Ω_c.

In Fig. 1.10, the difference between the probe laser detuning (40MHz) and measured shift (≃64MHz) is due to the Doppler mismatch of the probe and coupling lasers[14]. The measured probe detuning in the spectrum is $\Delta_{pm} = D\Delta_p$, where Δ_{pm} is the measured shift and D is a parameter whose value depends on the wavelengths of the probe and coupling laser $D = \lambda_p/\lambda_c \simeq 1.6$.

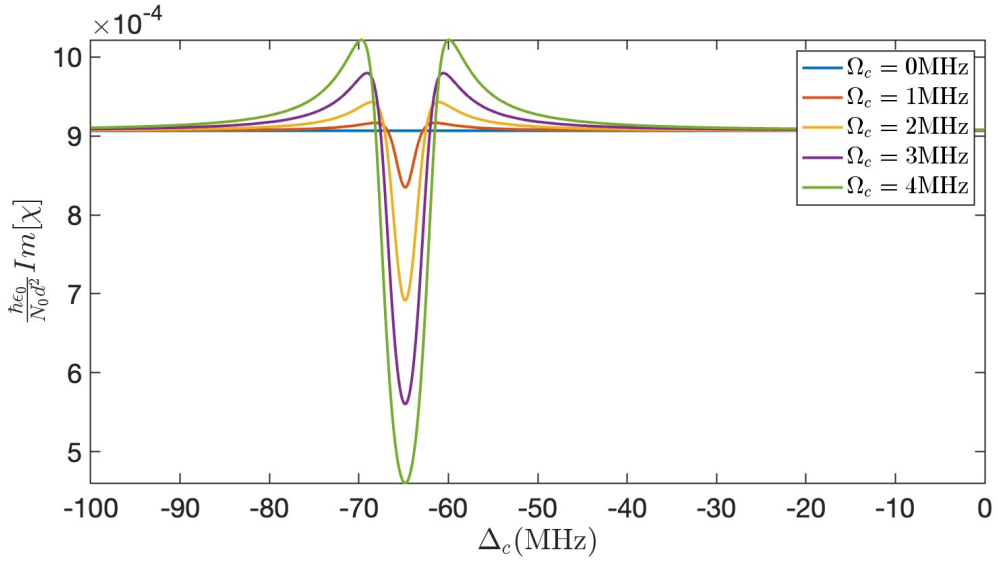

Figure 1.10: Imaginary part of the susceptibility vs coupling laser detuning for room temperature atoms and $\Delta_p = 40$MHz. The transparency dip position is shifted from 0MHz to -64MHz due to the uncompensated probe laser detuning. The difference between the shift in the position of the observed dip and the probe laser detuning is due to the Doppler mismatch between the probe and coupling lasers[14].

The transparency window width also increases with coupling laser power (P_c), as shown in Fig, 1.12. The measured widths are typically larger than predicted in Fig. 1.12 due to factors not included in the model, such as additional dephasing of the Rydberg state due to interactions between Rydberg atoms and/or ions in the sample, laser line widths[18] and frequency jitter, and transit-time broadening[19], [20].

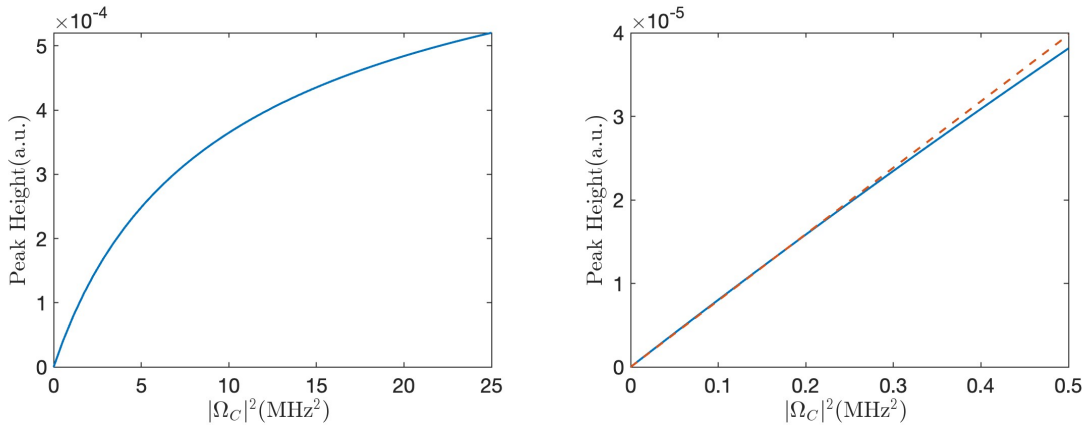

Figure 1.11: EIT dip magnitude vs the square of the coupling laser Rabi frequency, the latter proportional to the transition probability in lowest order perturbation theory. The dip magnitudes are derived from calculations similar to those shown in Fig. 1.10. The left figure shows a wide range of coupling laser Rabi frequencies, roughly corresponding to those relevant to the Rb $5p \rightarrow 32s$ transition at the range of laser powers explored in the experiment. The right figure shows a magnified view of the dip magnitude for low Rabi frequencies, illustrating its proportionality to the transition probability in this regime. The red dashed line is a linear reference.

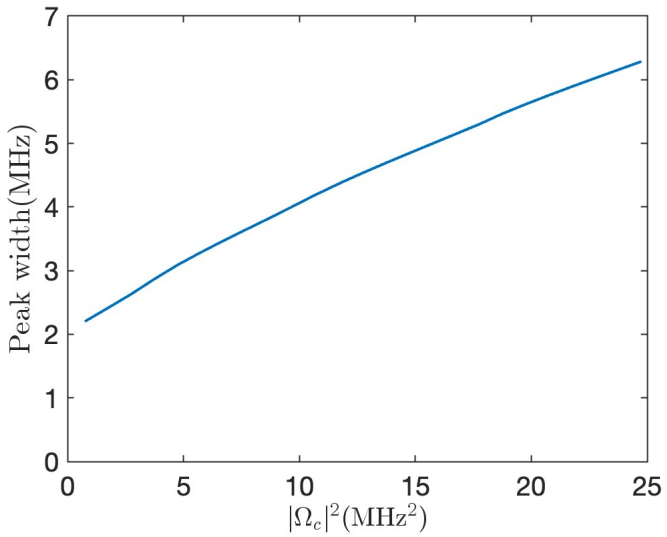

Figure 1.12: EIT peak width vs the coupling laser Rabi frequency squared. The peak width is derived from the calculated susceptibility including the Doppler effect. In general, the peak width increases non-linearly as a function of the squared interaction strength. However, for low interaction strengths, the width increases linearly with a substantial non-zero width near zero coupling.

1.5 Dissertation Structure

Chapter 2

The experimental apparatus necessary to perform the RF detection measurements is described in Chapter 2. Details are given on the design and use of the external cavity diode laser (ECDL), the intracavity second harmonic generation process, the electronics used to tune and/or frequency-lock the two laser systems, and the instruments used to produce various types of electric fields to benchmark the Rydberg electrometer.

Chapter 3

This chapter introduces the theory describing the effect of non-resonant low frequency fields on Rydberg atoms, providing the background for our self-calibrating broadband Rydberg electrometer design. We specifically explore the non-linear Rydberg response to combinations of fields with different frequencies which forms the basis for our approach to improve the sensitivity and frequency range of the electrometer, by combining the unknown signal field with a strong reference.

Chapter 4

Experimental results, benchmarking the operation of the Rydberg electrometer using a continuous coupling laser and strong DC reference, are presented and compared with the theory. These initial measurements revealed a non-linear response of the EIT signal at high coupling laser intensities that led to errors in the field measurement if not properly compensated. A second set of measurements, using a pulsed coupling laser, were then performed to identify appropriate regimes of coupling laser peak power and pulse duration for which accurate field measurements could be made. Additional measurements made using an RF antenna rather than a direct wired connection revealed the impact of an RF field-dependent coupling between the RF signal

source and the DC supply that altered the magnitude of both the RF and DC fields in the interaction region affecting the benchmark measurements for wired RF coupling. Further measurements showed that one could extract both the spectral amplitude of the RF signal and the magnitude of the DC field directly from the EIT spectra. Finally, the effectiveness of the electrometer was demonstrated using either low frequency AC (synchronous with modulation frequency of the coupling laser) or RF reference fields. The latter enables the extension of the electrometer into higher frequency regimes by enabling detection at the difference frequency between the signal and reference fields, reducing the required frequency scan range of the coupling laser. Comparisons of the performance of the electrometer for DC, low frequency AC, and RF reference fields are provided.

Chapter 5

The last chapter in this thesis gives a summary of which equations and approximations can/should be used for the RF field measurement for different amplitude range of RF field. In particular, plots showing limiting conditions for applying non-resonant Rydberg field-mixing EIT-based RF electrometry with different Rydberg states as a function of DC reference and RF signal fields are provided. Then the sensitivity of the current implementation of the RF electrometer is discussed, in terms of expressions involving the smallest detectable RF field. Assuming all parameters have been optimized, a smallest measurable field value is given for the current apparatus. Finally, a brief outlook exploring future improvements of our electrometer and how our approach can combine with others for RF measurement across a frequency range.

Chapter 2

Experimental apparatus

The experiments described in this dissertation involve ^{85}Rb atoms excited to Rydberg states in a vapor cell. This chapter describes the Vapor cells that hold the atoms, the lasers used for excitation, the electronics used to create DC/RF fields and manipulate/measure the lasers, and the software used for data detection and analysis.

The experiments were performed in Room 166/168 of the Physics Building at University of Virginia. The HVAC system is targeted to maintain lab temperature around $72°F$. In practice, the humidity of air blowing out of HVAC system is not controlled. Even though dehumidifiers in the lab can help control local humidity level, a change of humidity cannot be prevented when the weather is rapidly changing. Because the laser systems are affected by humidity changes, it is better to perform measurements on non-rainy days or days without large day and night temperature (and corresponding humidity) fluctuations. A Bluetooth temperature and humidity sensor (manufactured by Govee) is used to monitor the environmental condition near the optical setup.

2.1 Rubidium vapor cell

Two different vapor cells are used in our experiments. The first one is a clear right circular cylinder (7.5 cm long × 2.5 cm diameter) made of Pyrex without any metal plates or wires in the cell. This "locking" cell is used for frequency locking the probe laser via saturated absorption spectroscopy The second vapor cell is also a Pyrex cylinder (7.5cm long × 2.5cm diameter) but is fabricated to include two parallel metal plates (6cm long × 2cm width and 0.5cm separation) positioned along the axis of the cell. The metal plates each have two electric wire feedthroughs for connection to an external power supply. The EIT measurements are made in this "Rydberg" cell.

2.1.1 Vapor cell temperature control with feedback circuit

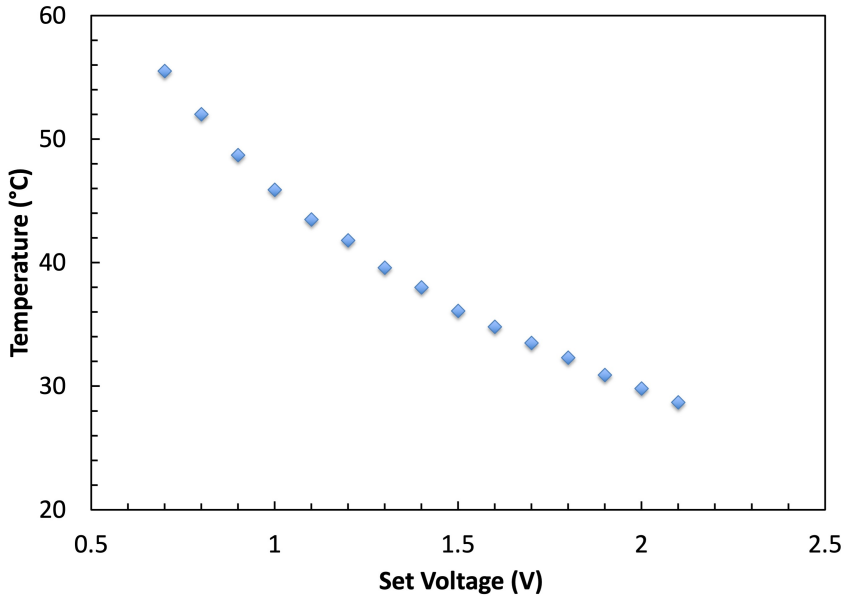

Figure 2.1: Cell temperature vs set voltage for the heating wire. Different temperatures can be selected for the Rubidium cell. Room temperature for the vapor cell corresponds to a set voltage of 3V. Typical temperature setting for experiments is $\sim 28°C$.

Our experiment does not require ultracold atoms, but a consistent temperature environment is preferred for the high precision EIT measurements since the atom density and residual Doppler shifts are temperature dependent. To achieve this goal, the Rydberg cell is wrapped with thin copper wires which serve as the heater, and a thermistor as a temperature sensor. The thin wires are folded at the start point so that adjacent wires carry current in opposite directions, minimizing the induced magnetic field.

Both the heating wires and the thermistor are connected to a proportional-integral-derivative (PID) feedback circuit (HTC-3000) [21] which compares the voltage across the thermistor to the setpoint voltage. The circuit board provides the appropriate current to the heating wires to maintain the cell temperature at the desired value.

2.2 Laser Systems

Laser-atom interactions are the basis for our RF electrometer. Two different tunable lasers are required for the measurements, utilizing the following components and modes of operation.

2.2.1 External Cavity diode laser

The EIT spectroscopy (see Section 2.2.5) is performed using a New FocusVortex 7000 Stable Wave tunable diode laser and a Toptica TA/DL-SHG laser system. The Vortex tunable laser and Toptica DL pro (the first stage of Toptica laser system) are external cavity diode lasers (ECDL). These lasers are widely used for laser-based atomic physics experiments due to their compact size, ease of use, and relatively good stability.

In an ECDL, a laser diode serves as the gain element, and is incorporated within a tunable resonant cavity to complete the external cavity diode laser. The wavelength selectivity is provided by angular dispersion selection from a diffraction grating[22]–[26]. As shown in Fig. 2.2, one side of the laser diode chip is covered with a high reflective (HR) coating while the other side has an anti-reflective (AR) coating to prevent the diode chip itself from acting as a cavity. The Laser light from the chip first passes through a collimating lens and is directed to the diffraction grating.

In the Littman-Metcalf design[25], [26] (used in the New focus laser), a rooftop prism reflects the first order diffraction from the grating back into diode as feedback. In the Littrow-Hansch design[22] (used in the Toptica laser), the diffraction grating sends the first order diffraction directly back into diode as feedback. The retro-reflecting

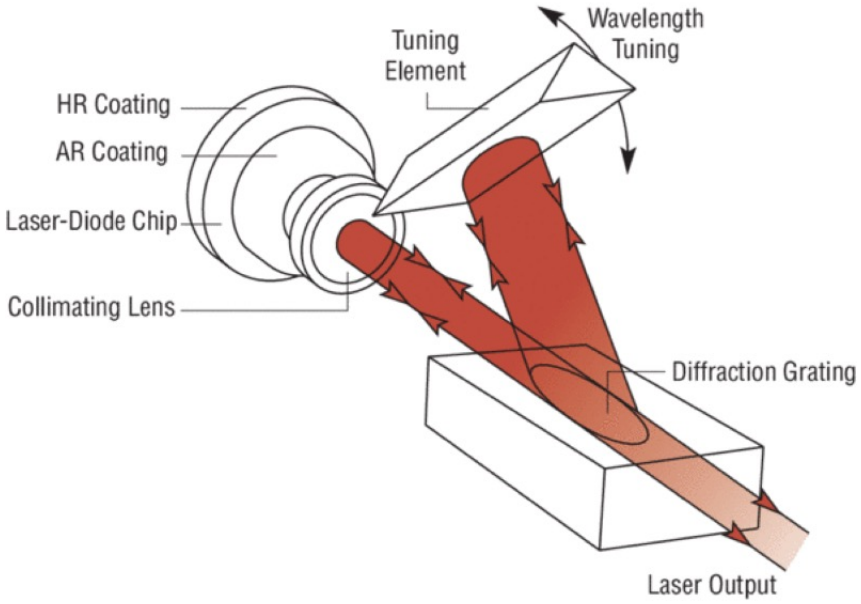

Figure 2.2: Principle of operation for the Littman-Metcalf ECDL[27].

element (prism or grating) and HR coating of the laser diode chip forms the external cavity and frequency tuning is achieved by adjusting the prism or grating angle to select which wavelength in the dispersed beam oscillates in the cavity. The tuning element (prism or grating) is mounted to a piezoelectric actuator to provide rapid frequency tuning and control. For any selected angle within the large first order dispersion angular range, only a narrow spectrum is retro-reflected and amplified. In the Littman-Metcalf design, the zero-order diffraction of the grating serves as the output beam of laser. In the Littrow-Hansch design, an output-coupler creates the optical cavity between the rear facet of the diode and the grating, and directs a portion of the oscillating laser light out of the cavity.

Mode-hop free tuning of the ECDL is achieved by simultaneously tuning two parameters, the prism-grating angle and the cavity length. The cavity length needs to be

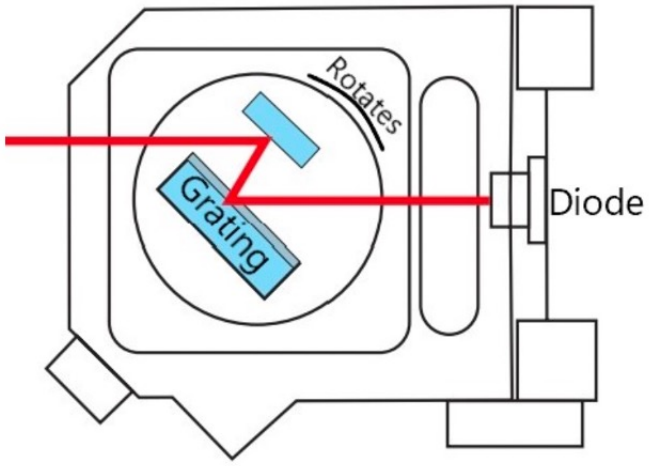

Figure 2.3: Principle of operation for the Littrow-Hansch ECDL[28].

related to the feedback angle of diffracted beam as

$$L(\theta_d) = N\lambda(\theta_d)/2 = N\Lambda(sin\theta_i + sin\theta_d)/2 \tag{2.1}$$

Where L is the cavity length, $\lambda(\theta_d)$ is the discrete set of possible modes that can lase, N defines the cavity mode which remains the same in a mode-hop free laser, Λ is the groove spacing of the diffraction grating, and θ_i and θ_d are the angles of incidence and diffraction, respectively.

In the Littman-Metcalf design, by appropriately setting the pivot point of the prism, these two parameters can be synchronized to allow for continuous tuning of the frequency of the diode laser free of any mode-hops, i.e. no change in N[25], [26]. In the Littrow-Hansch design, as the length of the piezoelectric that controls the external resonator length and grating angle is changed, the photodiode current is adjusted leading to a change in the internal resonator length, so that mode-hop free tuning is achieved[22].

For the measurements, the New Focus laser is tuned near 780nm. It serves as the probe laser and drives the ^{85}Rb $5S_{1/2}$ to $5P_{3/2}$ transition. The typical operating current is ∼90mA, and the standard power output is ∼ 30mW. The voltage on the piezoelectric actuator that controls the laser frequency is described in the Section 2.2.5. Daily Operating Details are provided in Appendix A.1.

The ECDL lasers are exceptionally sensitive to unwanted optical feedback, so optical isolators are used to block stray reflections that are directed back into the Diode lasers. The isolator used with the New Focus laser is an IO-D-780-VLP from Thorlabs. This allows linearly polarized light to pass through in one direction but extinguishes light in other direction irrespective of its polarization.

The Toptica DL pro laser, which is the first stage of TA/DL-SHG pro laser system, is tuned to ∼ 964nm. The ∼ 40mW beam is sent though a tapered amplifier (TA). Within the TA, the size of the beam is gradually increased to interact with a larger gain region as the power of the beam propagates through the fiber. The power after the TA is ∼ 600mW. To obtain the ∼ 482 nm light required to drive the $5p \rightarrow ns$ Rb Rydberg transition, the 964 nm beam from the TA is then sent to frequency doubling cavity. The TA/DL-SHG system is shown schematically in Fig. 2.4.

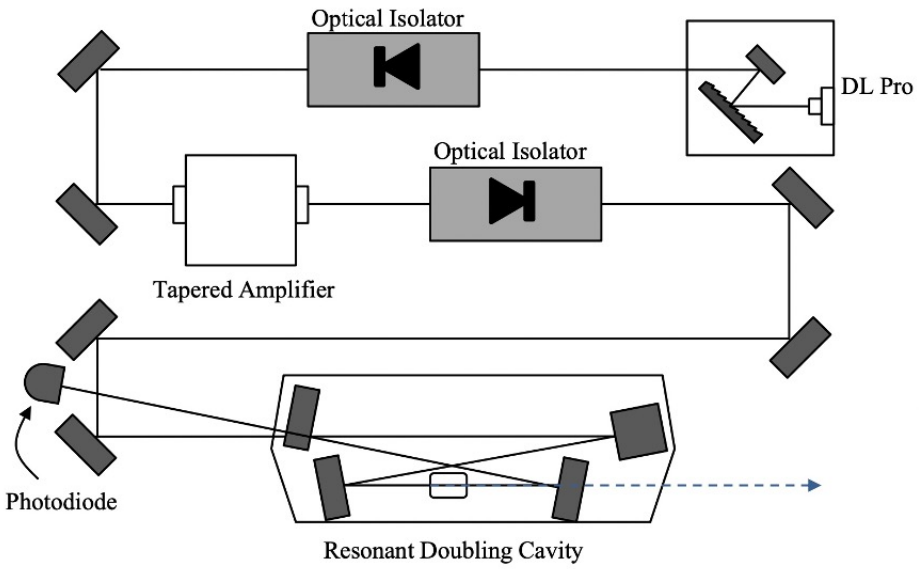

Figure 2.4: Principle of operation of the TA-SHG pro laser system[28].

2.2.2 Second harmonic generation

Non-linear frequency-mixing is commonly used to convert the coherent infrared/near infrared radiation produced by diode lasers to desired frequencies in the visible or ultraviolet[29], [30]. In our TA/DL-SHG pro laser system, a bow-tie-ring second harmonic generation (SHG) cavity surrounds a non-linear crystal that doubles the frequency of the circulating 964nm light, as shown in Fig. 2.5. The SHG cavity length is stabilized using the Pound-Drever-Hall technique[31], [32]. The ECDL diode current in the DL-pro (Fig. 2.4) is modulated at 5MHz , creating frequency sidebands spaced by symmetrically centered around the circulating 964nm light. Some portion of the 964nm laser passes through the high reflective mirror and into a fast photodiode, where the relative intensity of the two sidebands is compared. The two sidebands will have equal intensity when the cavity length provides minimum loss at the central fundamental frequency. The error signal is sent to a PID feedback controller which

appropriately adjusts the the piezoelectric actuator to stabilize the cavity for optimum circulating power and SHG efficiency.

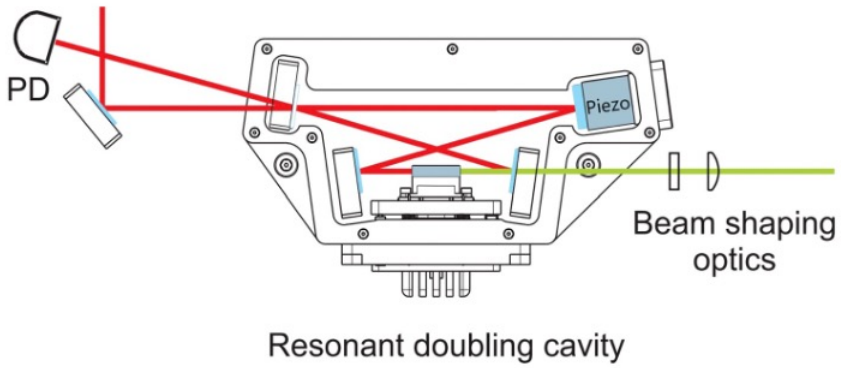

Figure 2.5: Principle of operation for second harmonic generation[28].

Normally, the Toptica TA/DL-SHG can provide $\sim$ 120mW of laser light at 482nm. The power is easily affected by the position of the cavity mirrors, the beam alignment and changes with output frequency. In this dissertation, the TA/DL-SHG laser is referred as the "blue laser" or "coupling laser."

2.2.3 Acousto-Optic Modulator

Before the blue laser is sent to the Rubidium vapor cell, it passes through an acousto-optic modulator (AOM), IntraAction Corp Model AOM-802A1. As shown in Fig. 2.6, the active element in the AOM is a piezoelectric transducer attached to a quartz crystal block. An oscillating voltage drives the piezo and creating an acoustic standing wave in the quartz. The standing wave produces a periodic variation in the refractive index of the quartz, so that it behaves like a diffraction grating.

Laser light entering the AOM at the Bragg angle $\theta_B = \frac{\lambda F}{2V}$, where λ is the laser wavelength, F is the acoustic frequency, and V is the acoustic velocity of the quartz

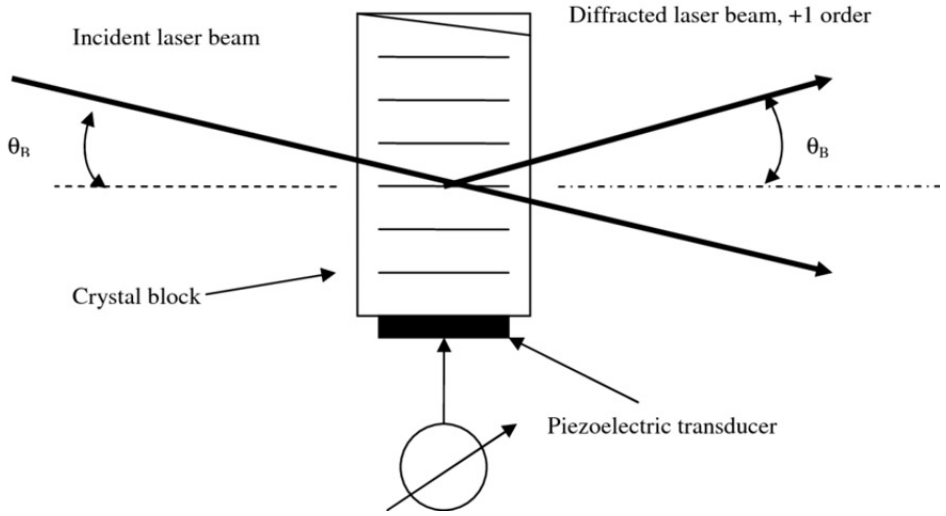

Figure 2.6: Principle of operation for Acousto-Optic Modulator[33].

crystal, is diffracted by an angle $\theta_R = 2\theta_B$. The diffracted beam can be switched on and off by pulsing the oscillating voltage applied to the piezoelectric transducer.

We use the single-pass first-order diffraction from the AOM to chop the light from the Toptica laser into pulses with desired duration and repetition frequency. The diffraction efficiency is $\sim 60\%$ to 70% depending on the transverse profile of the laser beam. The pulsed AOM has negligible leakage into the first order beam when the gate pulse is off to prevent any Rydberg excitation when the coupling laser is intended to be off.

2.2.4 Saturated Absorption Spectroscopy

Before the 780nm probe laser beam enters the Rubidium vapor cell, it's frequency is locked to the side of a Rb resonance using the saturated absorption spectroscopy and a proportional-integral-derivative (PID) feedback circuit. The saturated absorption is obtained using a pump-probe measurement in the room temperature "locking" Rb

vapor cell.

A beam splitter directs a small fraction (5%) of the 10mW 780nm laser beam into the cell, serving as the pump laser for the saturated absorption. The pump laser has enough power to saturate the $5s \rightarrow 5p$ transition of interest. After passing through the cell, roughly 5% of this pump beam is retro reflected through the Rb cell, serving as the probe laser, and is detected by a balanced photo-diode pair.

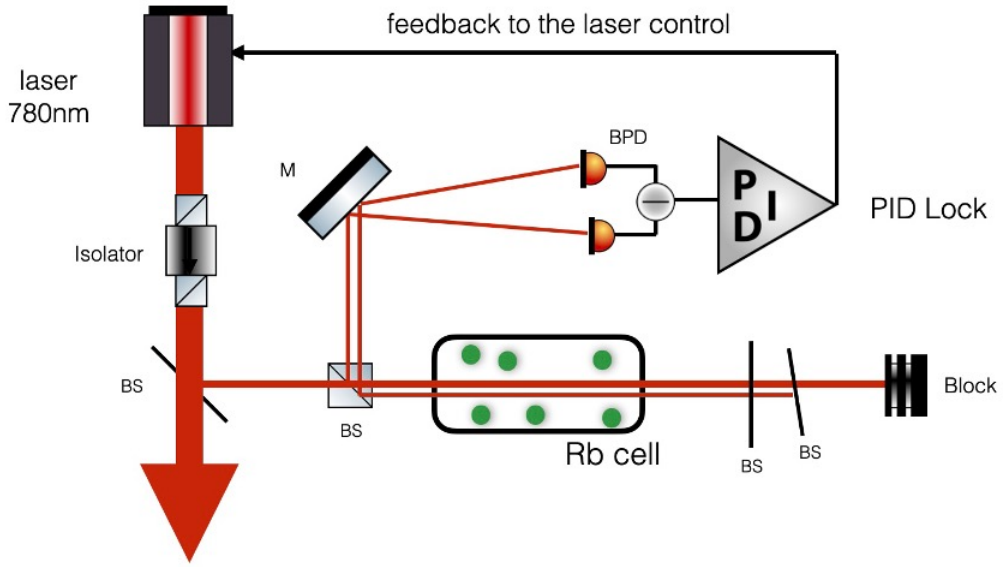

Figure 2.7: Detailed setup for saturated absorption spectroscopy including the laser source, Rubidium cell, and balanced photo-diode detector for the PID locking circuit.

When the strong pump beam, transits the cell with the same frequency as the counterpropagating probe, the two beams are most strongly absorbed by atoms in two different velocity groups. For example, for a laser frequency f_A that is below the resonance frequency f_0, probe and pump photons are most strongly absorbed by atoms moving in opposite directions, directly towards each beam. Therefore, the probe absorption is unaffected by the presence of the probe.

However, when the laser frequency is tuned to resonance at f_0, atoms that have zero

velocity or are moving perpendicular to the beams will be strongly absorbing. In this case, atoms that have been excited by the pump are not available to absorb light from the probe beam. Accordingly, as the laser frequency is scanned over the resonance, a narrow "Lamb dip"[34] is observed in the absorption of the probe at f_0 (i.e. a peak is observed in transmission spectrum). The width of the Lamb dip is determined by the natural linewidth of the excited state, rather than the temperature of atoms in the cell allowing for a much tighter frequency lock.

The ^{85}Rb $5s$ to $5p$ transition includes several non-degenerate resonances, due to the hyper-fine structure associated with the nuclear spin. The saturated absorption spectrum exhibits dips at each of the hyperfine transitions. There are additional spikes in the transmission spectrum known as crossover peaks which appear at frequencies $f_{1,2} = \frac{1}{2}(f_1 + f_2)$ exactly halfway between each pair of atomic resonances, at f_1 and at f_2. At $f_{1,2}$, atoms moving with the proper velocity will absorb downward Doppler shifted probe beam photons at f_1 and upward shifted pump beam photons at f_2 (or vice versa). Thus, at this crossover frequency $f_{1,2}$, the number of atoms available for absorbing probe beam photons is reduced, similar to the case at the resonance frequencies f_0 leading to cross-over peaks in the probe transmission spectrum.

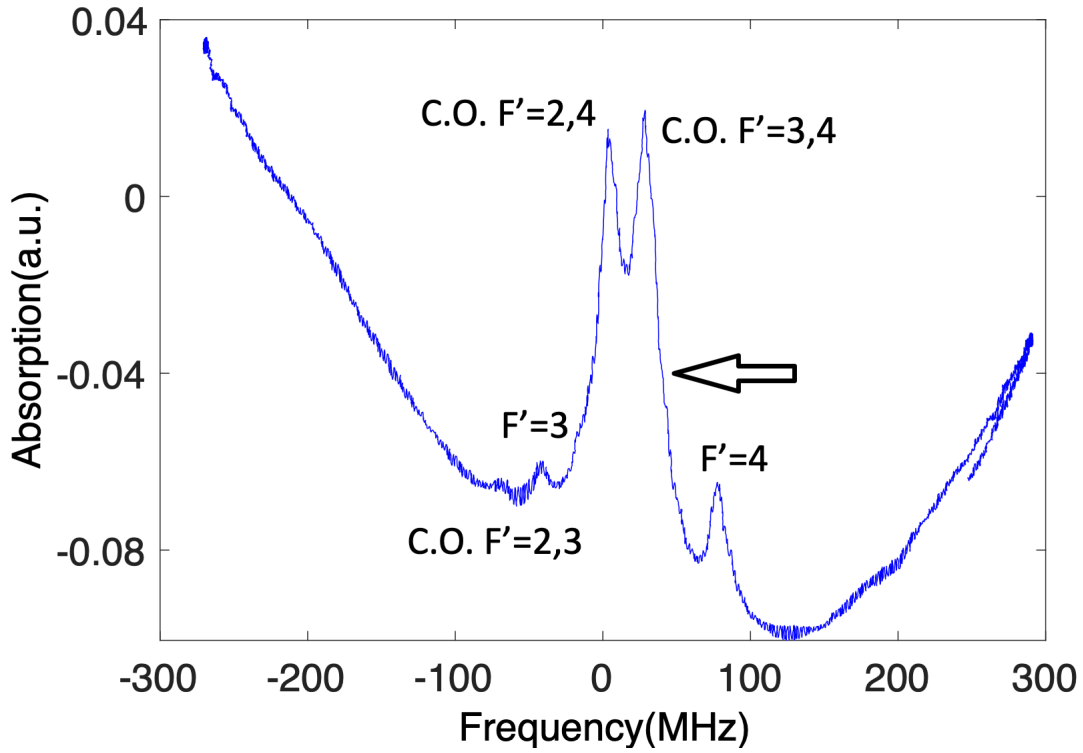

Figure 2.8: Experimental saturated absorption frequency scan collected from oscilloscope. The largest two transmission spikes are the crossover peaks corresponding to the $5S_{1/2}\ F = 3 \rightarrow 5P_{3/2}\ F' = 4$, and $5S_{1/2}\ F = 3 \rightarrow 5P_{3/2}\ F' = 2$ hyperfine transitions The arrow indicates the typical lock point. Further explanation of this spectrum is presented in reference[35].

As shown in the saturated absorption spectrum in Fig. 2.8, the locking point for the EIT probe beam is positioned on the downward (positively detuned) slope of the $5S_{1/2}\ F = 3 \rightarrow 5P_{3/2}\ F' = 3, 4$ cross-over peak. The voltage from the balanced photodiode is compared to the setpoint on the PID controller and the error signal is fed back to the piezo tuning element in the New Focus ECDL. By adjusting the setpoint voltage offset, the frequency lock point can be fine tuned over a small range.

2.3 Electronics Systems

The laser systems described in the previous section are controlled by various electronic circuits that provide frequency stabilization and amplitude modulation. In addition, the energies of Rydberg atoms are modified by externally applied electric fields, due to Stark effect. Several of the key circuits and instruments used in the measurements are described below.

2.3.1 Balanced photodiode detector

In balanced detection, the intensities of two optical beams are compared using two identical photodiodes. The resulting photocurrents are amplified deferentially in order to produce electrical signal proportional to their difference. The differential detection amplifies the difference between the two optical intensities while eliminating noise that is common to both beams. This approach is widely used for converting the optical response from light matter interactions to an electronic signal[36].

Two 9V batteries are used to provide the +9V and -9V bias voltages. Batteries are the preferred power source as they do not suffer from voltage ripple or other electronic noise in the output of an AC powered DC source. A narrow red optical bandpass filter is typically placed in front of the photodiodes to reject ambient light. If desired, additional biasing resistors can be added in series with the two photodiodes to reduce the differential gain.

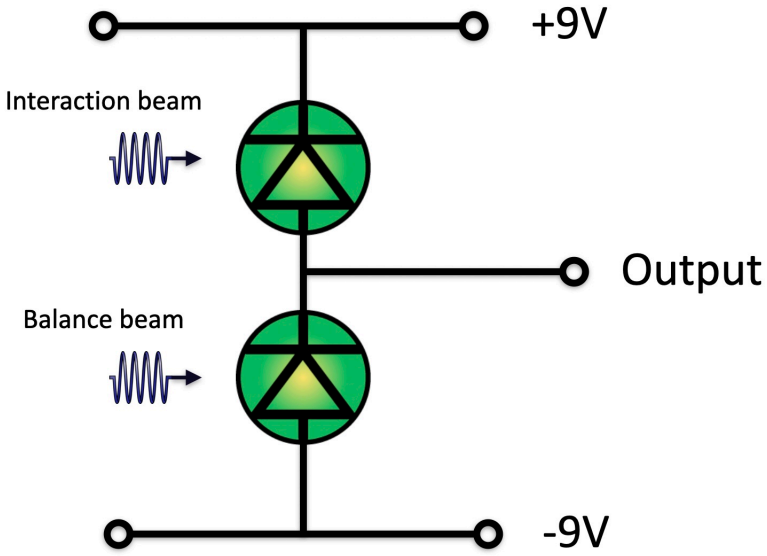

Figure 2.9: Balanced photodiode circuit used for laser spectroscopy. The interaction beam refers to the one overlapped with the strong coupling (for the EIT measurements) or pump (for saturated absorption locking) laser. The balanced beam refers to the one passing the same region of the cell but not overlapping with other laser. Two photodiodes separately receive the interaction and balanced beams.

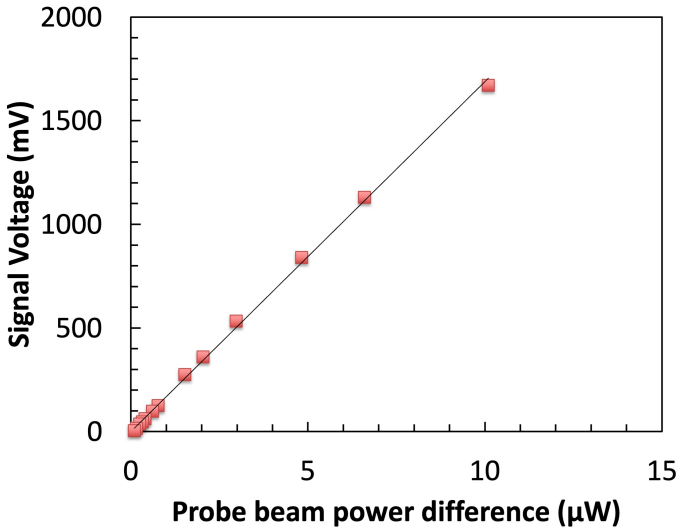

Figure 2.10: Balanced photodiode signal vs beam power difference. The power of the interaction beam is changed while keeping the balanced beam at zero. The output voltage is linearly proportional to the power difference for the range of interaction beam powers used in the experiments.

2.3.2 Frequency Locking with PID circuit

We use the saturated absorption spectroscopy (described in section 2.2.4) to implement a side-of-resonance lock using a proportional-integral-derivative (PID) feedback system. To achieve the locking, the feedback circuit compares the photodiode signal with a desired value (setpoint voltage), via a differential amplifier. Any difference in the amplitude of the signal relative to the set voltage is amplified and fed back to the control unit of the ECDL. The voltage of piezo is then changed to maintain the laser at the desired frequency. The time integral, and derivative of the difference signal can be combined with the proportional amplified for better and longer frequency locking.

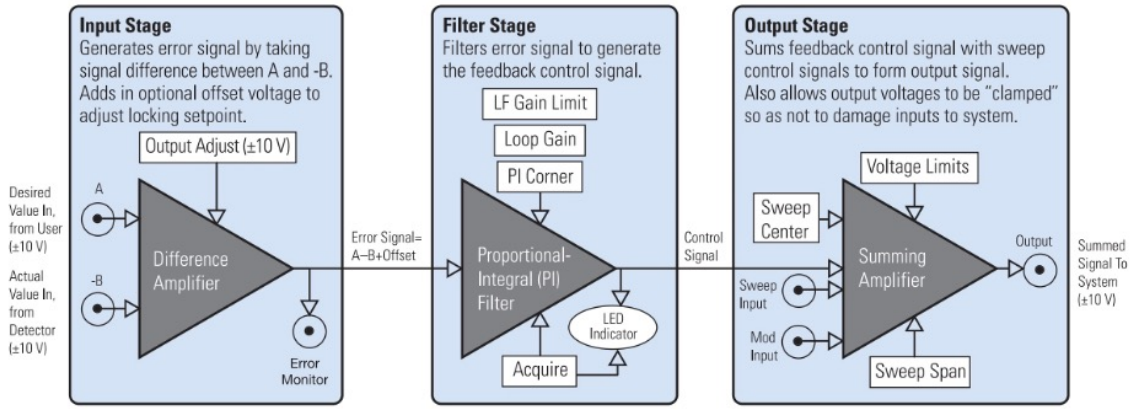

Figure 2.11: New Focus LB1005 high-Speed Servo Controller architecture[37].

The 780nm probe laser frequency is locked to the falling edge of the ^{85}Rb $5S_{1/2}$ $F = 3 \rightarrow 5P_{3/2}$ $F' = 3, 4$ crossover peak as described in section 2.2.4. The 482nm coupling laser can be frequency locked by directing a small portion of the 964nm seed laser into a Fabry-Perot Interferometer (Model: Thorlabs SA 200-3B). The interferometer (FPI) is housed in sealed, temperature controlled cell to reduce drifts associated with changes in room temperature and pressure.

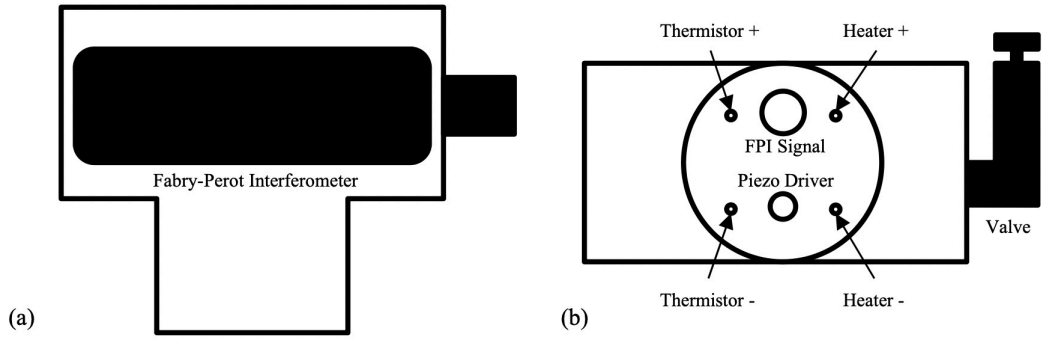

Figure 2.12: A schematic drawing of the "T" used for controlling the pressure of the Fabry-Pérot Interferomter.(a) The top view shows the "T" shape with the FPI resting inside the main part of the "T". (b) the side view shows the electrical feedthroughs that are used for the temperature control and the valve that is used for pressure tuning of the FPI frequency[6].

The FPI contains a back reflector attached to a piezoelectric transducer that allows for control of the cavity length. The piezoelectric is connected to the Thorlabs SA201 spectrum analyzer controller or a Thorlabs TPZ001 piezo driver. The SA201 driver provides a triangle or sawtooth voltage to the FPI piezo to measure the spectrum of the laser by scanning the cavity length. For frequency locking, the controller is replaced by the piezo driver that can apply a static (or slowly varying) voltage from 0V to 150V. To lock the 482nm laser, the DL laser (in the Toptica TA/DL-SHG pro laser system) is frequency tuned to an EIT resonance.The TPZ001 FPI piezo driver voltage is then adjusted so that the 964nm FPI transmission signal is positioned approximately half-way up the the rising edge of a transmission peak. The FPI signal is amplified (by the amplifying circuit in the SA201 controller) and sent to the Toptica PID 110 control circuit which provides the error signal to lock the DL laser frequency.

As an alternative to tuning the FPI cavity length with the piezo, the location of the transmission maxima can be tuned by changing the pressure in the sealed chamber

enclosing the FPI. Fine pressure tuning is accomplished using the plunger of a vacuum valve to change the volume of the gas in the enclosure.

2.3.3 Frequency scanning

EIT spectroscopy involves a frequency scan of either the probe or the coupling laser. The frequency of the probe laser can be controlled using the Vortex 6000 Controller by varying either the diode current or piezoelectric voltage.

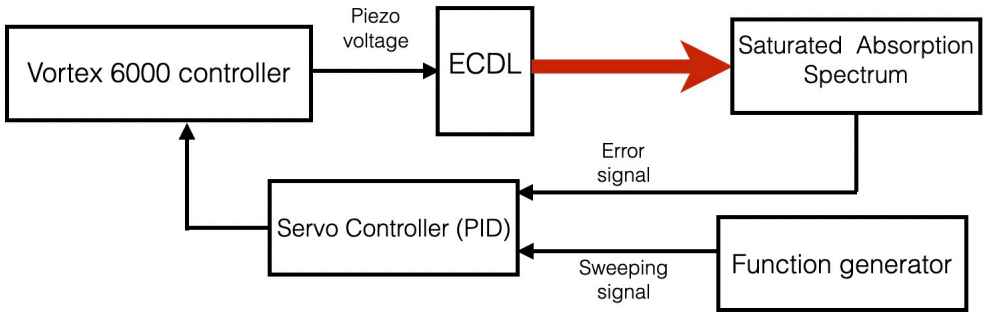

Figure 2.13: A schematic of the frequency control system for the New Focus laser. The red line is the 780nm light from the diode laser to the Rubidium cell for saturated absorption spectrum measurement. The signal from the absorption spectrum goes to the servo controller. A function generator sends a periodic voltage ramp (at approximately 1 Hz) to the servo controller which is passed to the ECDL piezo driver in the Vortex 6000 ECDL controller. The ramped piezo voltage sweeps the ECDL frequency. Once the setpoint voltage has been adjusted to the desired level on the side of the cross-over resonance in the saturated absorption spectrum, the locking circuit is engaged. This halts the voltage sweep and directs the error signal to the Vortex 6000 to hold the laser frequency on the side of the resonance.

As described previously, the frequency of the coupling laser can be locked using the PID 110 module in the TA/DL SHG-pro system. The SC 110 frequency scan module in the TA/DL SHG system can be used to scan the frequency of the fundamental ECDL and the frequency doubled output. An alternative method for scanning the

coupling laser involves first locking the ECDL to the FPI (in Fig. 2.12), and applying a periodic voltage ramp to FPI piezo to vary the FPI cavity length. Compared to the internal scan module, this method can minimize the laser drift between successive scans, but the modulation of frequency is limited to low frequency (several Hz) and smaller range (up to 100MHz) compared to the frequency scanning of ECDL.

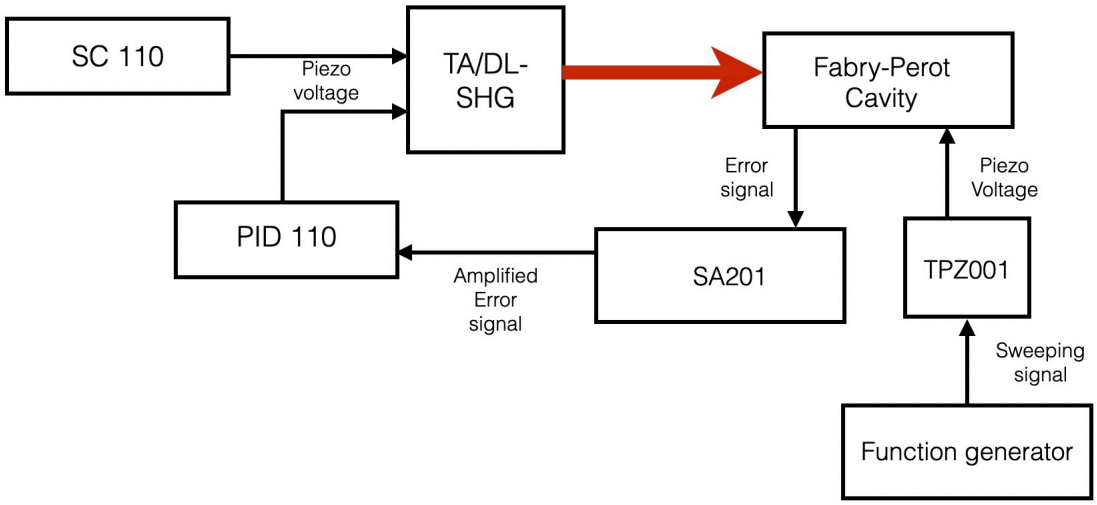

Figure 2.14: A schematic of the frequency control system for the Toptica TA/DL-SHG Pro. The red line represents the 964nm laser beam from the ECDL to the Fabry-Perot Interferometer (SA200-3B). The FPI cavity length is controlled by the piezo. For frequency locking, a voltage that is proportional to the optical transmission through the FPI is fed to the amplifier (SA201) and from there to the feedback controller (PID 110). For frequency scanning, a ramped voltage from the SC 110 is fed into the PID 110 and then to the piezo in the ECDL in the TA/DL-SHG pro.

Considering that the probe laser can be tightly locked to the atomic absorption and the coupling laser can only be locked to an optical cavity that is subject to thermal drifts (∼50MHz over an hour) and instabilities caused by table vibrations and acoustic noise, for the EIT measurements, we typically lock the probe laser and scan the coupling laser using the internal scan module.

2.3.4 DC field generation

DC voltages applied to the field plates within the Rydberg cell provide the static reference fields for the electrometer. The DC voltage source is an HP6286A 20V/10A DC power supply. The supply is connected to the metal plates through the wire feedthroughs of the Rubidium cell as shown schematically in Fig. 2.15.

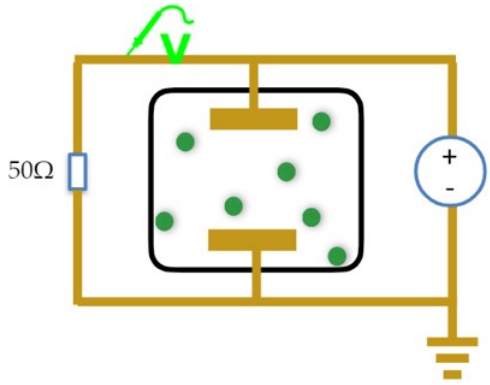

Figure 2.15: Schematic of the DC voltage supply connected to the internal plates of the Rubidium cell. A 50Ω resistor is connected with wire feedthroughs.

2.3.5 RF field generation

Three different RF power supplies with different output power and frequency ranges (IntraAction Model VFE frequency synthesizer, Wavetek Mode 2500C signal generator, and Agilent 83620B Synthesized Swept-Signal generator[38], [39]) provide the RF fields for the electrometer measurements. The RF voltages from the units can be applied directly to the field plates using the wire feedthroughs, or can be indirectly coupled to the plates using a simple antenna. In both cases, one end of a coaxial BNC cable is attached to the coaxial output connector of the signal generator. The other end of the BNC cable is terminated with alligator clips which can be directly connected to the wire feedthroughs or serve as the antenna for indirect coupling.

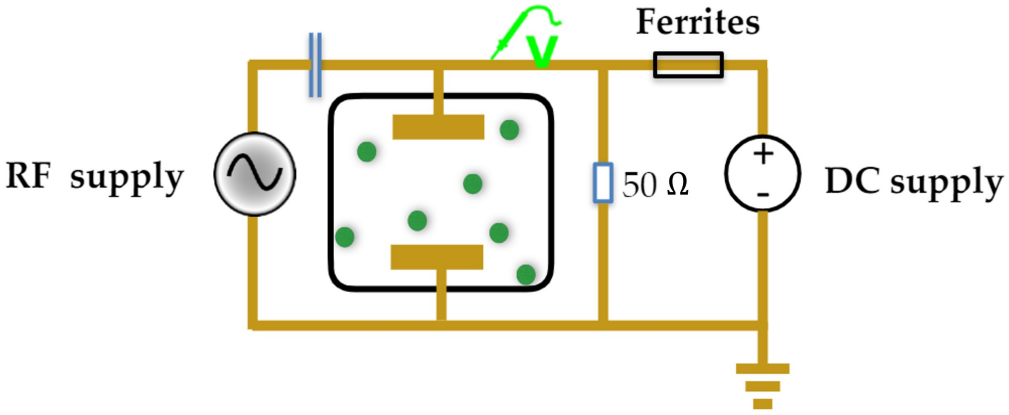

Figure 2.16: The schematic of the DC voltage supply and RF field supply connected to the internal plates of the Rubidium cell. A 50 Ω resistor and a 4.7 μF aluminum capacitor are connected with wire feedthroughs.

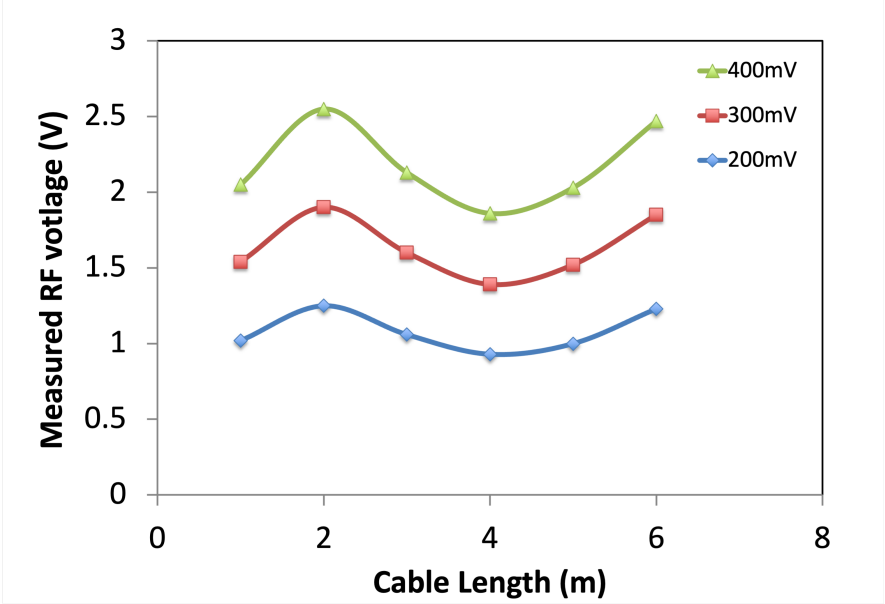

Figure 2.17: Peak to peak 60MHz RF voltage measured on the metal plate vs the BNC cable length. The metal plate is connected to the RF power supply through different length BNC cables. The peak to peak RF voltage on the plates is measured by the high-impedance voltage probe P6139A [1]. The output voltage reading on the Wavetek RF supply is set to three different levels shown in the legend.

A variety of factors affect the coupling of the RF voltage from the signal generators

to the metal plates inside/outside of the Rubidium cell. One important factor is the BNC cable length between the RF generator and the metal plates. Fig. 2.17 shows an example of the cable length dependence of the voltage across the field plates for a fixed RF amplitude from the signal generator. So a fixed strength BNC cable is used to connect the metal plate to the RF supplies.

Meanwhile, despite the addition of capacitors and inductive damping ferrite rings placed between them, the RF power supply influences the output of the DC supply when both supplies are directly connected to the metal plate. The coupling between the two supplies increases non-linearly with the RF voltage. This is discussed in more detail along with the experimental results in the RF wire and antenna setup section 4.2.

2.3.6 MW field generation

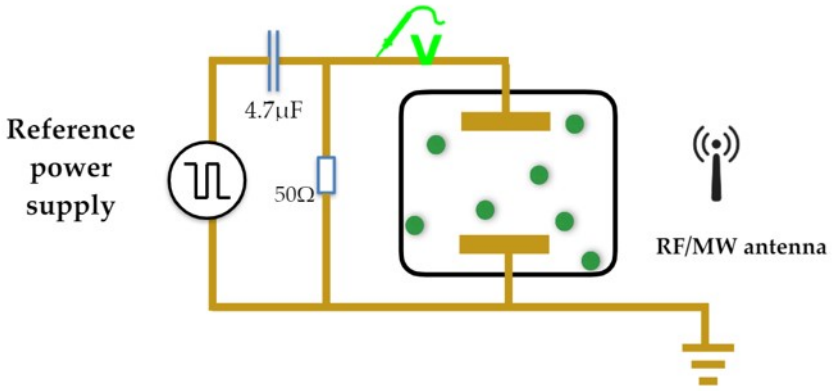

Figure 2.18: Schematic of the experimental configuration using a DC or low-frequency AC reference and indirect RF signal field coupling. The DC/AC voltage supply is directly connected to the internal plates of the Rubidium cell. The RF antenna wirelessly directs an RF field into the cell. A 50 Ω resistor is connected in parallel with the field plates inside the cell using the wire feedthroughs.

Low frequency microwave fields are generated with the IntraAction Model VFE frequency synthesizer, and introduced into the cell using the indirect antenna configuration. High frequency microwave fields are generated with an Agilent 83620B Synthesized Swept-Signal generator and introduced into the Rydberg cell using waveguide and a microwave horn, designed for the frequency range of interest, placed near the Rubidium cell.

2.3.7 Delay generator

The coupling laser pulse duration, synchronization of those laser pulses with the low-frequency AC reference, and referencing the pulse repetition frequency to the lock-in amplifier, are controlled by digital delay generators. The Stanford Research System DG 535 provides 4 independent outputs with a resolution of 5ps[40]. For the experiments using lock-in detection, the reference signal is a square wave of 40KHz frequency.

As mentioned in section 2.2.3, the first order AOM diffraction chops the 482nm beam from the Toptica laser to pulse the coupling laser. The AOM driver, which is an RF field generator, is gated by a pulse from the delay generator. The length of the coupling laser pulses, and their repetition frequency, are determined by the duration and repetition frequency of the gate pulses from the delay generator. If desired, the reference electric field can also be produced by the delay generator, providing a reference voltage (up to 5V) across the field plates synchronized with the coupling laser pulses.

2.3.8 Lock-In Amplifier

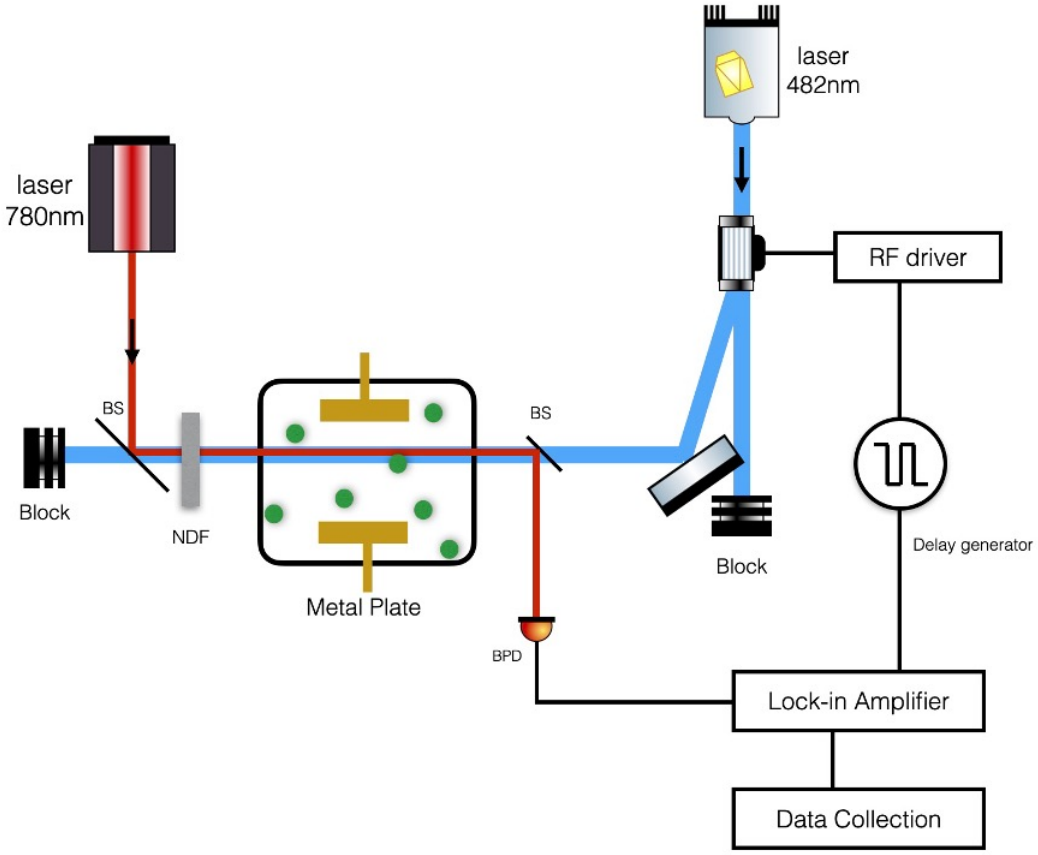

Figure 2.19: A schematic of the lock-In amplifier in the experimental setup. One channel of the delay generator modulates the amplitude of the RF field sent into the AOM driver. Another delay generator channel provides a square wave at the save frequency which serves as the frequency reference for the lock-in amplifier. Due to the pulsing of the coupling laser, the EIT signal received by photodiode is modulated at the reference frequency.

The lock-in technique is used to detect and measure very small AC signals. A lock-in amplifier can make high precision measurements of small signals even when the signals are obscured by noise that is a hundred (even a thousand) times larger. Essentially, the lock-in filters the input, passing only the portion within a narrow frequency window to a high-gain amplifier. The central frequency and bandwidth of the filter

can be tuned by the user to match that of the signal of interest.

The technique requires that the experimental signal is generated at a well-defined frequency, and works best if that repetition frequency is located within a relatively quiet part of the ambient noise spectrum.

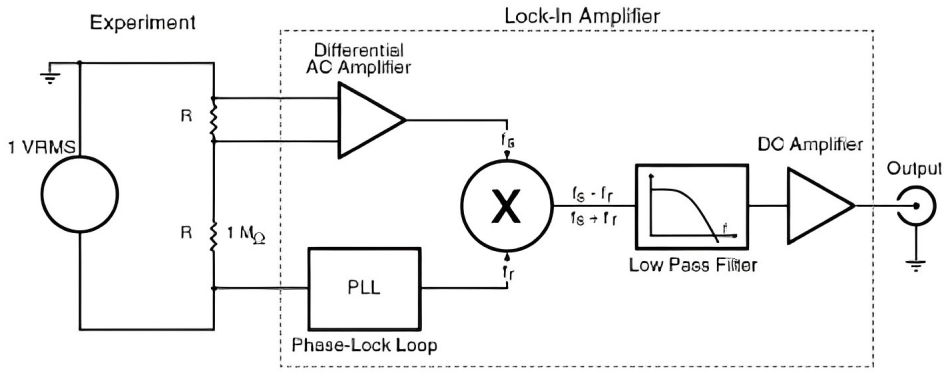

Figure 2.20: Schematic block diagram of the lock-in amplifier[41].

In the experiment, the AOM driver is gated by the delay generator at a 40kHz repetition frequency, as described in the previous section. With the pulsed coupling laser, the EIT signal from the balanced photodiodes is also modulated at 40kHz. The lock-in amplifier receives the modulated EIT signal from the photodiodes along with the reference signal from the delay generator. The two electric signals are mixed with the correct phase, through a low pass filter, and finally amplified with a high gain. Only those difference frequency components within the low pass filter's narrow 1kHz bandwidth will pass through to the DC amplifier.

The lock-in phase is chosen to maximize the amplified signal. The best approach is to first adjust the phase to null the signal, and then to shift the phase by 90° for the measurements. The gain is chosen according to the input voltage amplitude.

2.4 Data collection and Analysis

Data collection is based on a Tektronix DPO3032 digital phosphor oscilloscope . The oscilloscope records the time dependent voltage from the lock-in amplifier, which is linearly proportional to the time-dependent variation in the probe laser intensity as the coupling laser frequency is scanned. The time axis can be converted to coupling laser frequency using the frequency scan range and sweep time. The scan range is determined by observing the variations in the FPI transmission and the frequency calibration is confirmed using the location of the sidebands in the EIT spectrum for a known RF signal frequency.

All of the data acquired in the experiments presented in this dissertation were analyzed using EXCEL, Matlab, and codes written in Python or R programming language. Excel and Matlab are used for plotting the data and comparison with calculations.

Chapter 3

Theoretical background

In this chapter, we describe the theory underlying our scheme for RF detection in the presence of a DC, AC, or RF reference field. Because our principal interest is an RF detection scheme with broadband sensitivity, we focus on non-resonant interactions for which the atomic response to the RF signal field has only a weak frequency dependence. In this non-resonant regime, and for sufficiently weak fields in which the DC Stark shift is well described by a field-independent polarizability, the adiabatic approximation provides a highly accurate description of the atomic response. By selecting appropriate Rydberg states for detection, one can always work in a regime were this condition holds.

Consider a Hamiltonian $\hat{H}$ describing the evolution of a system initially in state ψ_0. Provided the initial state remains an eigenstate of the system and the time evolution of the Hamiltonian induces no transitions, then at any instant, $\psi(t)$ is the solution to Schrodinger equation $\hat{H}\psi(t) = E(t)\psi(t)$ with:

$$\psi(t) = e^{i\theta(t)}\psi_0 \tag{3.1}$$

where adiabatic phase is

$$\theta(t) = -\int_0^t E(t')dt' \tag{3.2}$$

In weak static electric fields, a low angular momentum Rydberg state nL undergoes a quadratic Stark shift, $\Delta E = \frac{1}{2}\alpha F^2$ where α is the state-dependent polarizability, and F is the static field. This remains an excellent approximation as long as the Stark shifted level is energetically well-separated from neighboring Stark states. We focus on ns states throughout this dissertation due to the limited state multiplicity (m_j=1/2 only) and correspondingly reduced complexity of the EIT spectra.

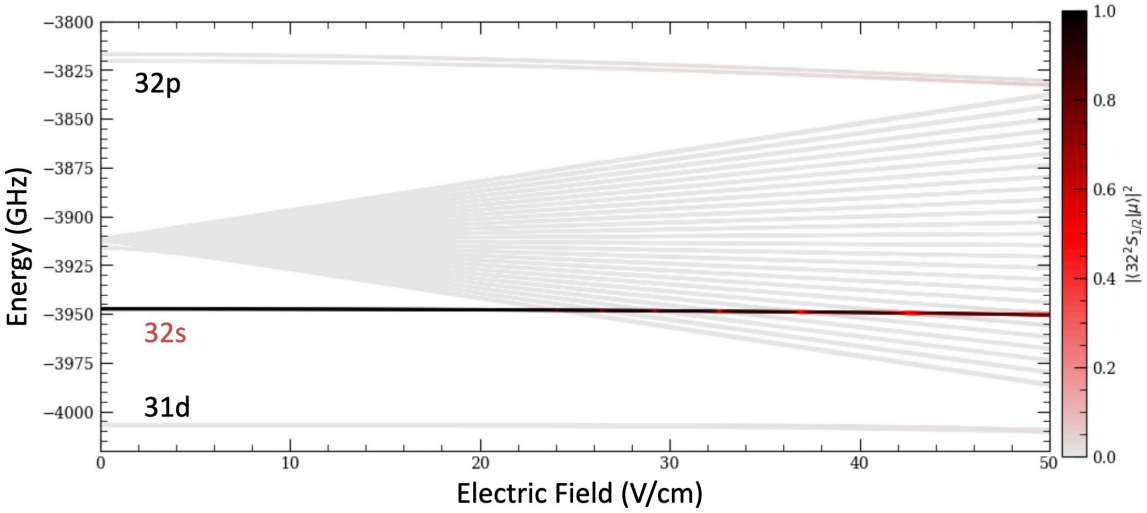

Figure 3.1: Map of the ^{85}Rb n=29 Stark manifold with electric field ranging from 0 to 50V/cm, calculated by python notebooks from ARC[7].The color indicates the percentage of the original 32s state in each Stark eigenstate. The 32s state has a quantum defect of 3.131 and starts to merge with the manifold around 24V/cm.

As illustrated in Fig. 3.1, the ns states in Rb become strongly coupled to other Rydberg states in a field of $F_c \sim 2 \times 10^9\ n^{-5.24}$ V/cm (as determined from a fit of F_c for different n in the Rb Stark map). For $F < F_c$ small deviations from a purely quadratic Stark shift can be accounted for by assuming the polarizability has a weak field dependence. Fig. 3.2 shows the field dependent polarizability for the 32s state,

for $F < F_c$, from the derivative of the stark shift

$$\begin{aligned} \Delta(F) &= \frac{1}{2}\alpha F^2 \\ \alpha(F) &= \frac{d}{FdF}\Delta(F) \end{aligned} \tag{3.3}$$

In our basic electrometer implementation, the atoms are exposed to a strong, known static reference to assist in the detection of a weak unknown RF field. In this case, the polarizability value corresponding to the applied static field gives the most accurate RF field determination.

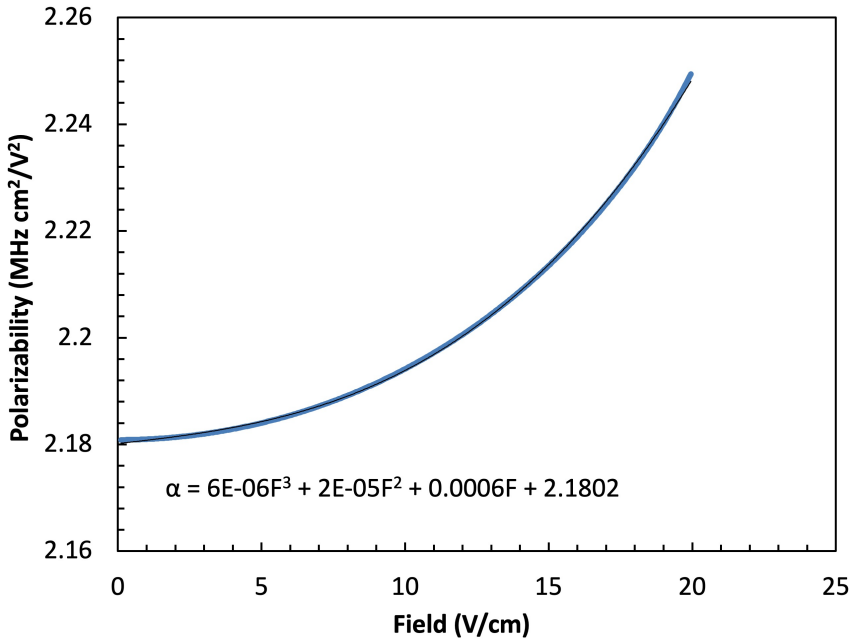

Figure 3.2: The Rubidium 32s state polarizability vs electric field. The expression in the graph is a polynomial fit illustrating how the polarizability changes with applied field. The polarizability changes by less than 1% for $10 < F < 15V/cm$.

Accordingly, within the adiabatic and quadratic Stark shift approximations, a low

angular momentum Rydberg state will experience a time-dependent energy

$$\begin{aligned} E(t) &= (E_0 - \frac{1}{2}\alpha F(t)^2) \\ \theta(t) &= -\int_0^t (E_0 - \frac{1}{2}\alpha F(t')^2)dt' \end{aligned} \tag{3.4}$$

in a slowly-varying total electric field,F(t), where E_0 is the field-free energy of the Rydberg state.

3.1 RF field determination with a DC reference

Consider a time-dependent field $\vec{F}(t)$ which is a superposition of static $\vec{F}_{dc}$ and harmonically varying $\vec{F}_{rf}\sin\omega t$ components. In that case,

$$E(t) = E_0 - \frac{1}{2}\alpha {F_{dc}}^2 - \alpha\vec{F}_{dc}\cdot\vec{F}_{rf}\sin\omega t - \frac{1}{2}\alpha {F_{rf}}^2\sin^2\omega t \tag{3.5}$$

Then, from equation(3.4),

$$\begin{aligned}\theta(t) &= -\int_0^t (E_0 - \frac{1}{2}\alpha F(t')^2)dt' \\ &= -\int_0^t (E_0 - \frac{1}{2}\alpha {F_{dc}}^2 - \alpha\vec{F}_{dc}\cdot\vec{F}_{rf}\sin\omega t' - \frac{1}{2}\alpha {F_{rf}}^2\sin^2\omega t')dt'\end{aligned} \tag{3.6}$$

According to Equation 3.1, the time-dependent wave function is

$$\begin{aligned}\psi(t) &= e^{i\theta(t)}\psi_0 \\ \psi(t) &= e^{-i(E_0+\Delta)t}e^{i\beta\cos\omega t}e^{i\gamma\sin 2\omega t}\psi_0\end{aligned} \tag{3.7}$$

where $\beta = \dfrac{\alpha F_{dc}F_{rf}\cos\phi}{\omega}$, ϕ is the angle between $\vec{F}_{rf}$ and $\vec{F}_{dc}$, $\gamma = \dfrac{\alpha F_{rf}^2}{8\omega}$, and the time-averaged Stark shift is

$$\Delta = -\frac{1}{2}\alpha {F_{dc}}^2 - \frac{1}{4}\alpha {F_{rf}}^2 \tag{3.8}$$

If we use the Jacobi-Anger expansion

$$e^{i\beta\cos\omega t} = \sum_{-\infty}^{\infty} i^n \mathbb{J}_n(\beta)e^{in\omega t} \tag{3.9}$$

$$e^{i\gamma \sin \omega t} = \sum_{-\infty}^{\infty} \mathbb{J}_n(\gamma) e^{in\omega t} \tag{3.10}$$

where $\mathbb{J}_n(x)$ is a Bessel function of the first kind of order n, then the wave function becomes,

$$\psi(t) = e^{-i(E_0+\Delta)t}(\sum_{-\infty}^{\infty} i^n \mathbb{J}_n(\beta) e^{in\omega t})(\sum_{-\infty}^{\infty} \mathbb{J}_m(\gamma) e^{i2m\omega t})\psi_0 \tag{3.11}$$

In general, $\psi(t)$ is a superposition of an infinite number of eigenstates all having the same spatial wavefunction, equally spaced eigenenergies separated by the RF frequency ω, and amplitudes depending on the static and RF field amplitudes through β and γ. The eigenstates form a spectral comb with energies $E_j = E_0 + \Delta + j\omega$ for integer values of j, with $-\infty \leq j \leq \infty$. The central eigenstate, corresponding to j=0, has an energy equal to the field free energy plus the time-averaged Stark shift. This primary or "main" Stark eigenstate is flanked by "sidebands" of order j. For relatively weak fields with $\beta,\ \gamma\ < 1$ the sideband amplitudes decrease rapidly with increasing $|j|$.

For $F_{dc} = 0$ or $\vec{F}_{dc} \perp \vec{F}_{rf}$ (i.e. for $\beta = 0$), only the even-order sideband states have non-zero amplitude. However, for $\gamma \ll 1$ (i.e. in a weak RF field for which the AC Stark shift is much less than the RF photon energy) these amplitudes are extremely small. The addition of a static reference field F_{dc} that is parallel to the RF field results in the creation of odd order sidebands that can have substantially larger amplitudes if $\beta \gg \gamma$. The enhancement of the sideband amplitudes, through the non-linear mixing within the detection atoms of a large reference field with a weak RF field, is the basis for the enhanced sensitivity of our non-resonant electrometer.

In the strong reference and weak RF field regime, there are three non-negligible absorption dips in the measured EIT spectrum: the central one is due to the primary

or "main" Stark state, flanked by the +/- first order sidebands at relative frequencies of $\pm\omega$, respectively. In the actual measurements, a fourth absorption dip appears at (or near) the zero-field resonance since the metal plates that create the fields within the cell do not extend to the entrance windows of the cell. Hence, a non-negligible fraction of the atoms do not experience the external electric fields. The presence of this "zero-field" dip serves as a convenient frequency reference for each EIT measurement. Fig. 3.3 illustrates the primary features in an EIT scan, plotted as transmission rather than absorption. In this case, the Rydberg resonances appear as peaks rather than dips. This terminology will be used for the remainder of this dissertation, i.e. it is assumed that the EIT spectrum is probe laser transmission vs coupling laser frequency.

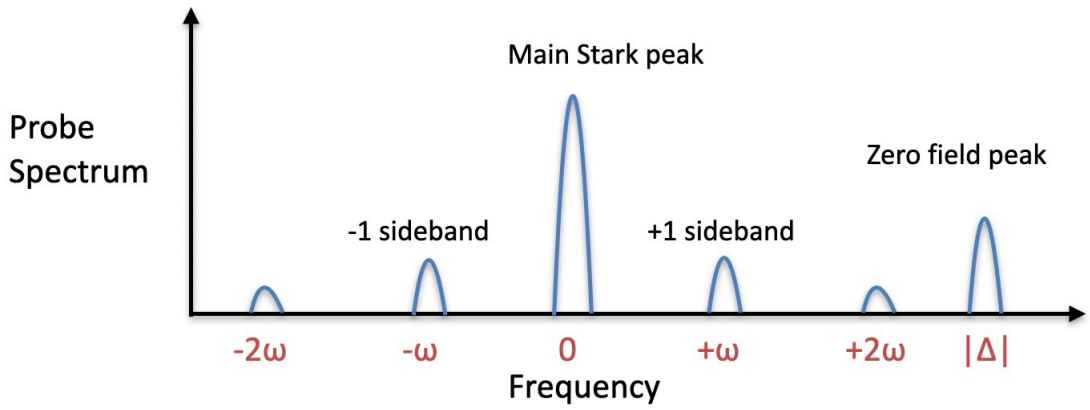

Figure 3.3: Depiction of an EIT spectrum obtained when the detection atoms are exposed to a strong DC reference and a weak RF field. For convenience we plot transmission rather than absorption.

We use the sideband separation in the presence of known static and RF fields to accurately calibrate the frequency axis for the EIT scans. The separation d between the plates in the cell can then be determined using the known applied DC voltage V_{dc}, the frequency splitting $|\Delta| = \frac{1}{2}\alpha(\frac{V_{dc}}{d})^2$ between the zero field peak and the main Stark peak obtained from an EIT scan with no reference, and the Rydberg polarizability

α, which can be calculated with high-accuracy. The measured value of d is then used to convert measured voltage to applied field for all subsequent measurements in the cell. Alternatively, if d has been accurately measured, α can be determined from the experimental values of V_{dc} and $|\Delta|$, rather than calculations.

3.1.1 Determining the RF field from sideband amplitudes

The amplitude a_0 of the primary Stark state, $j = n + 2m = 0$, is given by a sum of products of Bessel functions

$$\begin{aligned}(\sum i^n \mathbb{J}_n(\beta))(\sum \mathbb{J}_m(\gamma)) &= \sum_{-\infty}^{\infty} \mathbb{J}_m(\gamma)\mathbb{J}_{-2m}(\beta) i^{-2m} \\ &= \mathbb{J}_0(\gamma)\mathbb{J}_0(\beta) + \mathbb{J}_1(\gamma)\mathbb{J}_{-2}(\beta) + \mathbb{J}_{-1}(\gamma)\mathbb{J}_2(\beta) + ... \\ &= \mathbb{J}_0(\gamma)\mathbb{J}_0(\beta) + 2\mathbb{J}_1(\gamma)\mathbb{J}_2(\beta) + ...\end{aligned} \tag{3.12}$$

For the positive first order sideband with $j = n + 2m = 1$, the amplitude a_1 of the sideband state is

$$\begin{aligned}(\sum i^n \mathbb{J}_n(\beta))(\sum \mathbb{J}_m(\gamma)) &= \sum_{-\infty}^{\infty} \mathbb{J}_m(\gamma)\mathbb{J}_{1-2m}(\beta) i^{1-2m} \\ &= i\mathbb{J}_0(\gamma)\mathbb{J}_1(\beta) + i^{-1}\mathbb{J}_1(\gamma)\mathbb{J}_{-1}(\beta) + i^3\mathbb{J}_{-1}(\gamma)\mathbb{J}_{-3}(\beta) + ... \\ &= i(\mathbb{J}_0(\gamma)\mathbb{J}_1(\beta) + \mathbb{J}_1(\gamma)\mathbb{J}_1(\beta) + \mathbb{J}_1(\gamma)\mathbb{J}_3(\beta) + ...)\end{aligned} \tag{3.13}$$

For the negative first order sideband with $j = n + 2m = -1$, the amplitude a_{-1} of the sideband state is

$$\begin{aligned}
&(\sum i^n \mathbb{J}_n(\beta))(\sum \mathbb{J}_m(\gamma)) = \sum_{-\infty}^{\infty} \mathbb{J}_m(\gamma)\mathbb{J}_{-1-2m}(\beta) i^{-1-2m} \\
&= i^{-1}\mathbb{J}_0(\gamma)\mathbb{J}_{-1}(\beta) + i\mathbb{J}_{-1}(\gamma)\mathbb{J}_1(\beta) + i^{-3}\mathbb{J}_1(\gamma)\mathbb{J}_{-3}(\beta) + ... \\
&= -i(\mathbb{J}_0(\gamma)\mathbb{J}_1(\beta) - \mathbb{J}_1(\gamma)\mathbb{J}_1(\beta) - \mathbb{J}_1(\gamma)\mathbb{J}_3(\beta) - ....)
\end{aligned} \tag{3.14}$$

The amplitudes of the higher order sideband states can be calculated in an analogous fashion.

As described in Chapter 2, when scanning the coupling laser (at sufficiently low power) over an excited state to Rydberg resonance in an EIT measurement, the magnitude of the observed transmission peak is proportional to the square of the excited state to Rydberg transition dipole moment. In the presence of an external RF field (with or without a static field reference), peaks are observed at the primary Stark resonance and the associated sidebands. Since all of the states in the spectral comb share the same spatial wavefunction, the relative magnitudes of the various absorption dips are determined solely by the probability weighting $A_j = |a_j|^2$ of the constituent states in the dressed Rydberg wavefunction.

Specifically, the amplitudes of the transmission peaks associated with the $j = \pm 1$ sidebands are

$$\begin{aligned}
A_1 = |a_1|^2 = (\sum_{-\infty}^{\infty} \mathbb{J}_m(\gamma)\mathbb{J}_{-1-2m}(\beta) i^{-1-2m})^2 \\
A_{-1} = |a_{-1}|^2 = (\sum_{-\infty}^{\infty} \mathbb{J}_m(\gamma)\mathbb{J}_{1-2m}(\beta) i^{1-2m})^2
\end{aligned} \tag{3.15}$$

and the average amplitude of those two transmission sidebands is

$$\begin{aligned} A_\omega &= \frac{1}{2}(A_1 + A_{-1}) \\ &= \frac{1}{2}(\sum_{-\infty}^{\infty} \mathbb{J}_m(\gamma)\mathbb{J}_{-1-2m}(\beta)i^{-1-2m})^2 + (\sum_{-\infty}^{\infty} \mathbb{J}_m(\gamma)\mathbb{J}_{1-2m}(\beta)i^{1-2m})^2) \\ &= \frac{1}{2}((\mathbb{J}_0(\gamma)\mathbb{J}_1(\beta) + \mathbb{J}_1(\gamma)\mathbb{J}_1(\beta) + \mathbb{J}_1(\gamma)\mathbb{J}_3(\beta) + ...)^2 \\ &+ (\mathbb{J}_0(\gamma)\mathbb{J}_1(\beta) - \mathbb{J}_1(\gamma)\mathbb{J}_1(\beta) - \mathbb{J}_1(\gamma)\mathbb{J}_3(\beta) - ....)^2) \\ &= (\mathbb{J}_0(\gamma)\mathbb{J}_1(\beta))^2 + (\mathbb{J}_1(\gamma)\mathbb{J}_1(\beta))^2 + (\mathbb{J}_1(\gamma)\mathbb{J}_3(\beta))^2.... \end{aligned} \tag{3.16}$$

with the amplitude of the transmission peak due to the primary Stark state,

$$\begin{aligned} A_0 = |a_0|^2 &= (\sum_{-\infty}^{\infty} \mathbb{J}_m(\gamma)\mathbb{J}_{-2m}(\beta)i^{-2m})^2 \\ &= (\mathbb{J}_0(\gamma)\mathbb{J}_0(\beta))^2 + ... \end{aligned} \tag{3.17}$$

Cross terms proportional to $J_0(\gamma)$ that appear in $A_{1,-1}$ cancel in A_ω. As discussed in more detail below, this allows for an accurate determination of the amplitude of a small RF field by comparing the EIT measurements to calculations that use only a small number of terms in the series expansion for the sideband amplitudes.

Although it is not necessary for a full determination of the fields, for small F_{rf}, i.e. $\gamma \ll 1$ the expressions for $|a_j|^2$ for the primary Stark state and the sidebands can be greatly simplified while still retaining high accuracy. For example, in the approximation $\gamma = 0$, all terms involving $\mathbb{J}_j(\gamma)$ with $|j| > 0$ are zero, and $\mathbb{J}_0(\gamma) = 1$. Accordingly,

$$\begin{aligned} A_0 &\simeq (\mathbb{J}_0(\beta))^2 \\ A_\omega = A_{-1} = A_{+1} &\simeq (\mathbb{J}_1(\beta))^2 \end{aligned} \tag{3.18}$$

In practice, assuming $\gamma = 0$ is an excellent approximation if no second or higher order sidebands are visible in the EIT spectrum. That said, it is important to understand the accuracy of that approximation, as well as errors introduced by truncating the series expansions (Eqs. 3.14-3.17) for the main Stark peak and sideband amplitudes for $\gamma \neq 0$. Below we present the results of numerical calculations carrying out the relevant summations to different orders, m, to illustrate how the amplitudes of various spectral peaks are affected by truncation of the sum and the approximation $\gamma = 0$ as a function of γ and β.

Unless otherwise indicated, for the calculations shown in Figs. 3.4-3.7, the frequency of the RF field is 60 MHz, $F_{dc} = 14.7\text{V/cm}$, and $\vec{F}_{dc} \parallel \vec{F}_{rf}$. The polarizability of the 32s state of Rubidium, $\alpha = 2.19\text{MHz}/(\text{V/cm})^2$ is used to compute β and γ. All of the calculations are normalized so that $A_0 = 1$ for $F_{rf} = 0$, which ensures that the sum of the amplitudes of all peaks is 1 for any value of F_{rf}.

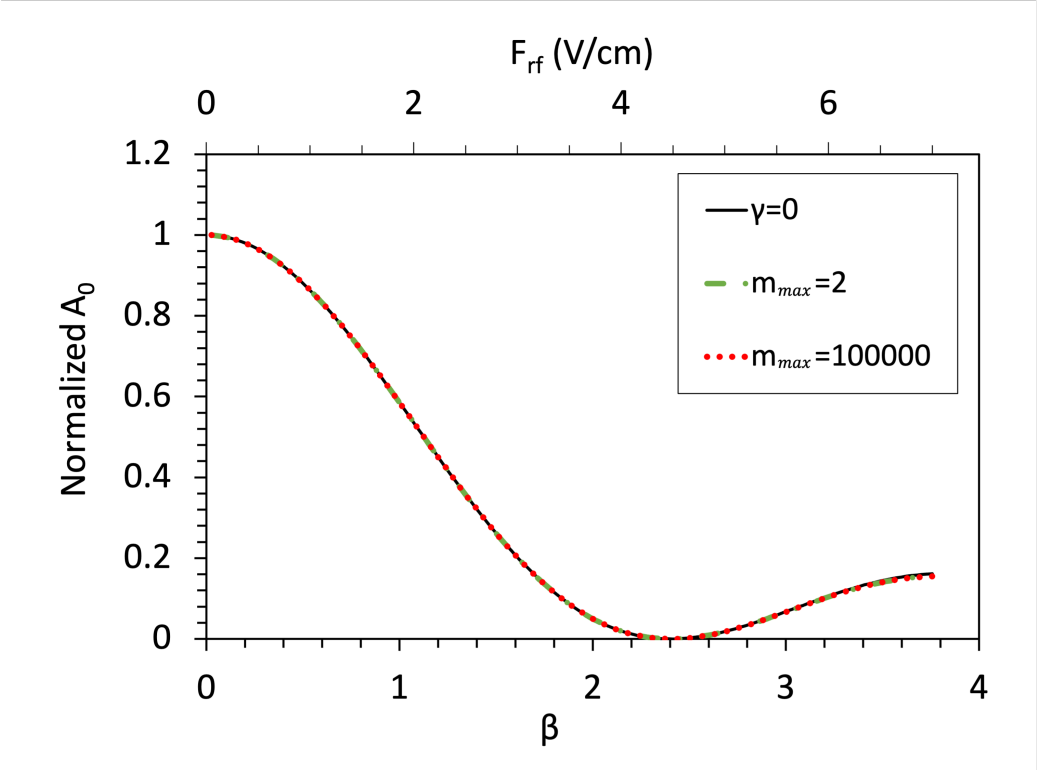

Figure 3.4: Main peak amplitude A_0 vs RF field and β. The red line shows the peak amplitude obtained from Eq. 3.17, including terms with $0 \leq |m| \leq 100000$ in the sum (effectively exact). The green line shows the result if only the leading order terms ($0 \leq |m| \leq 2$) are included. The black line shows the peak amplitude under the very weak RF field approximation, $\gamma = 0$ from Eq. 3.18. With increasing RF field, the Stark peak amplitude decreases as the sidebands increase in amplitude. The location of the first zero in A_0 serves to define the maximum RF field for which the $\gamma = 0$ approximation remains highly accurate, with $A_0 \simeq \mathbb{J}_0 = 0$ for $\beta = 2.40$.

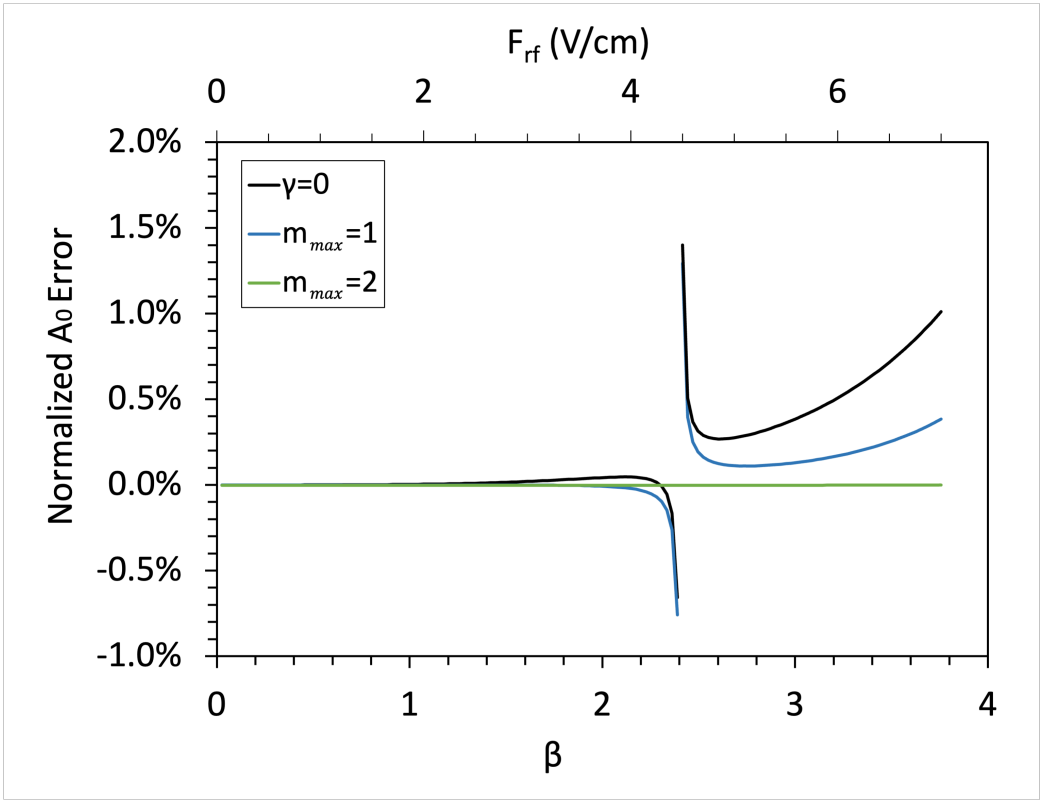

Figure 3.5: Main peak amplitude error, defined as the difference in the values of A_0 computed under various approximations from the "exact" expression using $m_{max} = 100000$ in the Bessel function expansion, vs β and F_{rf}. The green line shows the error if only the leading order terms ($0 \leq |m| \leq 2$) are included. The blue line shows the error for $0 \leq |m| \leq 1$). The black line shows the error of the peak amplitude under the weak RF field approximation, $\gamma = 0$ (from Eq. 3.18). The main peak amplitude error is smaller than 1% for $\beta \leq 2.40$.

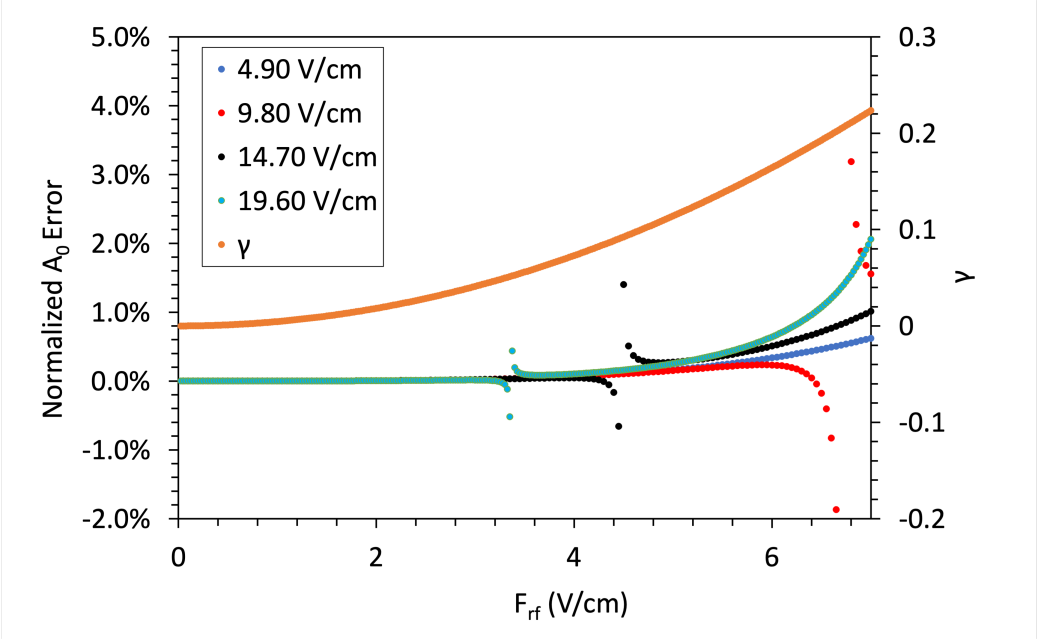

Figure 3.6: Main peak amplitude error, defined as the difference in the values of A_0 computed assuming $\gamma = 0$ and the "exact" expression using $m_{max} = 100000$ in the Bessel function expansion, vs F_{rf} for different DC fields: blue ($F_{dc} = 4.90$ V/cm), red ($F_{dc} = 9.80$ V/cm), black ($F_{dc} = 14.70$ V/cm), and green ($F_{dc} = 19.60$ V/cm). For $\beta \leq 2.40$, the $\gamma = 0$ approximation results in an error of less than 1%. The largest errors are found near $\beta \simeq 2.4$, i.e. for$F_{rf} = \dfrac{2.40\omega}{\alpha F_{dc}}$. For reference, the value of γ vs F_{rf} (right hand scale) is also shown. The value of γ for which the $\gamma = 0$ approximation holds increases with decreasing static field.

As shown in Figs. 3.5 and 3.6, for $\beta < 2.4$, the $\gamma = 0$ approximation holds with an error $\ll 1\%$ when $\beta < 2.40$. The limiting RF field in this situation is $F_{rf} = \dfrac{2.40\omega}{\alpha F_{dc}}$. The largest negligible $\gamma = \dfrac{\alpha F_{dc} F_{rf}}{8\omega} = \dfrac{0.72\omega}{\alpha F_{dc}^2}$ is determined by the RF field frequency, the state polarizability and the DC reference field.

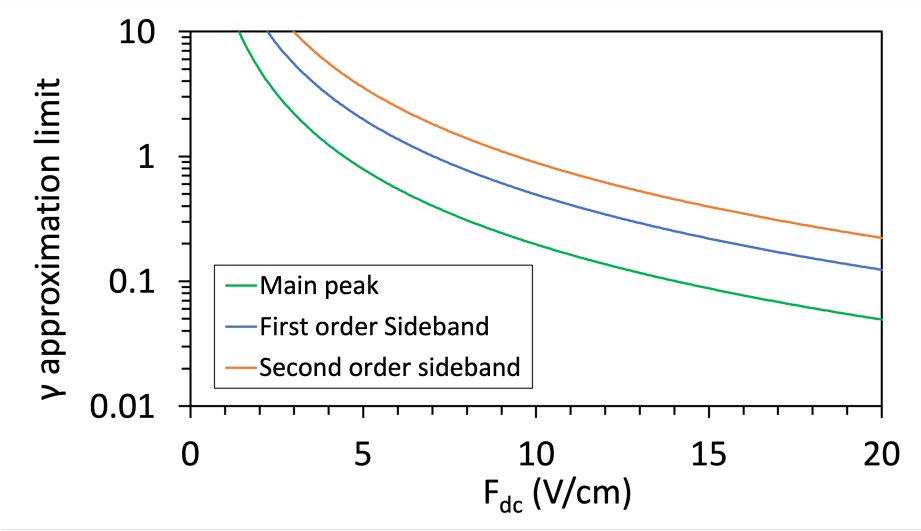

Figure 3.7: Value of γ above which the error in the $\gamma = 0$ approximation exceeds 1% vs F_{dc} for an RF frequency of 60MHz. Cutoff γ values for the 1st and 2nd order sidebands (blue and orange, respectively) are larger than those for A_0 (green), due to the larger β values at the higher order sideband zeros.

Similarly, the limits of the $\gamma = 0$ approximation can be derived for the EIT sidebands in Fig. 3.7.

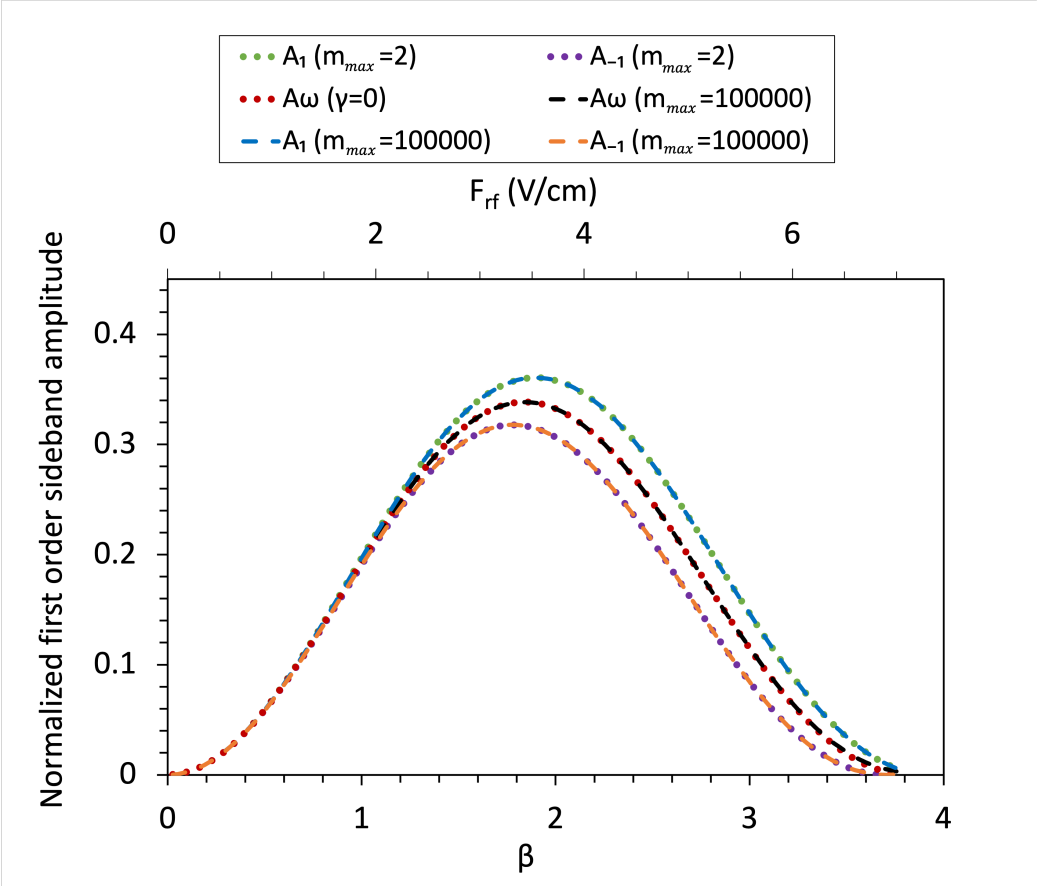

Figure 3.8: Normalized first order sideband amplitudes $A_{\pm 1}$ and A_ω vs β and RF field. The A_1 and A_{-1} curves are obtained from equation (3.15), and are plotted for two different values of the maximum index $|m_{max}|$ included in the sum. The calculated peak amplitudes with $|m_{max}| = 100000$ are overlapped with those obtained for $|m_{max}| = 2$. The average sideband amplitude A_ω, calculated from Eq. 3.16 is in excellent agreement with the value from Eq. 3.18, which assumes $\gamma = 0$. Note that $A_1 = A_{-1}$ for $\gamma = 0$, so this approximation clearly breaks down for $F_{rf} > 1.5$ V/cm. However, as noted earlier in this section, due to the cancellation of leading order cross-terms, $\gamma = 0$ remains a good approximation for A_ω out to significantly larger RF fields.

The error of the $\gamma = 0$ approximation for the first order sideband amplitudes $A_{1,-1}$ and their average A_ω is shown in Fig. 3.9. For $\gamma = 0$, $A_{1,-1} = A_\omega = (\mathbb{J}_1(\beta))^2$. The first zero of $\mathbb{J}_1(\beta)$ (for positive β) appears at $\beta = 3.83$.

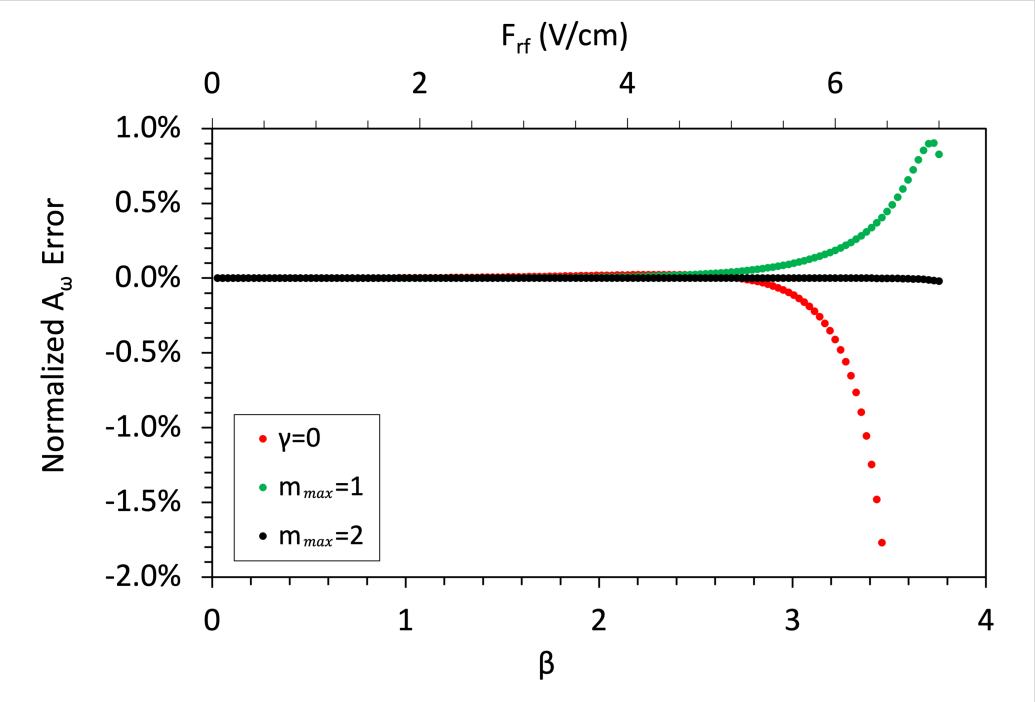

Figure 3.9: Error in average first order sideband amplitude A_ω vs β and RF field. The normalized A_ω for $m_{max} \leq 100000$ is assumed to be"exact." The black dots show the error for $m_{max} = 2$ and the green dots show the error $m_{max} = 1$. The red dots show the error for $\gamma = 0$, from Eq. 3.18. The average sideband amplitude error for $\gamma = 0$ is less than 0.1% when $\beta \leq 2.40$ (at the first zero in A_0 where the $\gamma = 0$ approximation fails for A_0), and smaller than 1% for $\beta \approx 3.40$, 2% for $\beta \approx 3.60$(where A_ω approaches zero).

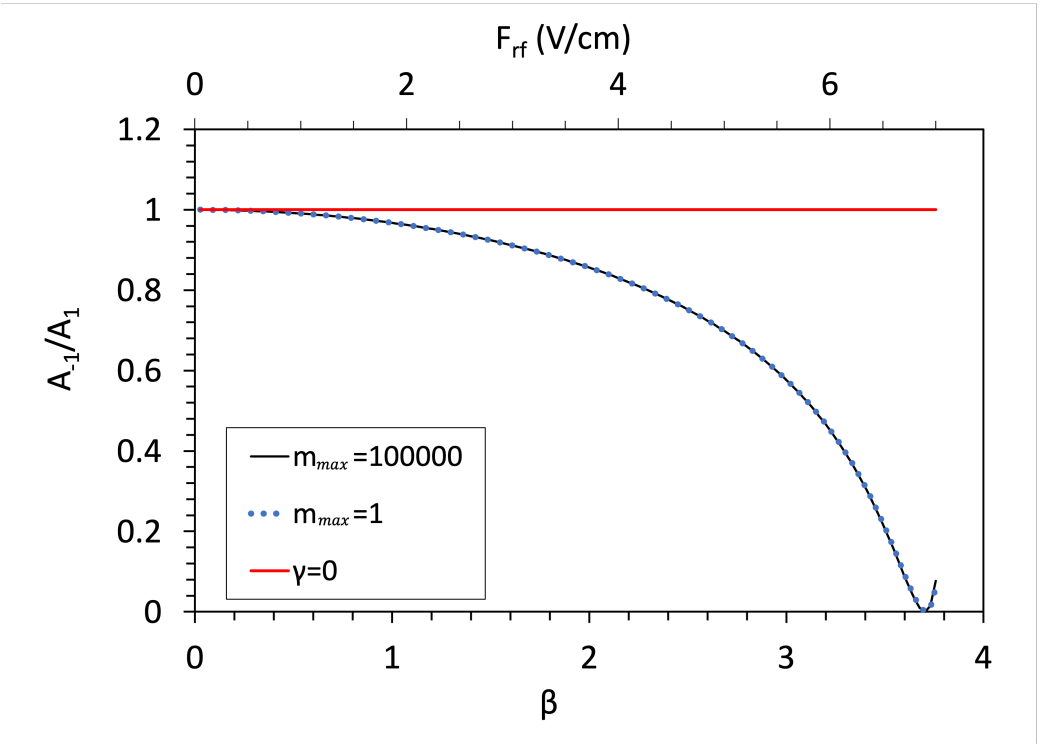

Figure 3.10: Calculated ratio A_{-1}/A_1 vs β and RF field, for $|m_{max}| = 100000$ and $|m_{max}|$=1. For $\gamma = 0$ (red line), the ratio is equal to 1 for all F_{rf}. For this range of β, the difference between A_{-1} and A_1 is mainly due to the first cross term $\mathbb{J}_1(\beta)\mathbb{J}_1(\gamma)$, as shown by the good agreement between the blue dotted (m_{max}=1) and black (m_{max}=100000) lines.

To determine the RF field from the EIT spectrum and the known value of F_{dc}, we compare the measured value of A_ω/A_0 to the analytic expression for that ratio in terms of β and γ,

$$\frac{A_\omega}{A_0} = \frac{(\mathbb{J}_0(\gamma)\mathbb{J}_1(\beta))^2 + (\mathbb{J}_1(\gamma)\mathbb{J}_1(\beta))^2 + ...}{(\mathbb{J}_0(\gamma)\mathbb{J}_0(\beta))^2 + ...} \tag{3.19}$$

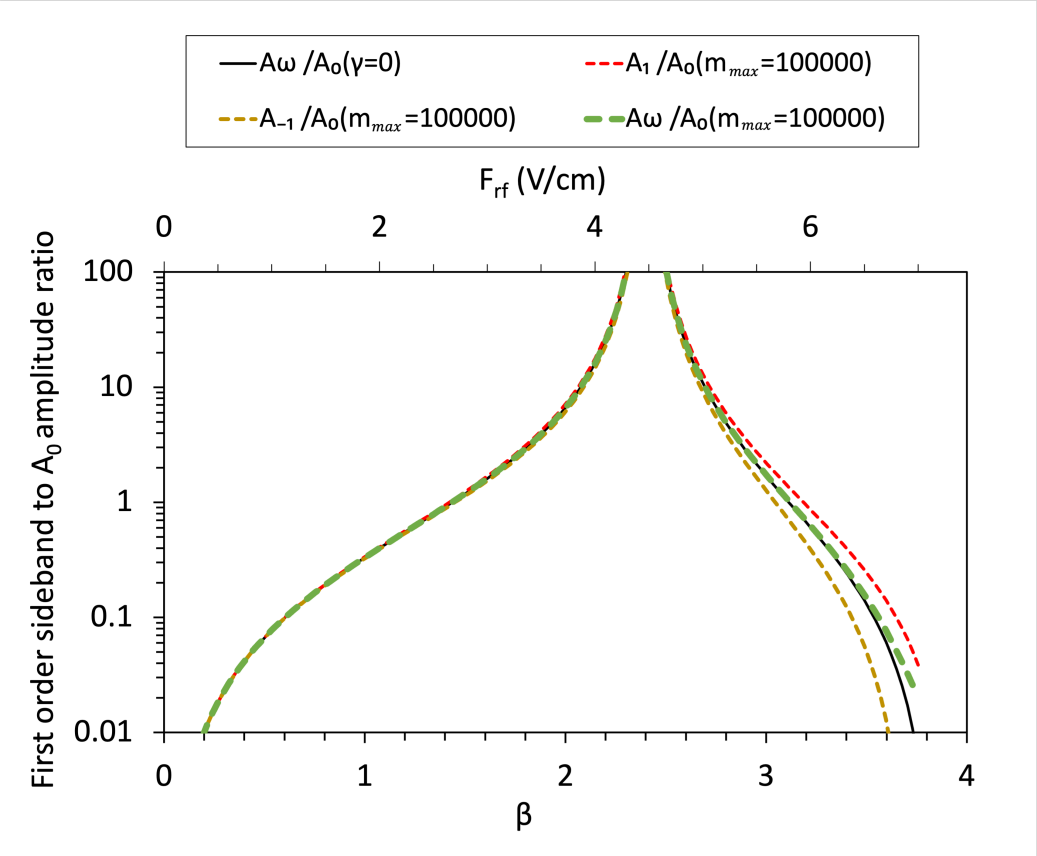

Figure 3.11: Calculated ratio of the average first order sideband to main Stark peak amplitudes vs β and RF field. The green, red, and brown curves are calculated using $|m_{max}| = 100000$. The black line (overlapped with the green line) is calculated for γ=0, demonstrating the accuracy of that approximation (less than 1% error) for F_{rf} < 5.1 V/cm (i.e. $\beta < 2.7$, not including $\beta \approx 2.4$ where A_0 approaches zero.)

For relatively weak RF fields ($\beta \leq 2.40$) (as shown in Figs. 3.5 and 3.6), we can use the $\gamma = 0$ approximation and obtain accurate values for F_{rf} from the simpler approximate expression

$$\frac{A_\omega}{A_0} \cong \frac{\mathbb{J}_1(\beta)^2}{\mathbb{J}_0(\beta)^2} \tag{3.20}$$

Hence, the ratios of the various transmission peaks in the EIT spectrum give direct access to the applied fields.

For very small β, a power series expansion of the the Bessel functions can be used to obtain analytic expressions for β and F_{rf} in terms of A_ω/A_0. Specifically, inserting the expansion

$$\mathbb{J}_v(\beta) = \sum_{k=0}^{\infty} \frac{(-1)^k(\beta/2)^{v+2k}}{k!(v+k)!} \tag{3.21}$$

into Eq. 3.20,

$$\sqrt{\frac{A_\omega}{A_0}} \cong \frac{\mathbb{J}_1(\beta)}{\mathbb{J}_0(\beta)} \cong \frac{\beta/2 - \beta^3/16 + ...}{1 - \beta^2/4 + \beta^4/64 + ...} \cong \frac{\beta}{2} + \frac{\beta^3}{16} - \frac{3\beta^5}{128} + \mathcal{O}\big(\beta^7\big) \tag{3.22}$$

Accordingly, we can numerically solve for $\beta = \dfrac{\alpha F_{dc} F_{rf}}{\omega}$ from the the full Bessel expansion (Eq. 3.19) or from the $\gamma = 0$ approximation (Eq. 3.20), or analytically using Eq. 3.22. If β sufficiently small so that terms of order β^3 and higher can be ignored compared to β, we obtain the simple expression

$$F_{rf} = \frac{\omega}{\alpha F_{dc}}\beta = \frac{2\omega}{\alpha F_{dc}}\sqrt{\frac{A_\omega}{A_0}} \tag{3.23}$$

Figure 3.12 shows how different approximations affect the results.

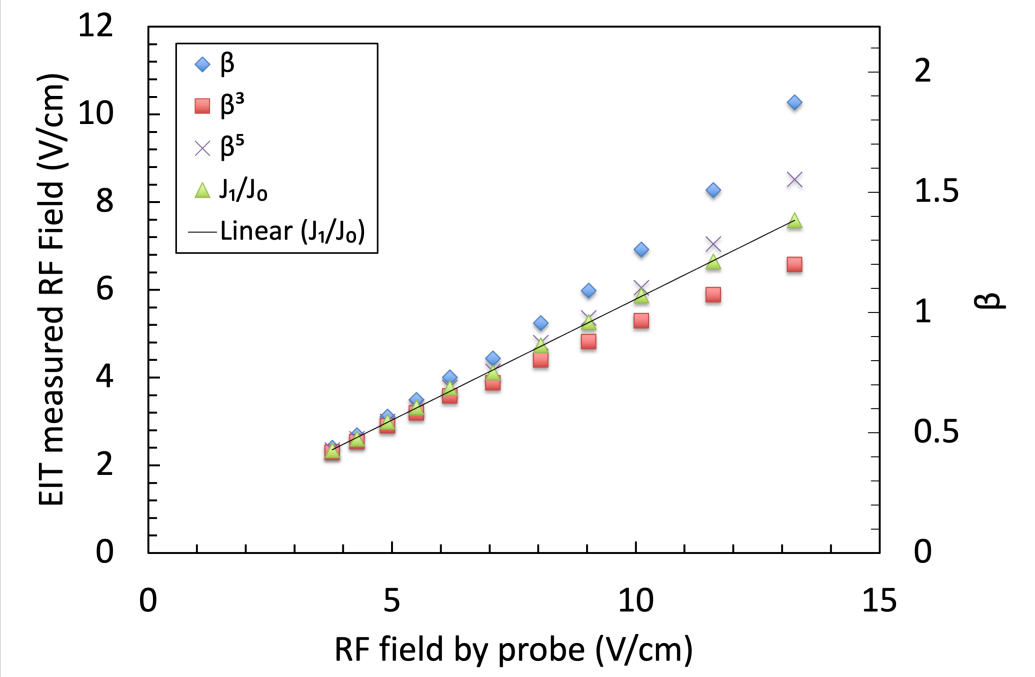

Figure 3.12: Comparison of RF fields measured via a high impedance probe and via EIT using different levels of approximation for the peak amplitude ratios in terms of β (see Eq. 3.22). The Rb 25s state is used for detection (rather than 32s) due to its smaller polarizability, $\alpha = 0.372$ MHz/(V/cm)^2 and larger detectable F_{rf} range. The DC reference is $F_{dc} = 29.4$V/cm. The blue dots (including terms proportional to β) clearly curves up while the red dots (terms up to β^3) curves down. The crosses (terms up to β^5) curves up again. The green dots (from $\mathbb{J}_1/\mathbb{J}_0$) show the expected linear relationship between the EIT and probe measurements. For lowest data point $\beta = 0.42$, the error resulting from keeping terms linear in β only is 2.2% relative to the full Bessel function solution.

For very weak RF fields ($\beta \leq 0.2$), the value for F_{rf} as determined directly from the simple expression in Equation (3.23) is within 1% of that determined numerically from the Bessel function expression $\mathbb{J}_1(\beta)/\mathbb{J}_0(\beta)$.

Fig. 3.4 shows that with increasing F_{rf}, A_0 decreases from 1 and falls to zero at an RF field strength corresponding to $\beta \approx 2.40$. As shown in Figs. 3.5 and 3.6, the error in the $\gamma = 0$ approximation is particularly large near this zero. Rather than resort to a numerical solution of the full Bessel function expansion, one can determine F_{rf}

using ratios of sideband peaks of higher orders, for which the $\gamma = 0$ approximation is still valid. For example, near the first zero in A_0 there are $\pm 2\omega$ sideband peaks with significant amplitude, and the field amplitude can be readily extracted from the EIT spectrum using the ratio $A_{2\omega}/A_{\omega}$, where $A_{2\omega}$ is the average amplitude of the two second order sidebands, $A_{\pm 2}$.

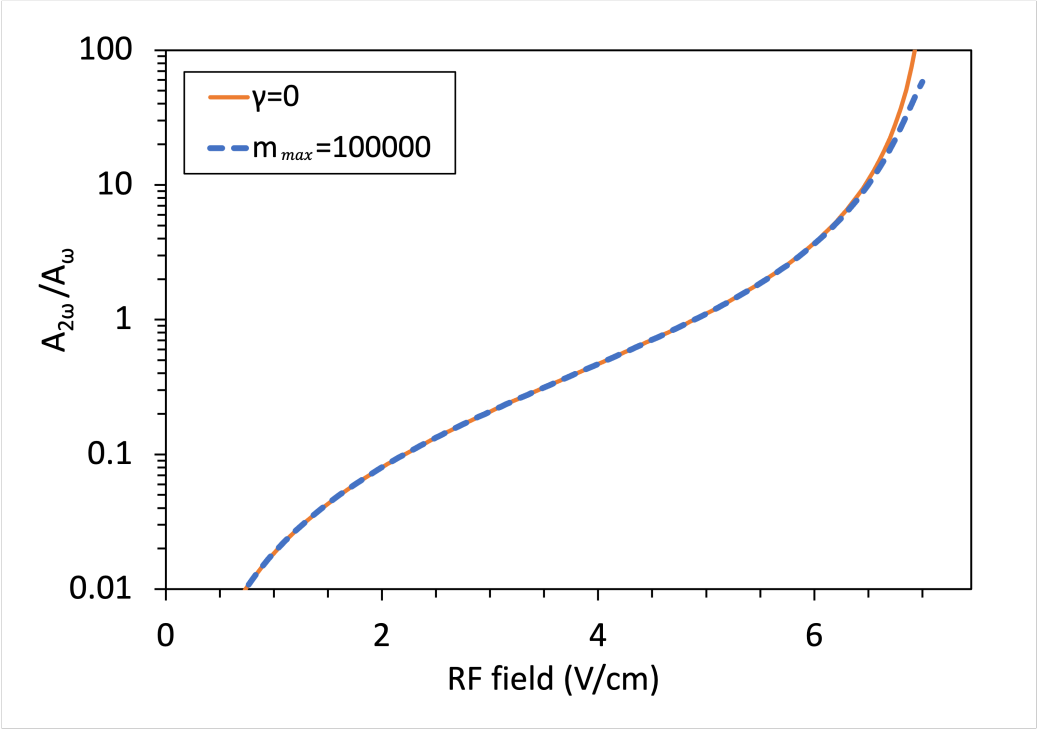

Figure 3.13: Calculated ratio of the average 2ω to ω sideband amplitudes vs RF field. The blue line is calculated using $m_{max} = 100000$. The red line (overlapped with the blue line) is calculated assuming $\gamma = 0$. The difference between the two lines becomes larger than 1% when $F_{rf} \geq 5.85$ (i.e. $\beta \geq 3.13$) due to the zero in A_{ω}.

As shown in Fig. 3.13, in the range $\beta \geq 2.40$ (main peak amplitude close to zero) and $\beta \leq 3.13$ (first sideband peak amplitude close to zero), we can utilize the amplitude ratio between the average $\pm 2\omega$ sideband and the average $\pm\omega$ sideband to solve for RF field.

$$\frac{A_{2\omega}}{A_{\omega}} = \frac{\mathbb{J}_2(\beta)^2}{\mathbb{J}_1(\beta)^2} \tag{3.24}$$

This expression, or analogous ones for higher order sidebands, can be used determine RF fields which are too large to be simply extracted from the amplitude ratio of the first order sidebands and the main Stark peak, but yet too small to be measured directly from the average Stark shift, Δ, within the EIT linewidth.

As alluded to above, higher order sidebands that appear in the spectrum can be used to measure larger RF fields. If sidebands up to order $j+1$ are visible in the EIT spectrum, then we can approximate

$$\frac{A_{(j+1)\omega}}{A_{j\omega}} = \frac{\mathbb{J}_{j+1}(\beta)^2}{\mathbb{J}_j(\beta)^2} \tag{3.25}$$

to determine F_{rf} within the $\gamma = 0$ approximation.

As noted previously, while making the $\gamma = 0$ approximation makes the relevant expressions relating F_{rf} to the EIT peak amplitudes particularly simple, it is always straightforward to numerically solve Eq. 3.19 (or analogous expressions for higher order sideband ratios), setting $m_{max} \geq 2$ for high accuracy. This can be readily accomplished with MATLAB or Mathematica.

3.1.2 RF field with Zero DC field

For measuring moderately strong RF fields, a DC reference field is not necessary. When $F_{dc} = 0$, only even-order sideband states have non-zero amplitude. In this case the eigenstate in Eq. 3.11 simplifies to

$$\psi(t) = e^{-i(E_0 - \alpha {F_{rf}}^2/4)} \sum \mathbb{J}_n(\gamma) e^{i2n\omega t} \psi_0 \tag{3.26}$$

In the moderately strong to strong RF field range, there can be several non-negligible

peaks in the EIT transmission spectrum: the center one is due to the primary or "main" Stark state, flanked by sidebands at relative frequencies of $\pm 2n\omega$, along with the "zero-field" peak.

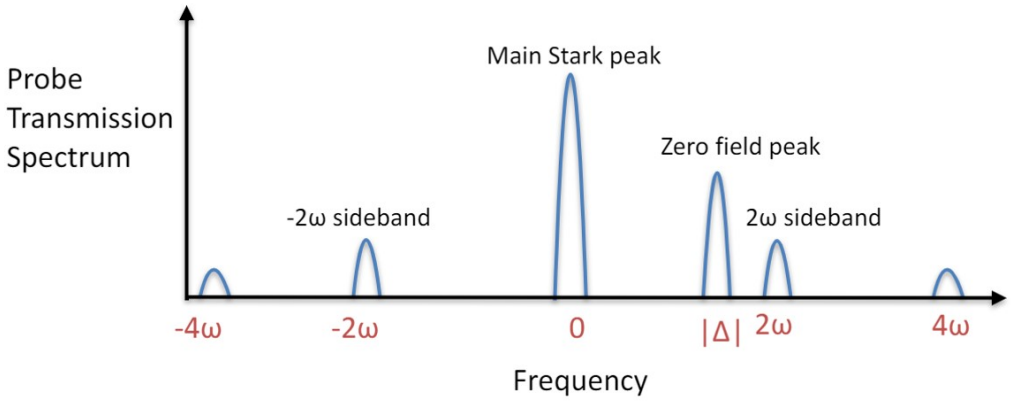

Figure 3.14: Characteristic EIT spectrum for a moderately strong RF field alone. For larger RF fields, additional sidebands at integer multiples of $\pm 2\omega$ would also be observed.

Fig. 3.14 illustrates the primary features in an EIT scan, plotted as transmission rather than absorption. Sufficiently strong RF fields can be measured directly from the known polarizability α and the frequency separation $\Delta = -\alpha {F_{rf}}^2/4$ between the main Stark peak and the zero field peak in the EIT spectrum,

$$F_{rf} = \sqrt{\frac{4|\Delta|}{\alpha}} \tag{3.27}$$

Alternatively, if the widths of the EIT peaks are too broad to accurately determine the Stark shift, F_{rf} can be extracted from spectral peak amplitude ratios, analogous to the approach used with the static reference. For this, one can use expressions for the amplitudes of the primary Stark state and sidebands in terms of Bessel functions

of argument γ,

$$\begin{aligned} A_0 &= (\mathbb{J}_0(\gamma))^2 \\ A_{2\omega} &= A_{-2\omega} = (\mathbb{J}_1(\gamma))^2 \end{aligned} \tag{3.28}$$

F_{rf} can then be determined from $\gamma = \dfrac{\alpha F_{rf}^2}{8\omega}$ and the value of γ that solves the amplitude ratio,

$$A_{2\omega}/A_0 = (\mathbb{J}_1(\gamma))^2/(\mathbb{J}_0(\gamma))^2 \tag{3.29}$$

for the measured EIT peak amplitudes $A_{2\omega}$ and A_0.

3.2 RF field determination with an RF reference

A known RF field F_1 can be used as an alternative to the static reference to detect a small signal RF field F_2. For this case, the applied electric field is: $\vec{F}(t) = \vec{F_1}\sin\omega_1 t + \vec{F_2}\sin\omega_2 t$. In the adiabatic limit, the Stark shift in such a field is

$$\begin{aligned}\Delta E &= -\frac{1}{2}\alpha(\vec{F_1}\sin\omega_1 t + \vec{F_2}\sin\omega_2 t)^2 \\ &= -\frac{1}{2}\alpha(F_1^2\sin^2\omega_1 t + F_2^2\sin^2\omega_2 t + 2\vec{F_1}\cdot\vec{F_2}\sin\omega_1 t\sin\omega_2 t) \\ &= -\frac{1}{4}\alpha[(F_1^2+F_2^2) - F_1^2\cos 2\omega_1 t - F_2^2\cos 2\omega_2 t + \\ &\quad 2\vec{F_1}\cdot\vec{F_2}(\cos(\omega_1-\omega_2)t - \cos(\omega_1+\omega_2)t)]\end{aligned} \tag{3.30}$$

The wave function can be written as,

$$\begin{aligned}&\psi(t) = e^{i\theta(t)}\psi_0 \\ &\theta(t) = -\int_0^t (E_0+\Delta E)dt' \\ &\psi(t) = e^{-i(E_0+\Delta)t}e^{-i\beta_-\sin(\omega_1-\omega_2)t} \\ &\cdot e^{i\beta_+\sin(\omega_1+\omega_2)t}e^{i\gamma_1\sin 2\omega_1 t}e^{i\gamma_2\sin 2\omega_2 t}\psi_0\end{aligned} \tag{3.31}$$

where $\beta_\pm = \dfrac{\alpha\vec{F_1}\cdot\vec{F_2}}{2(\omega_1\pm\omega_2)}$, $\gamma_{1,2} = \dfrac{\alpha F_{1,2}^2}{8\omega_{1,2}}$ and $\Delta = -\dfrac{1}{4}\alpha {F_1}^2 - \dfrac{1}{4}\alpha {F_2}^2$.

For strong reference and weak signal fields $F_1 \gg F_2$, $\gamma_1 \gg \gamma_2$, and the wave function can be simplified by setting $\gamma_2 = 0$,

$$\begin{aligned}\psi(t) &= e^{-i(E_0+\Delta)t}e^{i\beta_-\sin(\omega_1-\omega_2)t}e^{i\beta_+\sin(\omega_1+\omega_2)t}e^{i\gamma_1\sin 2\omega_1 t}\psi_0 \\ &= e^{-i(E_0+\Delta)t}\Big(\sum \mathbb{J}_n(\beta_-)e^{in(\omega_1-\omega_2)t}\Big)\Big(\sum \mathbb{J}_k(\beta_+)e^{ik(\omega_1+\omega_2)t}\Big)\Big(\sum \mathbb{J}_m(\gamma_1)e^{im2\omega_1 t}\Big)\psi_0\end{aligned} \tag{3.32}$$

We will assume that we are working in the weak signal field regime for the remainder of this analysis.

The form of the wavefunction in Eq. 3.32 results in multiple peaks in the measured EIT spectrum. If the reference field is not very strong the prominent features in the EIT spectrum will be the main Stark shifted peak, a pair of "difference frequency" sidebands split from the main peak by $\delta = |\omega_1 - \omega_2|$, pair of "sum frequency" sidebands split by $\sigma = (\omega_1 + \omega_2)$ away from the main peak, and pair of "second harmonic" sidebands split by $2\omega_1$ about the main peak. All of these features are the result of non-linear mixing of the applied fields within the Rydberg atoms, due to the 2nd order Stark shift.

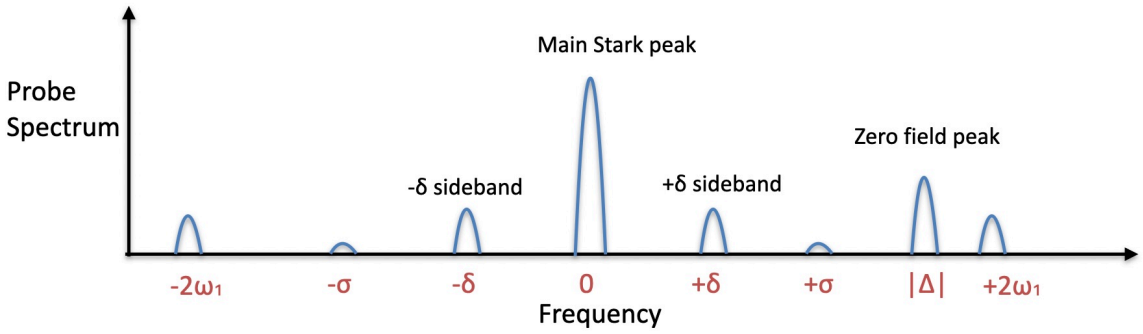

Figure 3.15: Depiction of the EIT transmission spectrum when the detection atoms are exposed to moderately strong RF reference and weak RF signal fields.

The main peak amplitude and average first order sideband amplitudes at the various frequencies can be calculated using an approach completely analogous to that used

for the DC reference case,

$$\begin{aligned} A_0 &= (\mathbb{J}_0(\gamma_1)(\mathbb{J}_0(\beta_-)(\mathbb{J}_0(\beta_+))^2 + ... \\ A_{2\omega} &= (\mathbb{J}_1(\gamma_1)(\mathbb{J}_0(\beta_-)(\mathbb{J}_0(\beta_+))^2 + ... \\ A_\delta &= (\mathbb{J}_0(\gamma_1)(\mathbb{J}_1(\beta_-)(\mathbb{J}_0(\beta_+))^2 + ... \\ A_\sigma &= (\mathbb{J}_0(\gamma_1)(\mathbb{J}_0(\beta_-)(\mathbb{J}_1(\beta_+))^2 + ... \end{aligned} \tag{3.33}$$

With appropriate selection of the reference field frequency, $\omega_1 \simeq \omega_2$, so that the sum frequency $\sigma = (\omega_1 + \omega_2)$ is much greater than the difference frequency $\delta = |\omega_1 - \omega_2|$. In this case, $\beta_- \gg \beta_+$ and the amplitude of the difference frequency sidebands will be much larger than the sum frequency sideband. Indeed, with proper choice of the F_1 and ω_1, we can approximate $\beta_+ = 0$ (similar to the $\gamma = 0$ approximation for the static field reference). This greatly simplifies the expressions for the amplitudes of the main Stark peak and difference frequency sidebands, while retaining high accuracy

$$\begin{aligned} A_0 &= (\mathbb{J}_0(\gamma_1)(\mathbb{J}_0(\beta_-))^2 + ... \\ A_\delta &= (\mathbb{J}_0(\gamma_1)(\mathbb{J}_1(\beta_-))^2 + (\mathbb{J}_1(\gamma_1)(\mathbb{J}_1(\beta_-))^2 + ... \end{aligned} \tag{3.34}$$

As in the static reference case, cross terms proportional to $\mathbb{J}_n(\gamma_1)$ cancel in the average amplitude of the difference frequency sidebands. So, the ratio of the average amplitude of the difference frequency sidebands to the main Stark peak amplitude depends on β_- only,

$$\frac{A_\delta}{A_0} = \frac{(\mathbb{J}_0(\gamma_1)(\mathbb{J}_1(\beta_-))^2 + ...}{(\mathbb{J}_0(\gamma_1)(\mathbb{J}_0(\beta_-))^2 + ...} \cong \frac{\mathbb{J}_1(\beta_-)^2}{\mathbb{J}_0(\beta_-)^2} \tag{3.35}$$

Accordingly, the signal field amplitude F_2 can be directly computed from that ratio.

In the extreme weak signal field limit ($\beta_- \leq 0.2$), we can expand the Bessel function expressions using Eq. 3.21 to obtain

$$\sqrt{\frac{A_\delta}{A_0}} \cong \frac{\mathbb{J}_1(\beta_-)}{\mathbb{J}_0(\beta_-)} \cong \frac{\beta_-/2 - \beta_-^3/16 + ...}{1 - \beta_-^2/4 + \beta_-^4/64 + ...} \cong \frac{\beta_-}{2} + \frac{\beta_-^3}{16} - \frac{3\beta_-^5}{128} + \mathcal{O}(\beta_-^7) \tag{3.36}$$

The component of the signal RF field $\vec{F}_2$ that is parallel to $\vec{F}_1$ can then be calculated as,

$$F_{2,\parallel} = \frac{2\delta}{\alpha F_1}\beta_- = \frac{4\delta}{\alpha F_1}\sqrt{\frac{A_\delta}{A_0}} \tag{3.37}$$

Note that F_1 can be independently measured from the EIT spectrum using the Stark shift when F_2 is not in present, or is negligibly small (see Eq. 3.27).

Chapter 4

Experimental results

In this Chapter, we describe the details of our experimental approach and present data demonstrating the effectiveness of the self-calibrating broadband Rydberg electrometer. Our initial measurements utilized standard EIT spectroscopy and continuous wave (cw) lasers. The non-linearity in the amplitude of the EIT transmission peaks as a function of coupling laser intensity, even at low intensities, led to our development of a pulsed approach that both alleviated the non-linearity and enhanced our field sensitivity through lock-in detection. The details of the pulsed EIT scheme are described along with other approaches utilizing strong low-frequency AC and RF reference fields that, in principle, eliminate the need for field plates within the measurement cell, and substantially reduce the required scan range of the coupling laser frequency for measurements of higher frequency fields. Use of an RF reference can also significantly enhance the detection sensitivity for RF frequencies much greater than the spectral width of the EIT transmission peaks.

4.1 Continuous laser EIT spectrum

We begin the discussion of our Rydberg EIT measurements, and testing of the electrometer scheme, with a description of our initial approach which used cw probe and coupling lasers and a static reference field in combination with a weak RF signal field. We first confirmed that, η, the square root of the ratio of the measured amplitudes of the lowest order EIT sidebands to the primary Stark peak was proportional to the RF field in the Rb cell, F_{rf}. However, we found that the non-linearity of the amplitude of the primary Stark peak with increasing coupling laser power (P_c) resulted in an intensity-dependent constant of proportionality between η and F_{rf}. That intensity dependence was eliminated through the use of sufficiently short coupling laser pulses in the following section.

4.1.1 Experiment Setup

Fig. 4.1 shows a schematic of the experimental apparatus for an EIT-based Rydberg electrometer employing cw laser beams. In the figure, the upper Rb cell enables saturated absorption locking of the 780 nm probe laser frequency. The EIT measurements are performed in the lower Rb cell which contains parallel metal plates for the creation of uniform static and/or RF fields. In principle, since the applied fields have a negligible effect on the Rb 5s and 5p states, both the saturated absorption and EIT measurements could be made in the EIT cell to reduce the footprint of the apparatus.

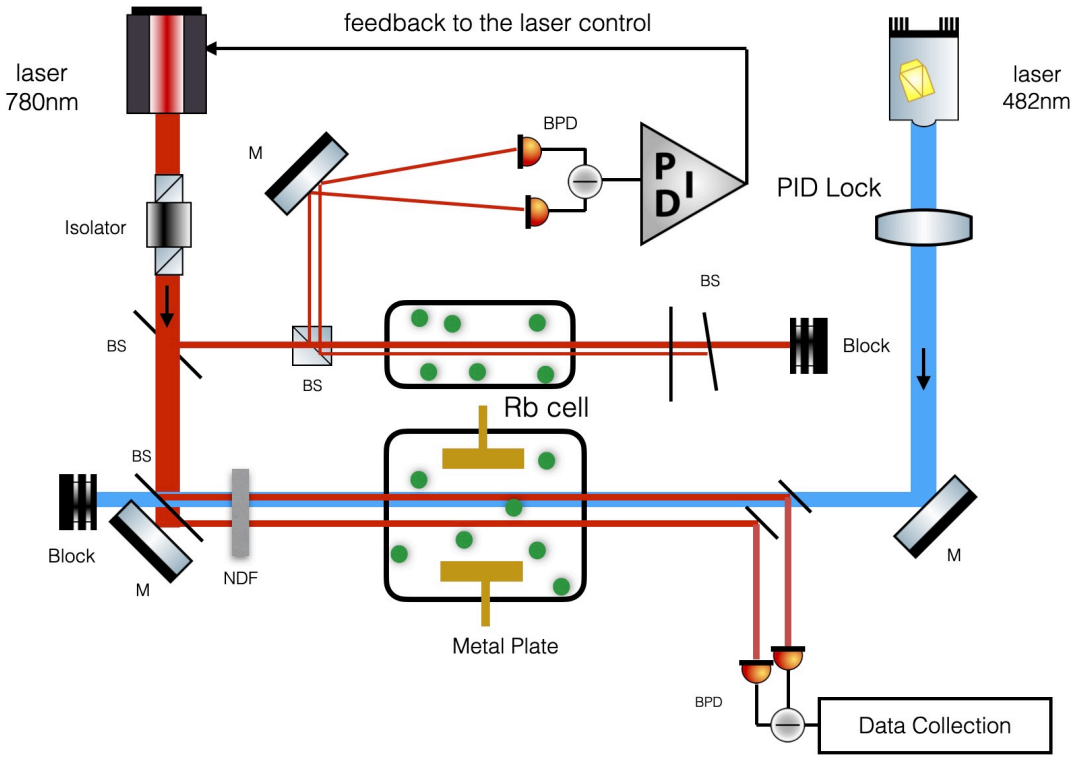

Figure 4.1: Schematic of the experimental apparatus for an EIT-based Rydberg electrometer employing cw laser beams. The upper Rubidium cell is used for saturated absorption locking of the 780nm laser frequency. The EIT spectroscopy is performed in the lower Rb cell, with counter-propagating probe and coupling laser beams interacting with Rb atoms between two parallel field plates.

4.1.2 DC and RF mixing field spectrum

Fig. 4.2 shows two EIT spectra used to detect weak RF fields in the presence of an additional known static reference field. As the coupling laser frequency is scanned changes in the absorption of the probe laser are measured using a balanced photodiode detector. The probe laser Rabi frequency is 1.1MHz and the coupling laser Rabi frequency is 4.2MHz (details shown in Appendix A.2). The red spectrum clearly shows the primary features illustrated in Fig. 3.1, for the detection of a weak RF field in

the presence of a strong DC reference. The largest dip, centered at 0MHz is due to the primary Stark resonance. As described in the previous chapter, the amplitudes of the two small sidebands flanking the Stark dip at ±90MHz, in combination with the main Stark dip, reveal the spectral amplitude of the RF field. The blue trace is obtained with the same DC reference but with a dual frequency RF signal field (50MHz + 90MHz). The spectral amplitude of the field can again be determined directly from the ratio of the amplitudes of the sidebands to the primary Stark dip.

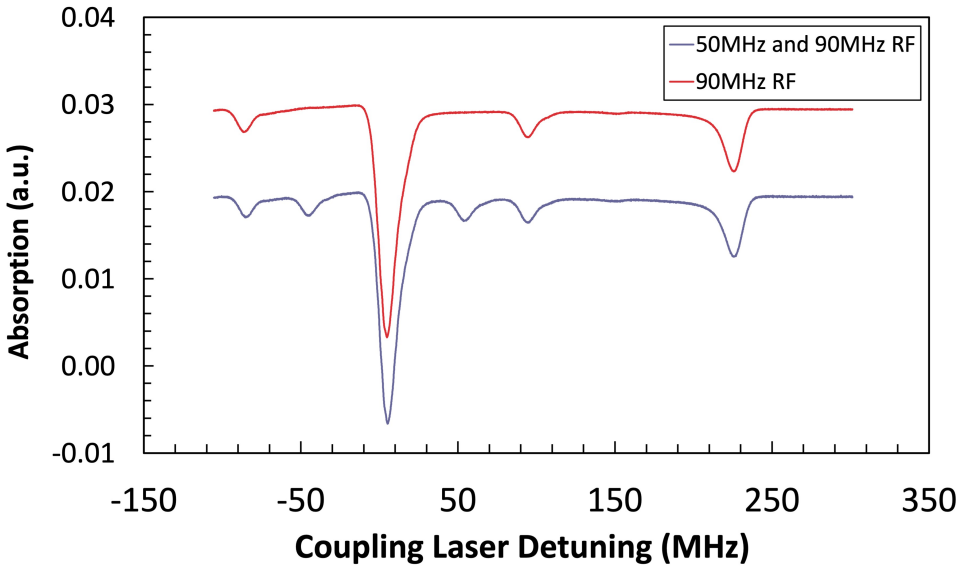

Figure 4.2: EIT spectra in the presence of RF signal and DC reference fields. The traces shown here are the average of 250 coupling laser frequency scans which are collected at a sweep rate of approximately 10 Hz for two different signal RF fields. The DC reference field is 14.7V/cm. The coupling laser detuning is calibrated using the "frequency ruler", described in the next section. The asymmetric broadening of the lineshapes is attributed to inhomogeneities in the DC reference field, particularly near the edges of the field plates.

4.1.3 Plate separation measurement

The separation d between the two field plates within the detection cell is needed to determine the reference field in the cell from the known applied voltage. For our cell, d is roughly measured to be ≈ 0.5cm using a standard ruler, but a more precise value is needed. Since the metal plates within the cell are not accessible for direct caliper measurement, we use the calculated polarizability of the 32s Rydberg state with Eq. 1.3 and Fig. 1.2 to determine d from the measured DC stark shift and applied DC voltage.

To get an accurate value for the DC Stark shift Δ from the spectrum, the rate and range of the coupling laser frequency scan is needed. By observing the Fabry-Perot Interferometer (FPI) signal shown in Fig. 2.14 as the laser frequency is scanned, and comparing the change in location of the FPI transmission signal with its free spectral range, we obtain a rough estimate of how the TA/SHG-pro ECDL frequency changes. However, this is not sufficiently accurate for the required Stark shift measurement.

Instead, we use the sidebands produced by known RF signal fields as a "frequency ruler" to determine the frequency change of the coupling laser as a function of $Time$ during a frequency scan.

A typical $Time$ to frequency calibration scan is shown in Fig. 4.3. Here the scanning $Time$ for different sidebands on the EIT spectrum (with a known DC reference) is plotted vs RF field frequency. The Rubidium atoms are excited to 32s state and a 6.5V DC voltage is applied to the metal plates. The sweep $Time$ vs the RF frequency can be well-fit to a linear equation that can be utilized as the "frequency ruler" to accurately determine the shift, Δ of the primary Stark peak.

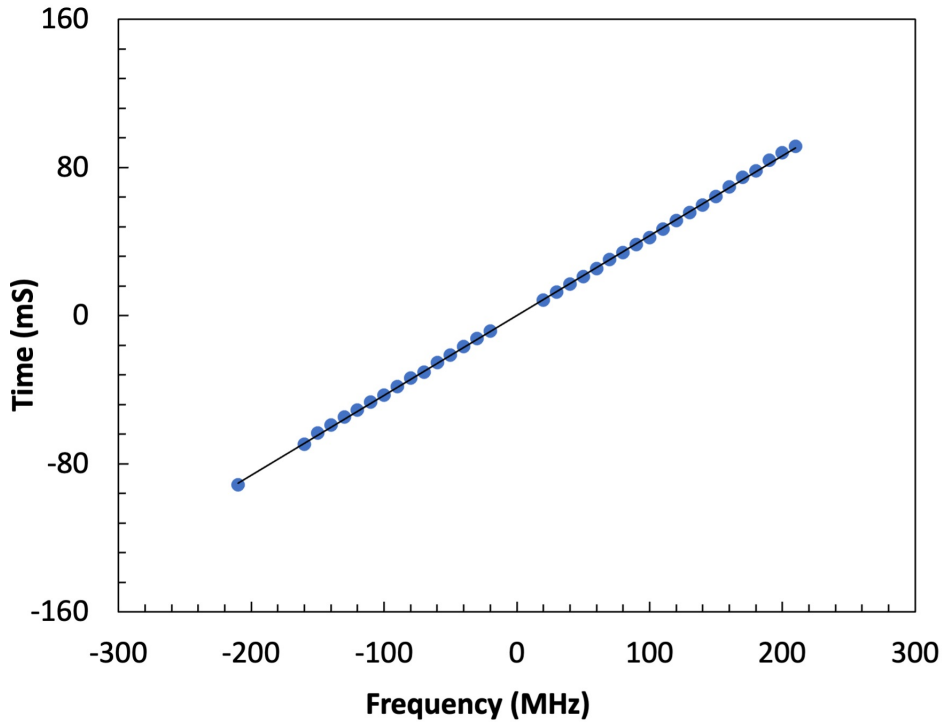

Figure 4.3: Sweep time vs RF sideband frequency. The solid curve is a linear fit to the data points. No sideband measurements near 0MHz and 200MHz are included, due overlap of the sidebands with the zero field and primary Stark shift peak.

The time interval between appearance of the primary Stark shifted peak and the zero field peak during a frequency scan can be directly converted to a frequency interval to obtain Δ using this "frequency ruler". Then, using the equation $F_{dc} = \sqrt{\frac{2|\Delta|}{\alpha}}$, we can extract F_{dc} from the measured Stark shift and combine it with the measured value of the voltage V_{dc} applied across the plates to obtain the plate distance, d.

As noted previously, the polarizability of the Rydberg state α, introduced in the Chapter 1.2.1, has a slight field dependence. So to get the most accurate value of F_{dc}, the value of α must be adjusted according to the measured Stark shift Δ. From the calculated shift data in the Stark map, we can derive the polarizability from the

Eq.1.3 and take the derivative of the field,

$$\alpha = \frac{1}{F}\frac{d\Delta(F)}{dF} \tag{4.1}$$

Therefore, the polarizability α can be plotted as a function of the field or the shift (Fig. 4.4). By fitting α vs Δ to a polynomial, we obtain a more accurate polarizability α for a given Stark shift.

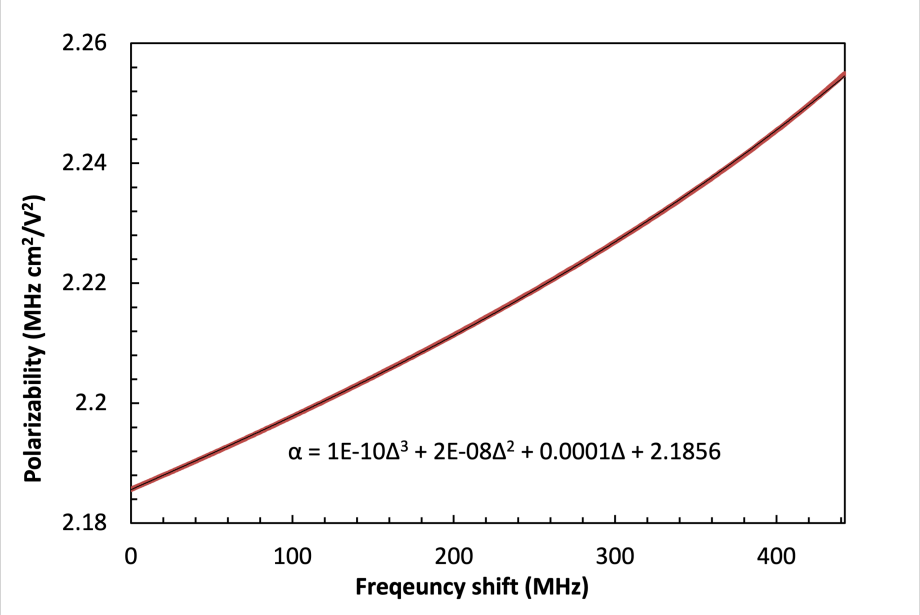

Figure 4.4: The Rb 32s state polarizability α vs the Stark shift Δ. The polarizability is calculated from Eq. 4.1. The frequency shift is the same as the stark map plot in Fig. 3.1. The expression in the graph is a polynomial fit.

The plate separation d is determined from measurements of the Stark shift vs applied voltage for different Rydberg states. Specifically, $1/d$ is the slope of the best linear fit to the measured Stark shift vs applied field (Fig. 4.5). The 32s fitting result gives $d = 0.514 \pm 0.010$cm, and the 25s fitting result gives $d = 0.514 \pm 0.007$cm. Accordingly,for the remainder of the dissertation chapters, we choose 0.51 ± 0.01cm as the plate separation for all field calculations.

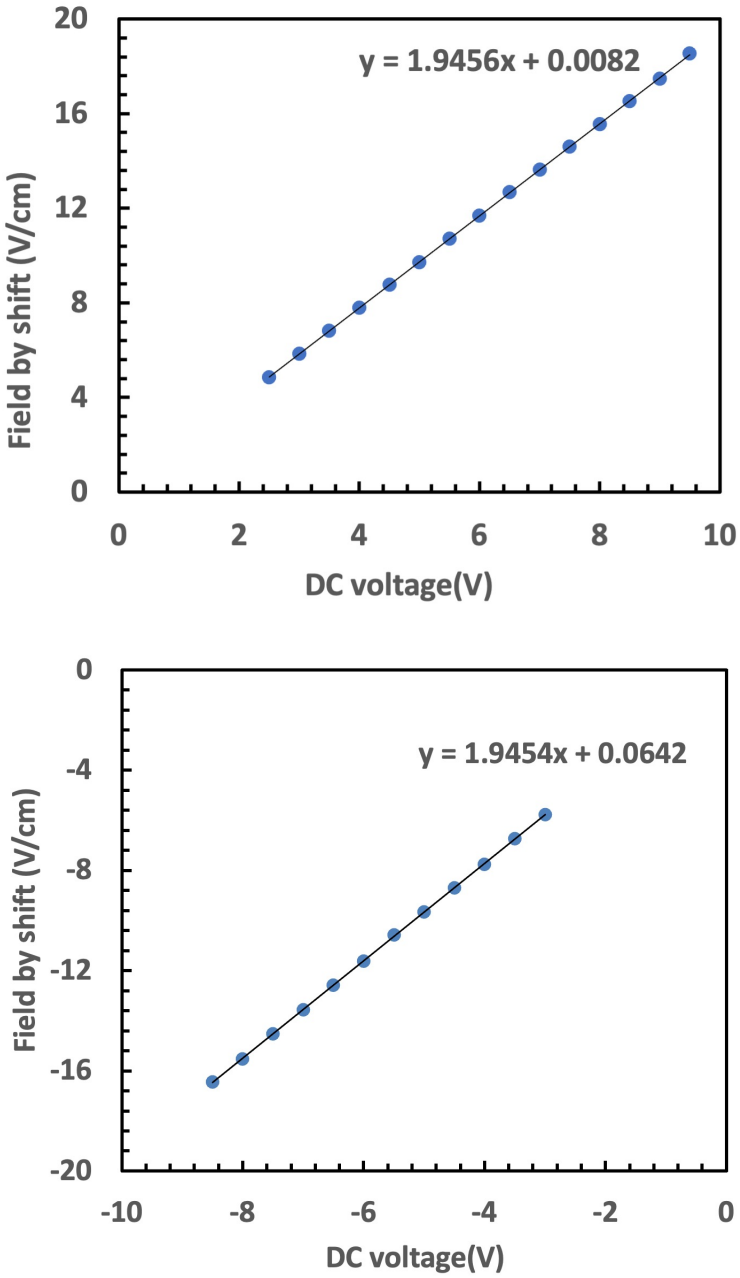

Figure 4.5: Plate distance measurement by plotting the stark shift vs the DC voltage across the metal plates using ^{85}Rb 32s state. (top) Plate distance with positive voltage and (bottom) Plate distance with negative voltage. Both figures show a great linearity between the F_{dc} and V_{dc}. The slope of the data fit gives the inverse of the plate separation d. The uncertainty in the field and voltage measurements are smaller than the plotted symbol size.

4.1.4 Field measurements for different RF frequencies

As the theory chapter shows, from Eq. 3.23, the magnitude of a weak RF field can be derived from the measured ratio η of the average first order sideband amplitude to the main Stark peak amplitude as

$$F_{rf} = \frac{\omega}{\alpha F_{dc}}\beta = \frac{2\omega}{\alpha F_{dc}}\sqrt{\frac{A_\omega}{A_0}} = \frac{2\omega}{\alpha F_{dc}}\eta \tag{4.2}$$

To test the Rydberg electrometer, we compare the values of F_{rf} extracted from EIT measurements and Eq. 4.2 with those obtained from direct measurements of the RF voltage applied to the plates, over a range of RF powers and for different RF frequencies.

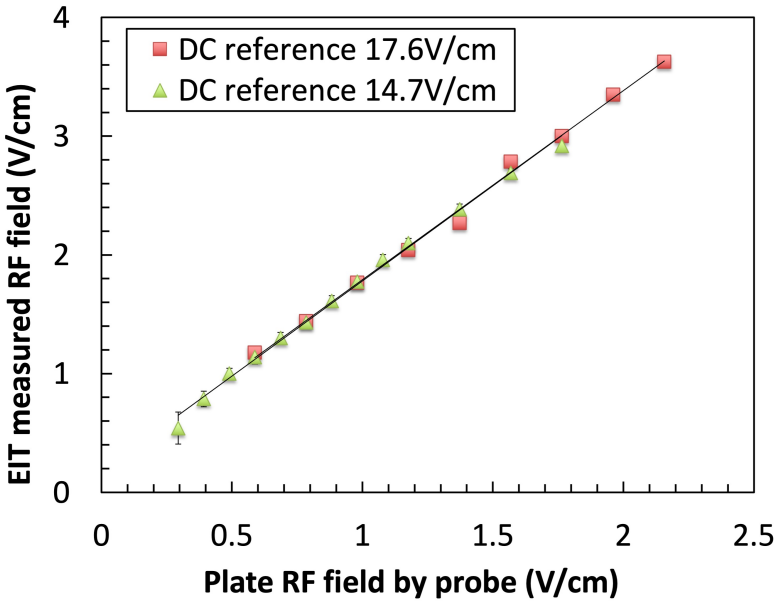

Figure 4.6: 60MHz RF field measurement for two different DC reference fields. The probe laser power is around 1μW and the coupling laser power (P_c) is 50mW. The 32s state of Rb is used for this measurement. The peak amplitude of the main peak and sidebands are taken from the average of 250 EIT spectrum traces. The uncertainty of some measured Fields is smaller than the plotted dot size.

The direct measurements are made using a high impedance RF probe which has a linear voltage response but a significant frequency dependence that is sensitive to the probe connections and cable geometry. Therefore, we expect (and find) a linear relationship between the EIT field vs probe voltage measurements with a constant of proportionality that various (significantly) with RF frequency.

Fig. 4.6 shows the linearity between the EIT measured RF field and the RF voltage on the metal plates measured directly by the high impedance probe for different DC reference fields. As discussed previously, and illustrated in Fig. 3.1, although larger static reference fields provide greater RF field sensitivity, there is an upper limit for the useful reference field amplitude if we are to avoid undesirable mixing between the state of interest and other states in the Stark manifold. For 32s state of ^{85}Rb atoms, the maximum field (DC + RF) is under 24V/cm. The maximum field for 25s is 100V/cm respectively.

Fig. 4.7 shows the expected linearity between the EIT measured RF field vs and the direct probe measurement of the RF voltage for different RF frequencies. The different constants of proportionality between the field and voltage measurements are due to the different response of the electronic probe to the different frequency fields. Whereas traditional RF electronic probes require frequency-dependent calibration, the atomic RF electrometer gives the field at the location of the detection atoms, self-calibrated to the reference field, independent of the RF frequency. In principle, the EIT measured RF field can be used to calibrate the electronic probe (for a fixed given probe connections and cable geometries).

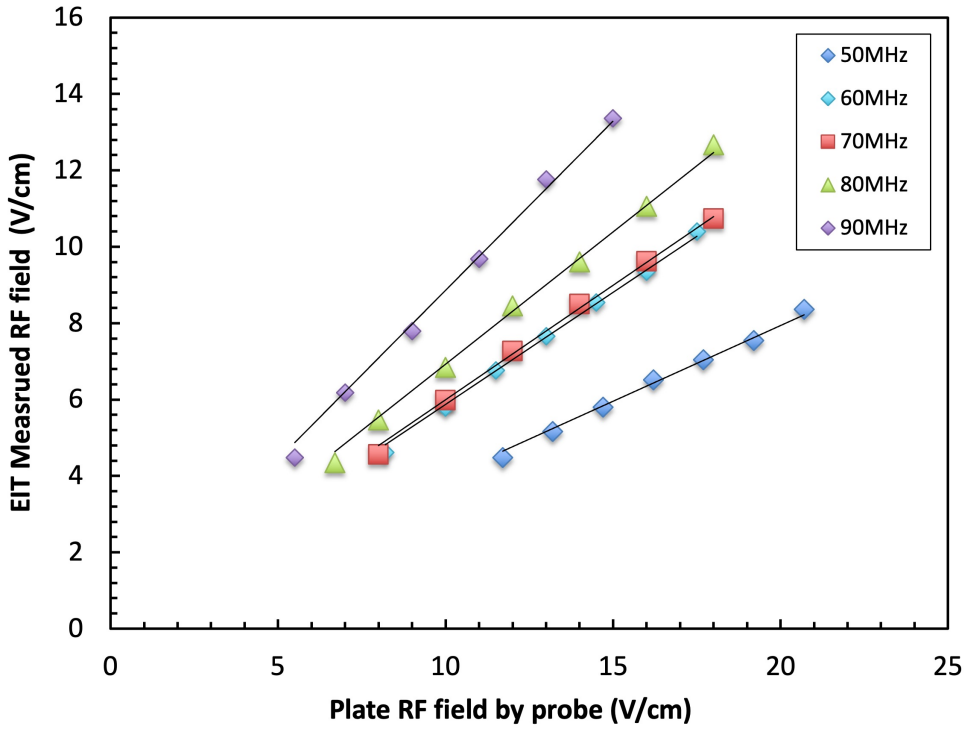

Figure 4.7: 50MHz to 90MHz RF field measurement with a DC reference of $14.7V/cm$. The probe laser power is $\sim 1\mu$W and the continuous-wave coupling laser power (P_c) is 50mW. The coupling laser is set to excite atoms to the Rb 25s state for larger RF field detectable range.

4.1.5 Laser power dependence

The non-resonant Rydberg RF field measurement scheme implicitly assumes that the EIT peak amplitudes are independent of the probe laser intensity and linearly proportional to the coupling laser intensity. However, Fig. 1.11 shows that the latter condition is expected to hold true only at sufficiently low coupling laser power (P_c). For weak RF fields, the Rabi frequencies of the Rydberg sidebands are substantially smaller than that of the main Stark peak. As a result, the greater saturation of the Stark peak amplitude with increasing coupling Rabi frequency (Fig. 1.11) will

result in an overestimate of the RF field (see Eq. 4.2). Therefore, it is necessary to determine, experimentally, the range of P_c for which the EIT response is linear. Operationally, larger P_c values (within the linear response regime) are preferred as they result in larger EIT signals and improved signal to noise for better RF field sensitivity.

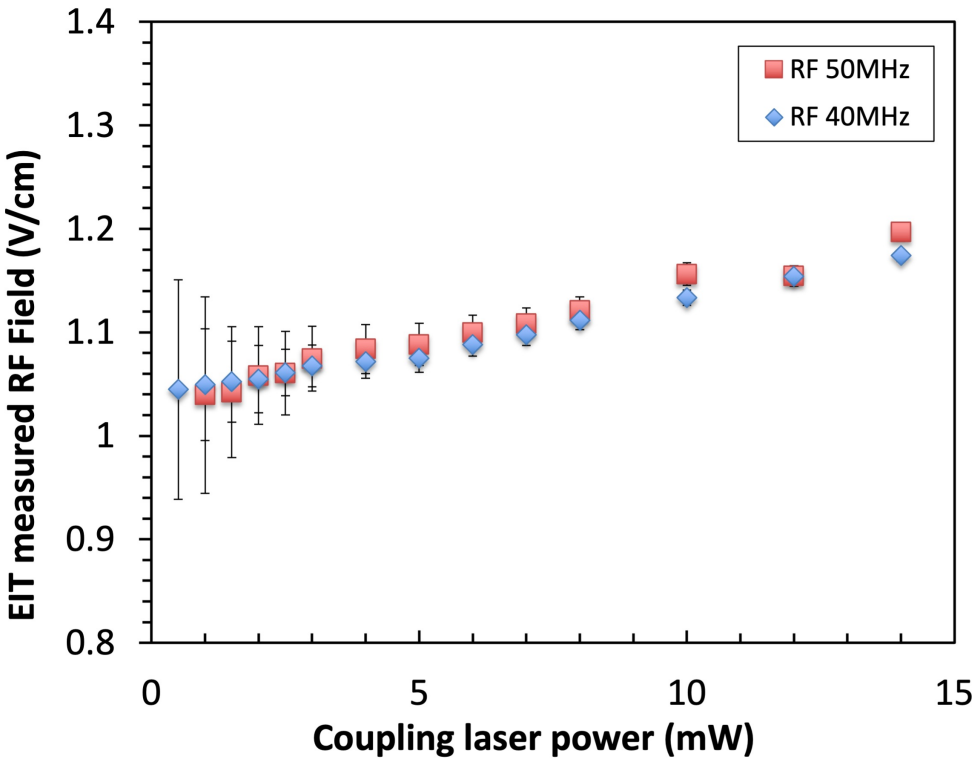

Figure 4.8: 40MHz and 50MHz RF field measurement vs P_c in the lower power regime. The RF field amplitude from the supply is set to the same value for each frequency measurement. The probe laser power is held constant at $\sim 1\mu$W.

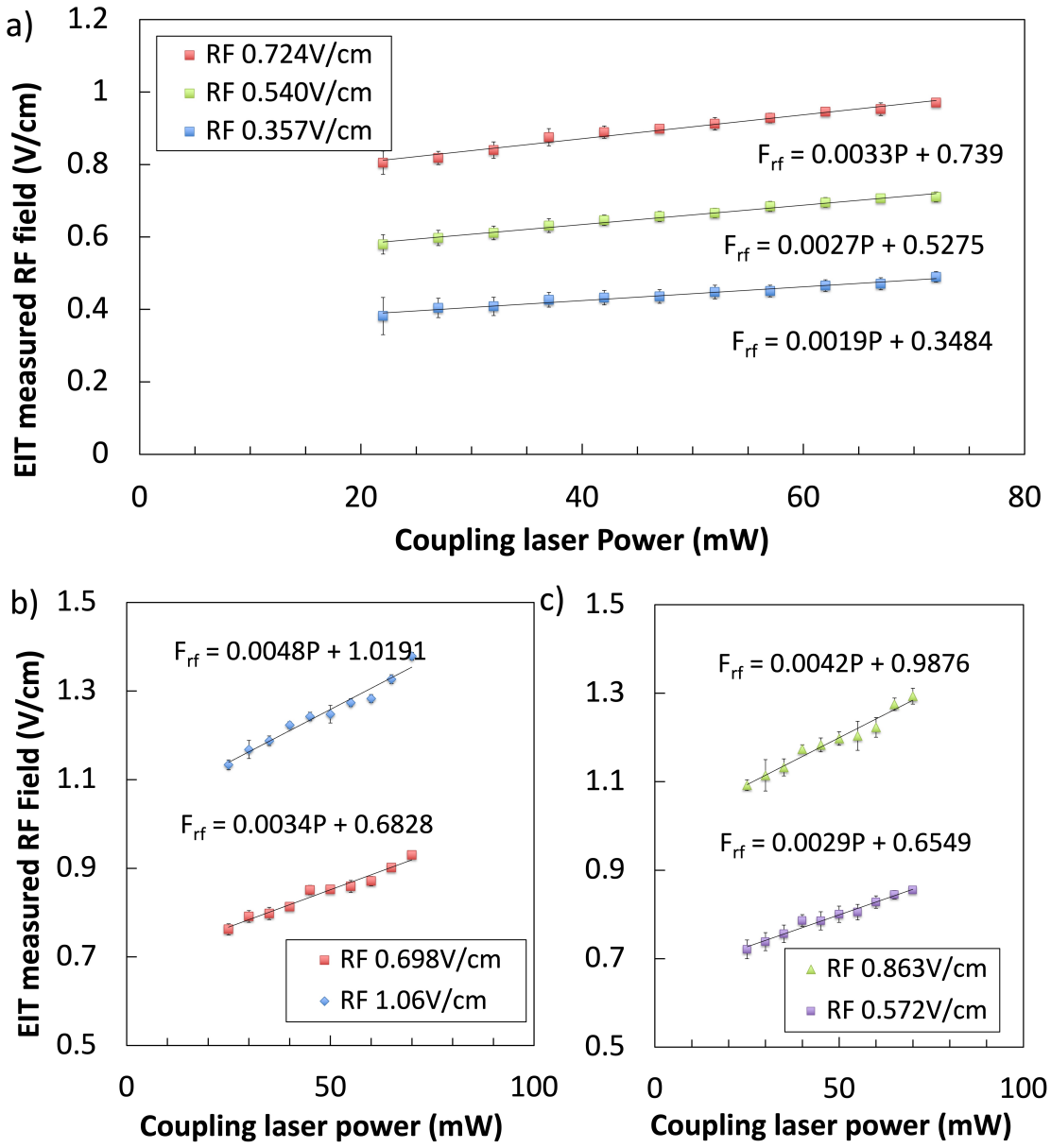

Figure 4.9: Measurements of 50, 60 and 70 MHz RF fields vs P_c are shown in figures a, b and c, respectively. The RF amplitude from the supply is set to the same value for each frequency measurement. Numbers shown in the legend are the RF fields measured by the high impedance probe for each data set. Solid lines are fits to the data. The probe laser power is held constant at $\sim 1\mu$W.

Figs. 4.8 and 4.9 show the growth in the extracted values for F_{rf} with increasing coupling laser power. Fig. 4.10 shows that, as predicted, the probe laser power has a negligible effect on the recovered field value. Figs. 4.8-4.10 all show that, as predicted, the EIT-based RF field determination increases with increasing P_c. Surprisingly, however, there is no apparent range of powers for which the field determination is independent of the P_c. Since the P_c dependence is not necessarily linear (see Fig. 4.10), a field determination by a simple linear extrapolation to P_c=0 is not always a viable option. Therefore, before the non-resonant EIT scheme can be applied to RF field measurement, the P_c dependence must be understood and taken into account during the field measurement, or eliminated. With that goal in mind, the observed power dependence is explored in more detail in the next section.

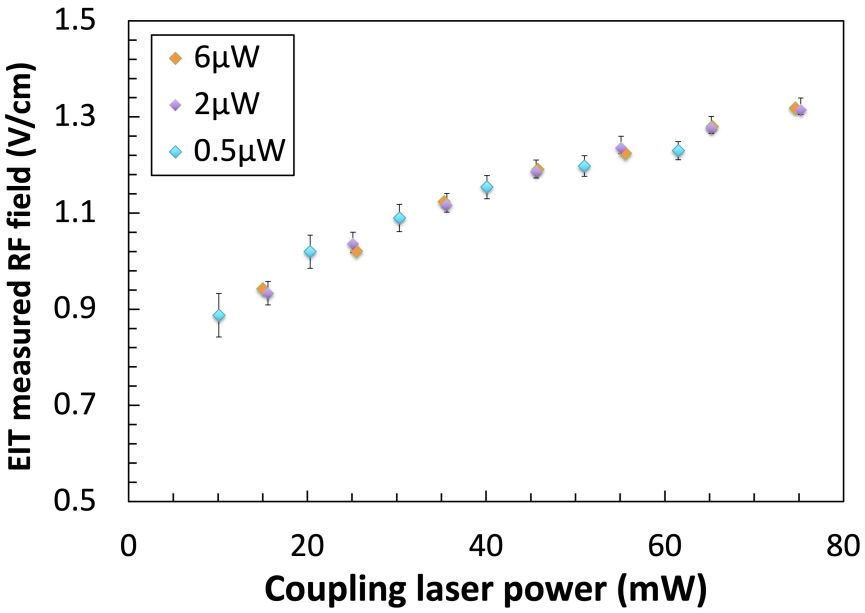

Figure 4.10: 50MHz RF field measurement vs P_c for different probe laser powers (see legend).

4.1.6 EIT peak amplitude and width vs coupling laser power

The predicted dependence of the Rydberg EIT peak amplitude on coupling transition Rabi frequency is examined in section 1.4. Fig. 4.11 compares the measured and predicted amplitudes of the primary Stark peak (in the presence of a weak 50MHz RF field and a DC reference), as a function of P_c under the experimental conditions. The only adjustable parameter in the calculation is an overall amplitude scale factor. The experimental saturation is in reasonable agreement with the simulation.

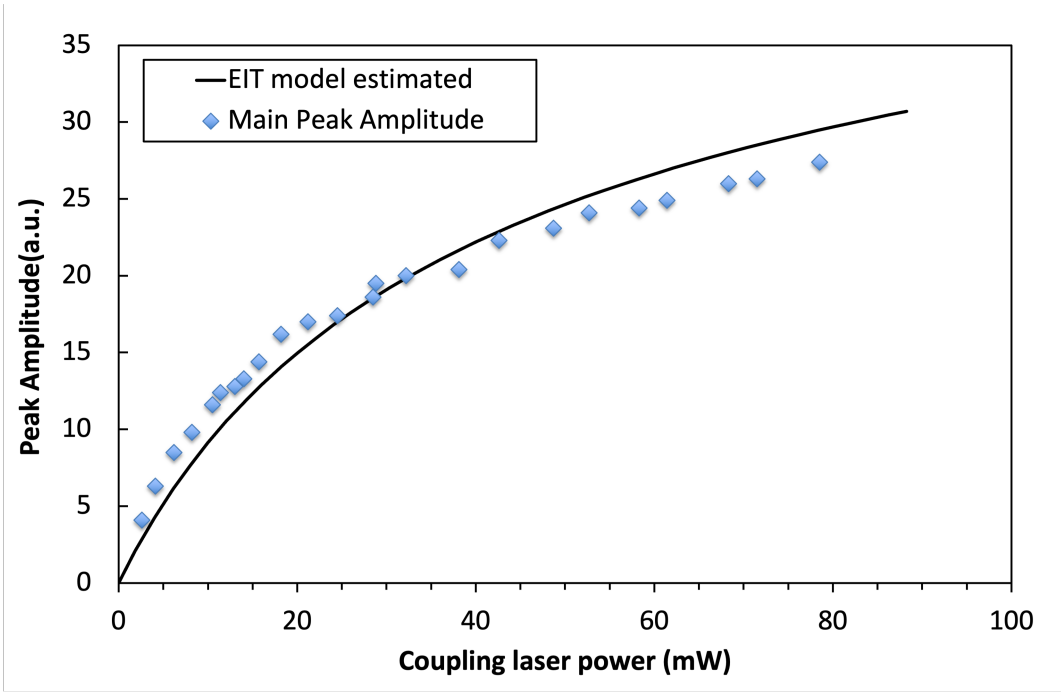

Figure 4.11: Amplitude of the main Stark peak (blue dots-experiment) compared with EIT simulation results (black line). The simulation is performed for the same laser parameters used in the experiments. The only adjustable parameter in the calculation is an overall amplitude scale factor. The measurements are performed in the presence of a weak (0.357V/cm) RF field and a 14.7V/cm DC reference. The uncertainty of the measurement is smaller than the size of dots.

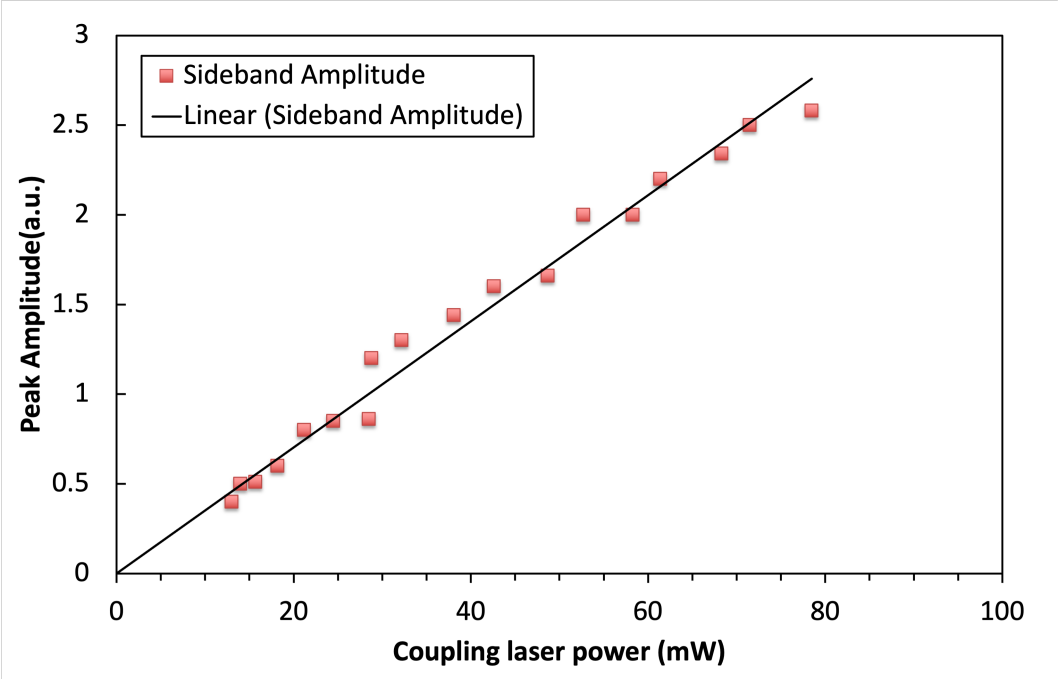

Figure 4.12: Measured average sideband amplitude (red squares) as a function of P_c in the presence of a 50MHz, 0.357V/cm RF field and a 14.7V/cm DC reference. The solid line plotted with the data is the result of a linear fit. The data were taken from the same EIT spectra used to produce Fig. 4.11. The uncertainty of the measurement is smaller than the plotted symbol size.

Although the peak amplitude of the primary Stark peak shows a clear saturation with increasing P_c, the amplitudes of the sidebands do not (see Fig. 4.12). This is because the sideband transitions have a significantly lower Rabi frequency (by a factor of $\frac{\mathbb{J}_1(\beta)}{\mathbb{J}_0(\beta)}$ for weak RF fields) for a given P_c. The data clearly demonstrate the linear dependence of the EIT peak amplitude for sufficiently low Rabi frequency.

Due to the saturation of A_0, $\eta = \frac{A_\omega}{A_0}$ grows with increasing P_c, leading to the observed increase in extracted value of F_{rf} shown in Figs. 4.8-4.10.

The EIT peaks also broaden with increasing P_c, in agreement with numerical simulations (Fig. 1.12). So, one may wonder the EIT peak areas, rather than their amplitudes, would provide a better measure of the amplitudes of the sideband states

relative to the primary Stark state and, therefore, the magnitude of the RF field. However, the widths of the primary Stark peak and sidebands increase at approximately the same rate, and their ratio remains essentially constant as a function of the Rabi frequency of the Rydberg transition. As shown in Fig. 4.13, typically, the main Stark peak width is slightly wider (average around 5%) than the sidebands. Accordingly, the same results are obtained regardless of whether one uses the peak amplitudes or areas to extract the RF field.

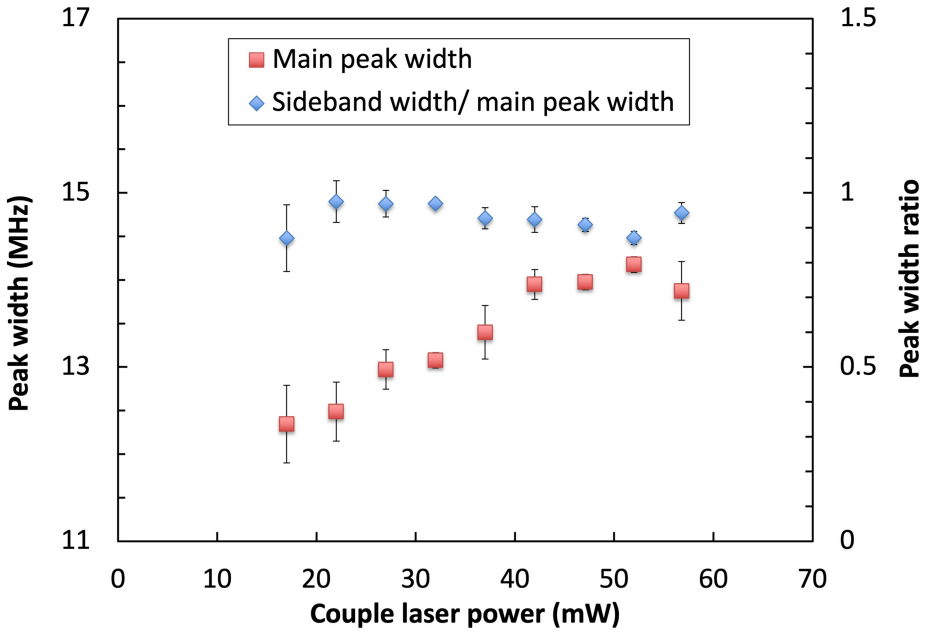

Figure 4.13: Comparison of the widths of the main Stark peak and lowest order sidebands in EIT spectra, in the presence of a 50MHz RF field and a DC reference, as a function of P_c. The RF amplitude is the same for each measurement. The probe laser power is $\sim 0.5\mu$W. The main Stark peak and sidebands broaden at roughly the same rate with increasing P_c.

4.1.7 Extrapolation to zero coupling laser power

As shown in Fig. 4.8, for low P_c, the EIT saturation effect leads to essentially linear growth in the extracted value of F_{rf} with increasing P_c. Given that the EIT satu-

ration is predicted to be negligible at very low P_c, one might expect that a linear extrapolation of F_{rf} to $P_c = 0$ would provide the most accurate value for the RF field.

To test this approach, we apply an RF field that is sufficiently large that its value can be accurately determined from the average Stark shift, Δ, with no DC field present (see Eq. 3.27). We then compare the result from this frequency measurement with the value obtained from amplitude measurements of the 2ω sidebands and main peak (see Eq. 3.29) with no DC field present, as a function of P_c.

As expected, Fig. 4.14 shows that the frequency domain measurement is independent of P_c, while the amplitude measurement varies linearly with P_c. Extrapolating a linear fit to the amplitude data to $P_c = 0$, obtains a value for F_{rf} that is only 3% larger than the value obtained from the frequency measurement, within the uncertainties of the two measurements.

Unfortunately, since the direct Stark shift measurement can only be made for a strong RF field, confirmation of the accuracy of the P_c=0 extrapolation cannot be obtained for weak RF fields (which are our primary interest). Therefore, for smaller RF fields, we need to find an alternative method for confirming the validity of the P_c=0 extrapolation, an approach for identifying an appropriate scaling factor for larger P_c, or a way to eliminate the saturation effect.

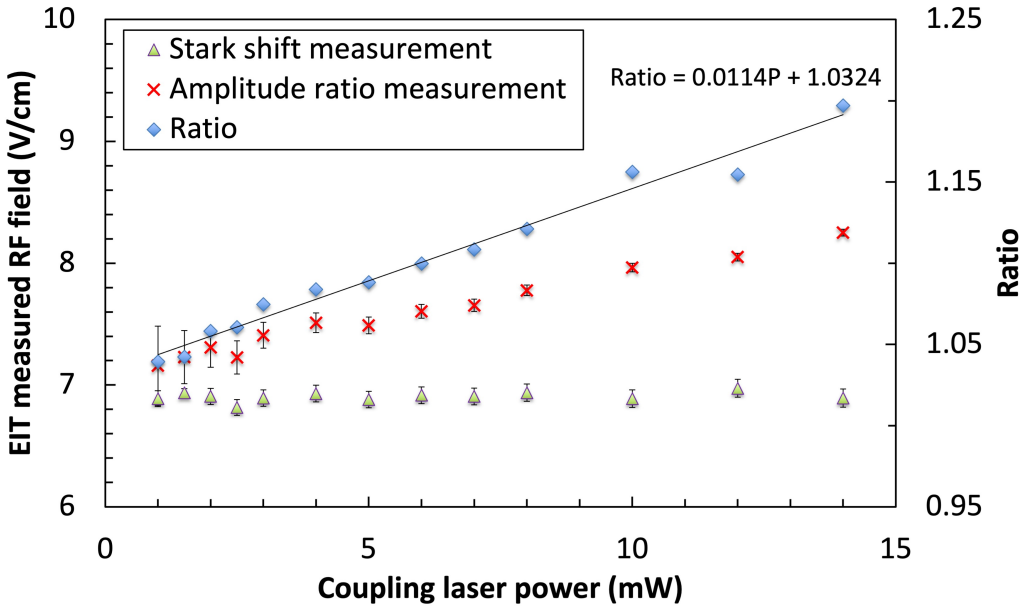

Figure 4.14: Comparison of two approaches for measuring a strong 50MHz RF field vs P_c, in the low power regime. The green diamonds show F_{rf} as determined through direct measurements of the average Stark shift Δ with no reference field present. The red crosses show the value of F_{rf} extracted from the 2ω sideband to main Stark peak amplitude ratio without the presence of a static reference field. The ratio of the two measurements (blue diamonds) is also plotted to illustrate how the difference between the two measurement is reduced as P_c decreases. The y-intercept of the best linear fit to that ratio shows that the P_c=0 extrapolation of the amplitude measurement agrees with the frequency measurement to within measurement error.

In the next section, we describe the results from a pulsed coupling laser scheme. The use of sufficiently short laser pulses at a high repetition rate allows us to eliminate the saturation effect and maintain high signal to noise via lock-in detection. The measurements indicate that reducing the average coupling laser power alone is not sufficient for preventing saturation. Sufficiently short and long pulse "on" and "off" times, respectively, are also required.

4.2 Rydberg electrometry using pulsed EIT

This section focuses on the implementation of the non-resonant Rydberg electrometer using a pulsed EIT readout. As noted in the previous section, use of a pulsed coupling laser (with appropriate timing characteristics) eliminates the coupling laser power dependence of the sideband to main Stark peak amplitude ratio that is used to determine the RF field. In addition, the pulsed scheme naturally lends itself to lock-in detection which allows for improved field sensitivity via increased signal to noise.

After describing the changes in the experimental setup (compared to the cw case), we show how the extracted RF field values depend on the on:off duty cycle and repetition frequency of the coupling laser pulse train. We then present measurements demonstrating the effectiveness of the pulsed Rydberg electrometer for different frequencies and over a wide range of RF field amplitudes, utilizing different approaches for extracting F_{rf} in different amplitude regimes. Next, we demonstrate the measurement of RF fields introduced into the interaction region via free space rather than wire coupling. Those measurements allowed us to resolve an issue related to the coupling between RF and DC power supplies in the wired configuration. Finally, we explore the RF field detection limits of the electrometer for different static reference fields and Rydberg principal quantum number.

4.2.1 Experimental Setup

A schematic of the pulsed coupling laser setup appears in Fig. 4.15. Like the continuous laser setup, the 780nm probe laser is frequency locked using saturated absorption spectroscopy. Unlike the previous setup, the 482nm laser passes through an acousto-

optic modulator (AOM) and then the first order beam diffracted out of of AOM is focused into the Rubidium cell. The EIT spectrum measurement is performed in the Rubidium cell with the metal plate inside.

The AOM is pulsed to serve as a fast switch for the coupling laser. A delay generator sends a periodic square wave which triggers the AOM driver, gating the RF that controls the diffraction from the AOM. As a result, the first order AOM beam, which is angularly displaced from the zeroth order transmission, is pulsed with the same periodicity as the trigger. The intrinsic frequency shift of the diffracted beam is constant as the coupling laser frequency is scanned for the EIT measurements, so the relative positions of the transmission peaks are not affected. The coupling pulse repetition frequency and duration can be varied by changing the corresponding characteristics of the trigger signal from the delay generator.

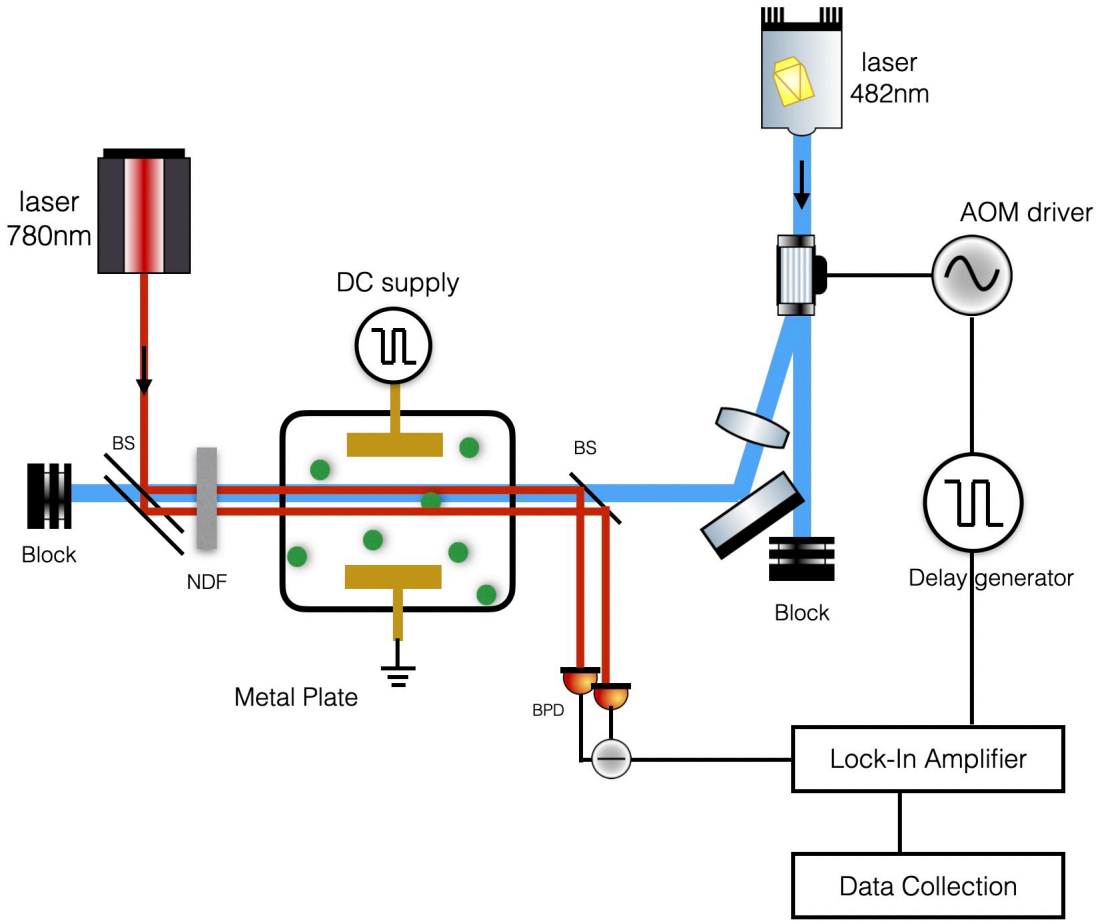

Figure 4.15: Schematic of the experimental setup for a pulsed coupling laser. The probe laser setup remains the same as in the cw configuration. Approximately 2μW of probe light propagates through the cells. The coupling laser first passes through an acousto-optic modulator (AOM). The zero order output beam is dumped into a beam block and the first order diffracted beam is directed into the EIT cell. Given the the AOM efficiency with optimal alignment, up to 50mW of cw laser power can be directed to the cell. The RF drive for the AOM is triggered by a delay generator, which controls how long the AOM driver is on/off during each circle. The lock-in amplifier receives the differential probe transmission signal from the balanced photodiode detector, along with the time reference signal from delay generator. The gain and reference phase for the lock-in are optimized for pulse repetition frequency and duty cycle. The EIT spectrum is obtained from the output of the lock-in, which is recorded as the coupling laser frequency is scanned.

4.2.2 Effect of repetition frequency and coupling pulse duration on RF field measurements

The duty cycle is defined as the ratio of the pulse duration T_{on} to the period of the trigger waveform T_{period}.

$$Duty\,cycle = \frac{T_{on}}{T_{period}} \times 100\% \tag{4.3}$$

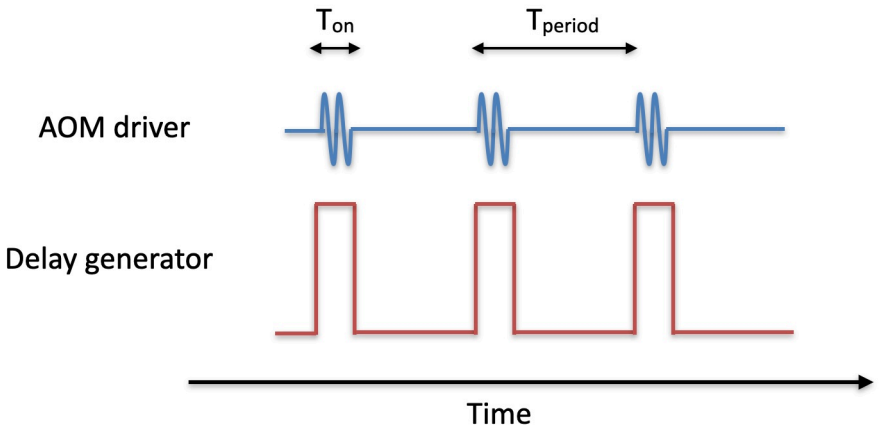

Figure 4.16: Schematic of the pulsed coupling laser timing with delay generator and AOM driver. The delay generator signal can be operated at a repetition frequency $f_r = 1/T_{period}$ from sub-Hz to several MHz. The pulse duration T_{on} can be varied from $\sim$ 100 ns to infinity, allowing for any experimental duty cycle between 0 and 1. The AOM driver is triggered by the TTL voltage from the delay generator, pulsing the 60MHz RF drive, and to modulating the coupling laser synchronous with the trigger.

Given the goal of eliminating the EIT signal saturation that is caused by the strong coupling laser, it is expected that T_{on} may need to be significantly less than T_{period}, resulting in a small experimental duty cycle.

The frequency of the modulation $f_r = 1/T_{period}$ can be choose from 0 Hz to several MHz. As described in more detail below, we find that both that both the "on" and

"off" time intervals are important for eliminating the signal saturation.

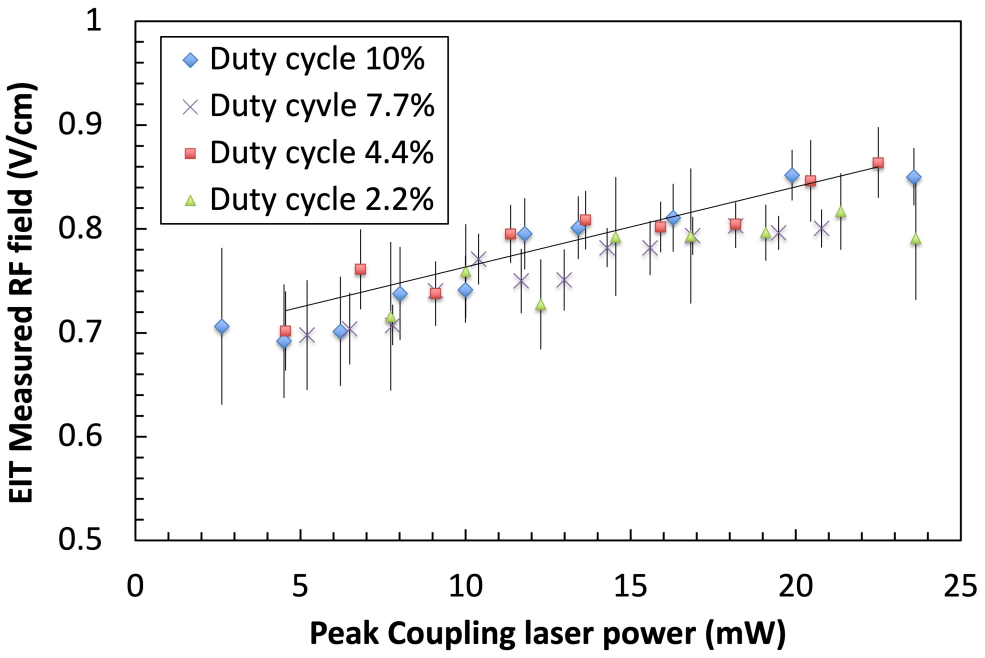

Figure 4.17: 50MHz RF field measurement vs peak coupling laser power, P_c, for a pulse repetition frequency f_r=1kHz. Data are shown for four different pulse durations, with measurement duty cycles of 10%, 7.7% 4.4% and 2.2%. Despite the substantially reduced average coupling laser power, all four data sets give similar results as the cw coupling laser case. The recovered RF field values increase with P_c, regardless of how long the coupling laser is on, suggesting that the saturation of the primary Stark depends on the total laser fluence during a time that is shorter than any of the pulses included in this data set.

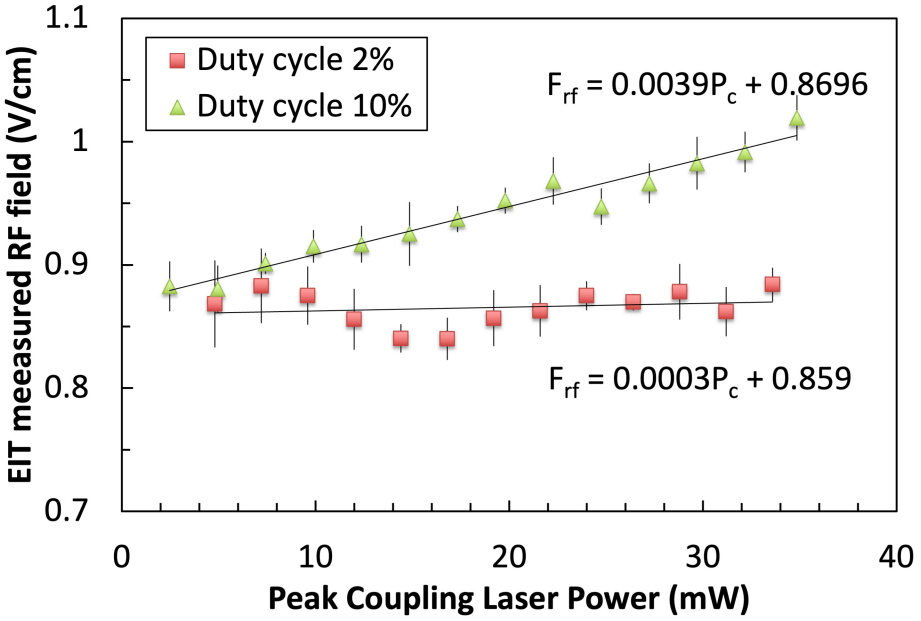

Figure 4.18: 50MHz RF field measurement vs peak coupling laser power, P_c, for a pulse repetition frequency f_r=40kHz. Data are shown for two different pulse durations, with measurement duty cycles of 10% and 2%. The solid curves are best linear fits to the data. The 10% data show extracted RF field values that increase with the P_c, similar to what is observed for the cw measurements and lower pulsed repetition frequencies. The best fit to the 2% data shows no evidence of the systematic increase in the recovered value of F_{rf} with increasing P_c.

We performed measurements of F_{rf} vs P_c with modulation frequencies from 1kHz to 5kHz, and with duty cycles ranging from 1% to 10%. The undesirable variation in the recovered value of F_{rf} with increasing P_c is eliminated for pulse durations of 500 ns (2% duty cycle) and $f_r \leq 40kHz$. The use of the same, or smaller, pulse duration with a lower repetition frequency also gives a result independent of P_c, but has a reduced signal due to the lower duty cycle for the lock-in amplifier, as shown for the data collected at $f_r = 30kHz$ in Fig. 4.20.

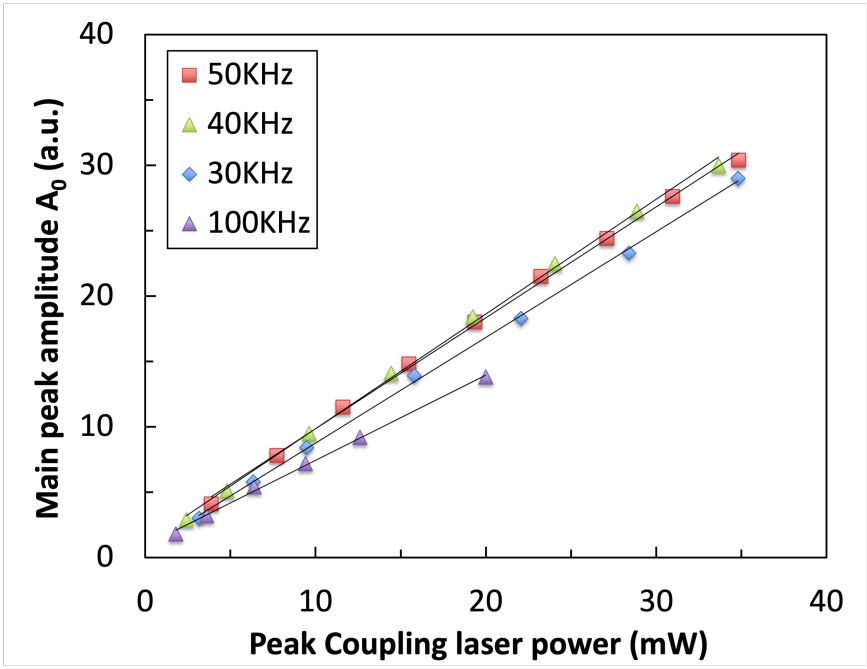

Figure 4.19: Measurement of main Stark peak amplitude using pulsed EIT with fixed pulse duration T_{on} = 500ns and different pulse repetition rates f_r vs peak coupling laser power. The pulsed repetition frequencies for the EIT measurements shown are 30, 40, 50 and 100kHz, corresponding to duty cycles of 1.5%, 2%, 2.5% and 5%, respectively. The 30kHz and 40kHz results behave roughly as expected for an unsaturated signal, with larger 40kHz amplitudes due to the higher duty cycle. The 50kHz amplitudes are essentially the same as those for 40kHz. The absence of an enhancement due to the larger duty cycle suggests some saturation for $f_r >$ 40kHz. Saturation is clear in the 100kHz amplitudes which are considerable smaller than those at lower f_r despite the significantly higher duty-cycle. The uncertainty of the measurements are smaller than the plotted symbol sizes.

For a 500 ns pulse duration, the f_r = 40kHz and 50kHz data in Fig. 4.19 are overlapped within their range of uncertainty. However, in the absence of saturation, the amplitudes at 50kHz should be 10% larger than those at 40kHz, due to the larger duty cycle. Indeed, the 40kHz amplitudes are larger than those at 30kHz, as expected. The amplitudes for f_r = 100kHz are much lower than the other data sets, clearly exhibiting some saturation affect given the expected 2∼3× greater signal enhancement expected for the larger duty cycle.

Apparently, detection using $n = 32$ atoms require a relaxation time of at least 25μs and an excitation time of 500 ns for the amplitude of the main Stark peak to increase in direct proportion to the coupling laser power (as predicted for low Rydberg Rabi frequencies). Notably, the spontaneous lifetime of the Rb 32s state is 28μs[42], and the lifetime at room temperature is 19μs due to black body radiation[43]. Choosing $f_r \leq 40$kHz, gives sufficient time for relaxation of any 32s Rydberg population created during the 500 ns coupling laser pulse. In the end, the optimum pulse characteristics for obtaining the best signal to noise with no observable dependence of F_{rf} on P_c were found to be $f_r = 40$kHz with a 500 ns pulse duration (i.e. a 2% duty cycle) at n = 32. Unless otherwise noted, these pulse parameters were used for all of the pulsed EIT measurements discussed in the remainder of this dissertation. The optimum values of T_{on} and T_{period} are expected to be somewhat smaller(larger) for lower(higher) n due to the $1/n^3$ dependence of both the Rydberg transition probability and spontaneous emission rate [5].

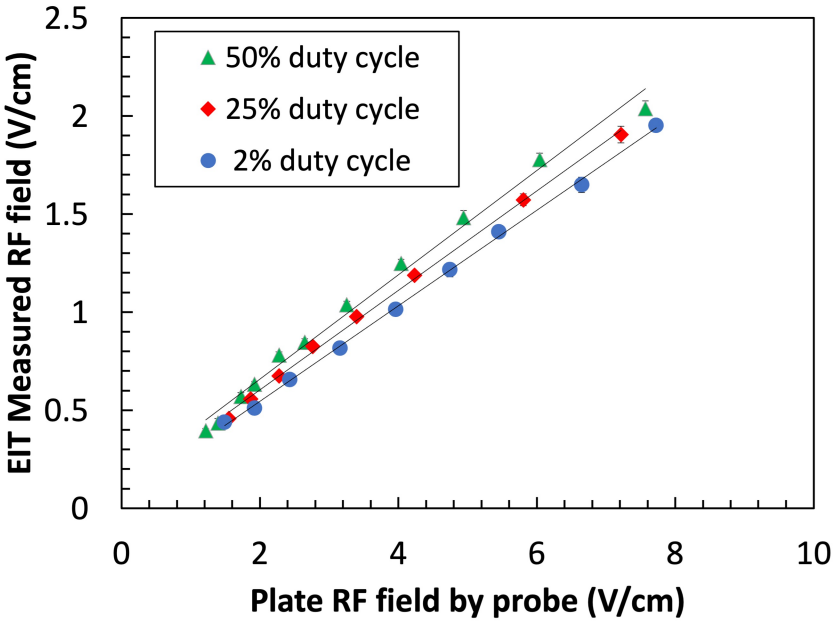

Figure 4.20: Measurement of a 60 MHz RF field using pulsed EIT with 50%, 25% and 2% duty cycles vs direct measurements using a high impedance probe. The pulsed repetition frequency for the EIT measurements is 40kHz. All of the EIT measurements are linearly proportional to the probe measurements. However, due to the non-negligible saturation effects for the higher duty cycle measurements, the constants of proportionality differ for the three EIT data sets. However, using data such as these, EIT measurements made with higher duty cycles can be calibrated to the 2% duty cycle result. This can be advantageous for weak RF fields, due to the increase in signal to noise for higher duty cycle measurements.

For extremely weak RF fields, the measurement signal to noise can be improved by using a higher duty cycle, provided additional calibration experiments have been performed to link the high and low duty cycle results (see Fig. 4.20). Measurements obtained using a cw coupling laser can be recalibrated in an analogous way.

4.2.3 Comparison of non-resonant pulsed EIT-based RF field measurement approaches

Using appropriate pulse parameters for the coupling laser, the Rydberg electrometer can be used to accurately measure RF field amplitudes over 3 decades (or more), employing the different approaches outlined in Chapter 3 for the weak, intermediate, and strong field regimes, Eqs. 3.20, 3.24 and 3.27, respectively (see Fig. 4.21).

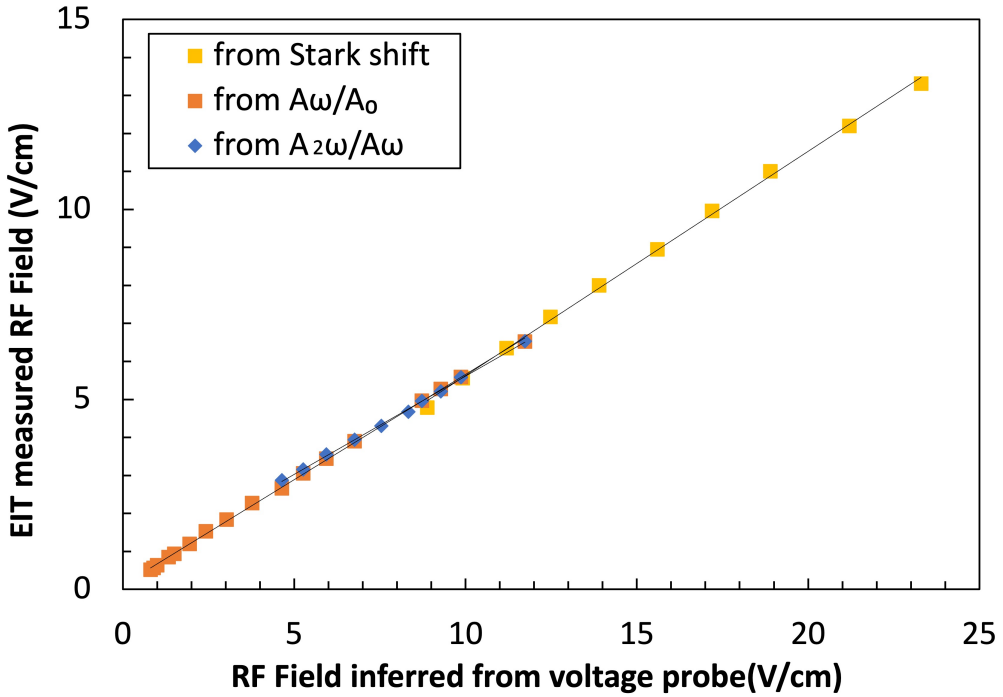

Figure 4.21: Amplitude of a 60MHz RF field measured using the pulsed non-resonant Rydberg electrometer vs direct measurements using a high impedance voltage probe. The orange data points are based on measurements of $\eta = A_\omega/A_0$, using the Bessel function expression in Eq. 3.20, which is accurate for $\beta < 2.40$. The blue data points were obtained from measurements of $\eta_2 = A_{2\omega}/A_\omega$ and the Bessel function expression in Eq. 3.24, which is accurate for $\beta < 3.83$. The yellow data points use the Stark shift formula in Eq. 3.27 to determine the strong RF field directly from the frequency splitting between the primary Stark peak and the zero field peak with no DC reference present. The solid lines are fits to the various data sets. The uncertainty of the measured RF field is smaller than the plotted symbol size. The fitting results are given in the following table.

60MHz RF field measurement	slope	Y-intercept(V/cm)
Between ω sideband to main peak	0.5537	0.1225
Between 2ω sideband to ω sideband	0.5163	0.4481
Stark shift	0.5900	-0.2735
All of three above combined	0.5701	0.0356
Two amplitude ratio measurements combined	0.5501	0.1540

Table 4.1: Fitting results for EIT vs direct probe measurements of 60 MHz RF field.

The three different types of EIT measurements are in good agreement in their region of overlap. However, there are small but significant differences in the linear fits to the individual data sets. Since we expect the probe response to be proportional to the field between the plates (with a constant of proportionality that is independent of the voltage across the plates), the differences in the slopes and, especially, the non-zero y-intercepts of the fits indicate that there are unresolved issues affecting either or both the EIT or probe measurements. As described in detail in a later section, these differences can be attributed to a coupling between the RF and DC supplies that depends on both output level of both supplies. These effects are small and tend to average out in the combined fit to the three data sets as suggested by the very small y-intercept of that fit.

Despite the small effects associated with the coupling between the supplies, the RF field amplitudes determined from the EIT measurements are sufficiently accurate to enable consistency checks of the predicted functional forms of the individual EIT peak amplitudes. Fig. 4.22 shows excellent agreement between the measured and calculated (Eq. 4.3) main Stark peak amplitudes vs RF field amplitude.

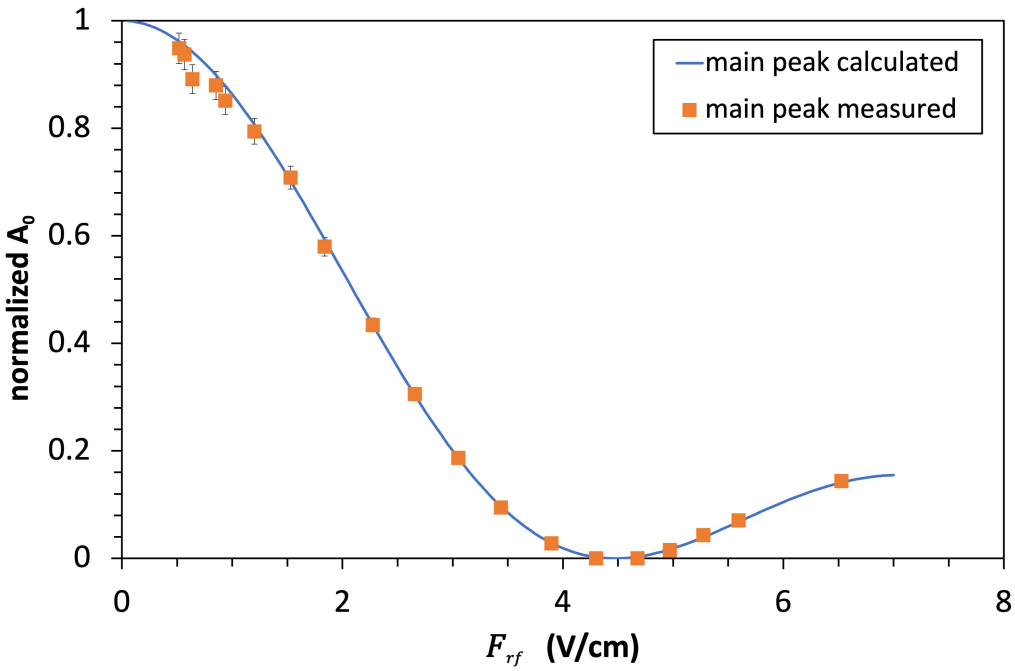

Figure 4.22: Normalized main Stark peak amplitude vs RF field. The blue line shows the calculated peak amplitude from Eq. 4.3 with a maximum sum index, $m_{max} = 100000$. The orange dots are the normalized experimental peak amplitudes vs RF field as determined from the EIT measurements (see Fig. 4.21).

Fig. 4.23 shows an analogous comparison of the measured and calculated amplitudes of the first order sidebands. The agreement is very good.

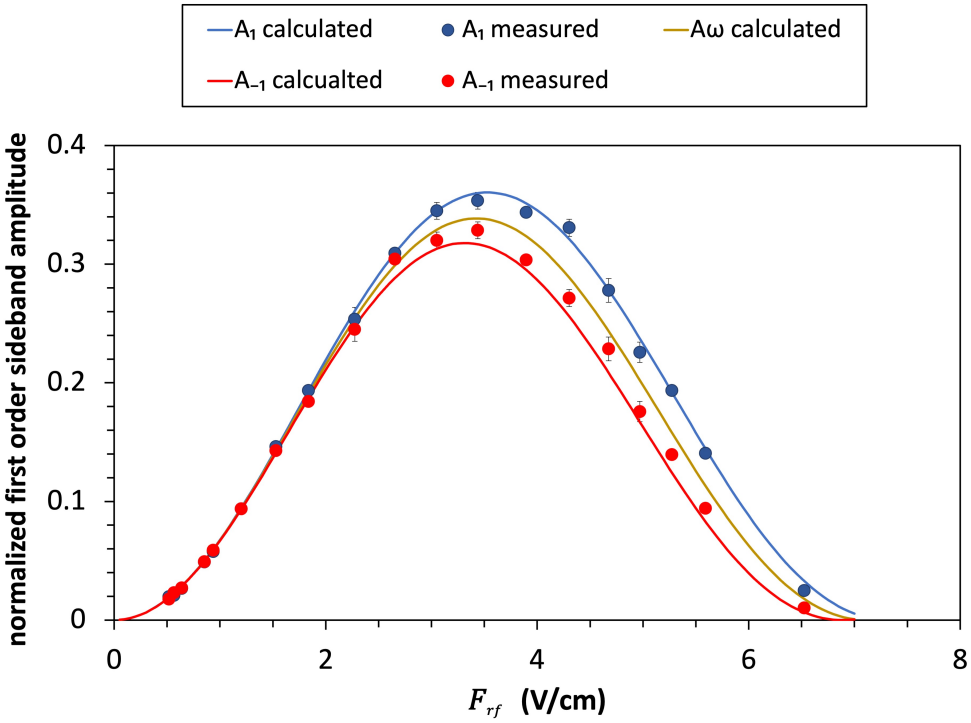

Figure 4.23: Normalized first order sideband amplitudes vs RF field. The blue and orange lines are the calculated ± 1 sideband amplitudes with with a maximum sum index, $m_{max} = 100000$ in Eq. 4.3. The brown line is the calculated average first order sideband A_ω. The blue and orange dots are the normalized experimental peak amplitudes vs RF field as determined from the EIT measurements (see Fig. 4.21).

Fig. 4.24 shows experimental and calculated ratios of the average amplitudes of the 2ω and ω sidebands, $\frac{A_{2\omega}}{A_\omega}$, vs RF field. As a consistency check, for the measurements shown, the RF fields are derived using two different amplitude ratios. For the blue data points, the field is extracted from $\eta_2 = \frac{A_{2\omega}}{A_\omega}$, resulting in perfect agreement between experiment and theory (as required). For the green points, the field is obtained from the $\eta = \frac{A_\omega}{A_0}$, and the agreement with theory is still excellent.

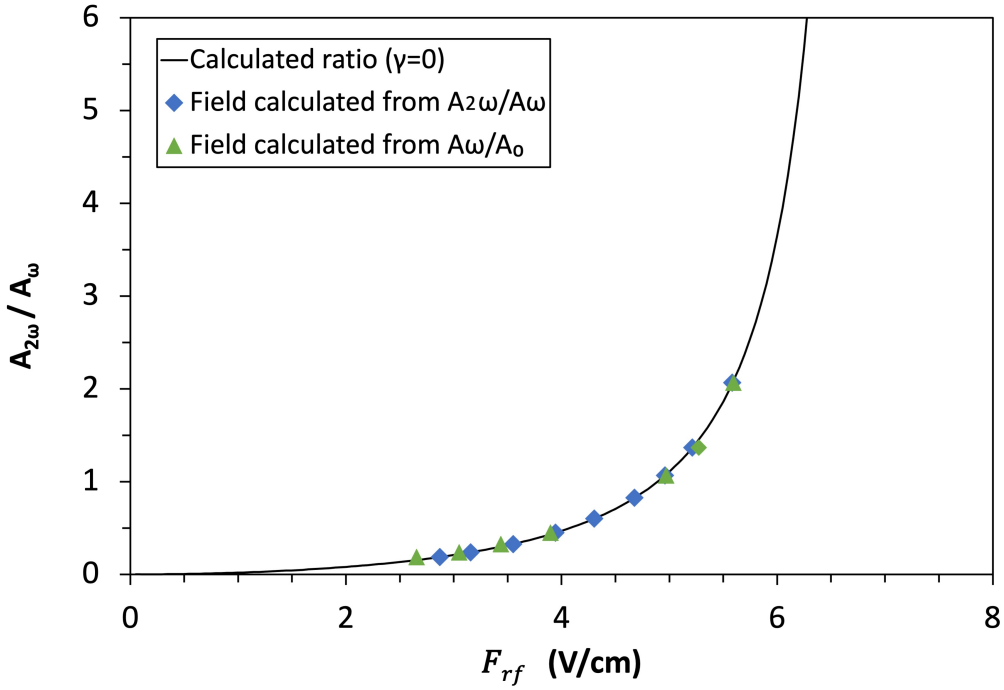

Figure 4.24: Amplitude ratio, $A_{2\omega}/A_{\omega}$ vs RF field. The black line is the calculated amplitude ratio in the $\gamma = 0$ approximation (Eq. 3.24). The blue dots are the measured ratio when the RF field has been determined from the experimental amplitude ratio $\eta_2 = \dfrac{A_{2\omega}}{A_{\omega}}$. The green dots are the measured ratio when the RF field has been determined from the amplitude ratio $\eta = \dfrac{A_{\omega}}{A_0}$.

4.2.4 Pulsed EIT peak widths

As shown in Section 3.2.6, the linewidths of the spectral peaks observed using cw coupling laser are expected to increase with P_c. For the cw case, the ratio of the sideband peak to primary Stark peak width is shown to be ≈1, independent of the Rydberg transition Rabi frequency (Fig. 4.13). The situation is similar for the pulsed laser setup (40kHz modulation rate and 2% duty cycle), as shown in Fig. 4.25, where the peak widths are plotted vs RF field amplitude. The ratio of the width of the peaks varies between 0.955 to 0.98, which results in $\sim$ 2% change in the RF field

determination if the peak area is used instead of peak amplitude. This difference is mainly due to uncertainties in the determination of the peak width for different peak shapes.

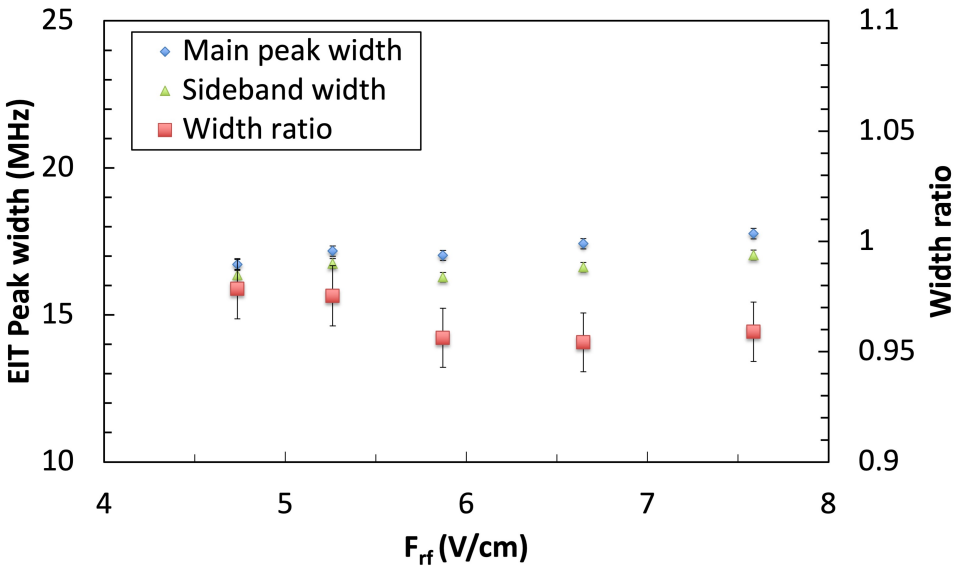

Figure 4.25: Width of the main Stark peak and sidebands vs RF field. The width of both peaks are found to increase slightly with larger RF field. Rubidium 25s state is used here to provided larger measurable RF field range. The DC reference voltage is 29.4V/cm.

The width of the EIT peak becomes slightly wider as the RF field increasing as well shown in the Fig. 4.25. This is likely due to the spatial inhomogeneity of the electric field between the two plates. With larger field (DC+RF), the slope of the s-state energy vs field curve increases, as shown in Fig. 1.2, and the range of electric fields present in the interaction region also increases. Therefore, there are a wider range of energies for the s-state within the laser sampled volume, resulting in a slightly broader main peak and sidebands.

4.2.5 Comparison of non-resonant pulsed EIT-based RF field measurements for other RF frequencies

Sections 4.2.2-4.2.4 describe and present a range of measurements characterizing and demonstrating the effectiveness of the pulsed EIT approach for 60MHz fields. Below, we present analogous measurements for 50, 70, 80, and 90 MHz fields.

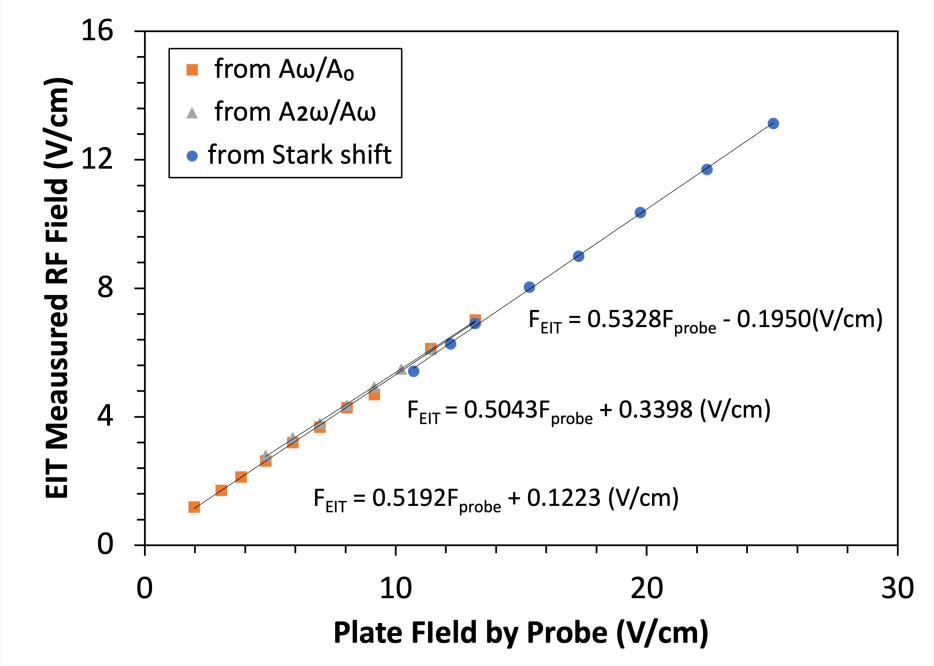

Figure 4.26: Comparison of EIT and high impedance probe measurements of 70MHz RF fields across three amplitude range. The orange squares show data obtained from the ratio A_ω/A_0, which is suitable for weak RF fields. The grey triangles show data obtained using the ratio $A_{2\omega}/A_\omega$, which is valid for low to intermediate fields. The blue circles show fields determined from direct frequency measurements of the Stark shift. The solid lines show linear fits to the three individual data sets. The uncertainty in the measured RF field is smaller than the plotted symbol size.

Tables summarizing the linear fitting results comparing EIT and probe measurements for 50, 70, 80, and 90 MHz RF fields appear below.

The EIT measurements which are based on different approaches in the different am-

50MHz RF field measurement	slope	Y-intercept(V/cm)	fit quality (R^2)
A_ω/A_0	0.8374	-0.0025	0.9990
$A_{2\omega}/A_\omega$	0.8223	0.0627	0.9983
Stark shift	0.8105	-0.1764	0.9997
Combined	0.7857	0.1345	0.9992

Table 4.2: Linear fitting results for EIT vs probe measurements of 50MHz RF fields.

70MHz RF field measurement	slope	y-intercept(V/cm)	fit quality (R^2)
A_ω/A_0	0.5192	0.1223	0.9985
$A_{2\omega}/A_\omega$	0.5043	0.3398	0.9993
Stark shift	0.5328	-0.1950	0.9995
Combined	0.5172	0.1122	0.9993

Table 4.3: Linear fitting results for EIT vs probe measurements of 70MHz RF fields.

80MHz RF field measurement	slope	Y-intercept(V/cm)	fit quality (R^2)
A_ω/A_0	0.4652	0.064	0.9993
$A_{2\omega}/A_\omega$	0.4383	0.4127	0.9992
Stark shift	0.4730	-0.3696	0.9995
Combined	0.4527	0.1173	0.9989

Table 4.4: Linear fitting results for EIT vs probe measurements of 80MHz RF fields.

90MHz RF field measurement	slope	Y-intercept(V/cm)	fit quality (R^2)
A_ω/A_0	0.7330	0.1796	0.9997
$A_{2\omega}/A_\omega$	0.6962	0.6103	0.9996
Stark shift	0.7861	-0.5334	0.9987
Combined	0.7431	0.0794	0.9983

Table 4.5: Linear fitting results for EIT vs probe measurements of 90MHz RF fields.

plitude regimes give reasonably consistent results for each RF frequency. However, there is a substantial variation in the relationship of the EIT measurements to those made by the high-impedance probe. Indeed, the fits indicate that the high impedance probe has a significant non-monotonic frequency response.

While the EIT measurements are in fair agreement with each other for all frequencies,

there is a noticeable difference between the fits involving RF fields extracted from amplitude ratio measurements and those obtained by direct frequency measurements of Stark shifts. Namely, the Stark shift measurements have a non-negligible negative y-intercept. This is is likely due to field inhomogeneity near the edges of the field plates, which leads to asymmetries in the zero field and primary Stark features in the EIT scans, and tends to slightly reduce the separations between their centers.

In contrast, the fits to the amplitude ratio measurements typically have small positive y-intercepts. The cause of the small positive y-intercepts for the amplitude ratio measurements is believed to be the result of the coupling between the RF and DC power supplies, as supported by the discussion and auxiliary measurements described below. For all of the measurements, the outputs of the DC and RF power supplies are connected directly to the field plates. Although a filter capacitor prevents the DC voltage from entering the RF supply, decoupling the DC supply from the RF is more difficult. Notably, for the Stark shift measurements, the static voltage is set to zero.

In an attempt to reduce the coupling between the two supplies, several "noise eater" ferrite beads were clamped around the cable between the metal plates and the DC power supply. With the ferrites in place, the y-intercept of the amplitude ratio fits were noticeably changed while the slope remained the same (within the fit uncertainty).

For example, the y-intercept decreased from 0.1729V/cm to 0.1223V/cm for the 70MHz measurement and from 0.1530V/cm to 0.064V/cm for 80MHz. In addition, the tables show that the offsets terms in the fits are larger for the data sets taken at larger RF fields. This suggests that as the RF field is increased, it has a non-negligible influence on the DC supply, slightly reducing the output voltage. Indeed direct measurements of the static voltage on the plates indicated that the DC voltage

varies with the RF field. An accurate determination of the actual static voltage on the plates will be discussed in the next section 4.3.

4.2.6 RF field measurement with free-space coupling

Of course, it is anticipated that a primary application of non-resonant Rydberg field detection is the characterization of freely propagating fields, not just those generated by direct connection of a voltage source to a conductor array.

Accordingly, we have also tested the Rydberg electrometer using a simple antenna as the source of the field in the Rb cell. The experimental setup is not changed except that the RF field wires are disconnected and moved a short distance away from the wires connecting to the plates within the cell. Because the wavelength of the 50-100 MHz RF radiation is much larger than the size of the metal plates and the separation between them, the RF voltage across the plates (as measured by the high-impedance probe) is still directly proportional to the field, providing a useful comparison for the EIT measurements. Moreover, without the direct connection between the RF and DC power supplies, the effect of the RF on the static reference voltage is substantially reduced.

Fig. 4.27 shows a comparison of EIT and high impedance probe measurements of 80MHz RF fields introduced into the detection cell via free space coupling from a simple antenna. Results are presented for different pulsed coupling laser duty cycles. For measurement of very weak fields, the sensitivity can be enhanced using a higher pulsed laser duty cycle that has a correspondingly higher signal to noise. More measurements such as those shown in Fig. 4.27 allow for re-calibration of the results obtained at higher duty cycle.

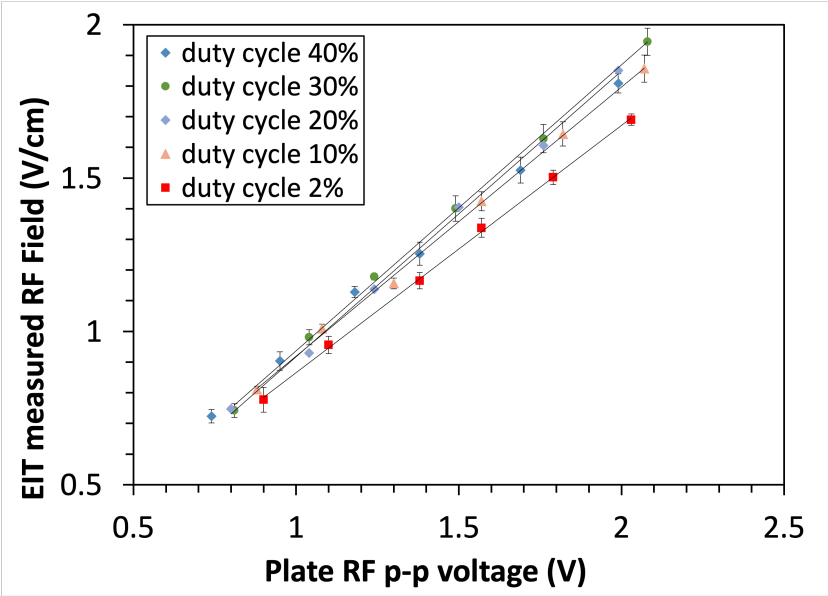

Figure 4.27: EIT field measurements vs high impedance probe measurements of the peak to peak RF voltage on the field plates. The 80MHz field is introduced into the Rb cell via free space coupling from a simple antenna. Results are presented for different pulsed coupling laser duty cycles. The RF field is determined from measurements of η. The solid curves are linear fits to the respective measurements.

The table below gives the results of the fits to the individual data sets shown in Fig. 4.27. Notably, the y-intercepts from the fits are much smaller than those when the RF supply is connected directly to the field plates, presumably due to the reduced coupling between the RF and DC supplies. The statistical P-value can be used to determine the significance of the offset term in the fits. $P < 0.05$ indicates that the inclusion of the offset is statistically significant[44]. Significance of the y-intercept can also be inferred by comparing the magnitude of the offset to its uncertainty.

Fig. 4.28 shows a comparison of the slopes of linear fits to the data in Fig. 4.27, with and without the constant term. In all cases, the slope values are overlapped within their range of uncertainty.

Measurement duty cycle	Slope	Y-intercept(V/cm)	p-Value
2%	0.806±0.029	0.060±0.046	0.019
10%	0.877±0.046	0.041±0.050	0.175
20%	0.933±0.060	-0.016±0.085	0.642
30%	0.933±0.042	0.036±0.060	0.878
40%	0.856±0.051	0.091±0.075	0.022

Table 4.6: Fitting results for comparison of free-spaced coupled 80MHz EIT RF field measurements to probe measurements of peak to peak voltage on the field plates, as a function of pulse duty cycle.

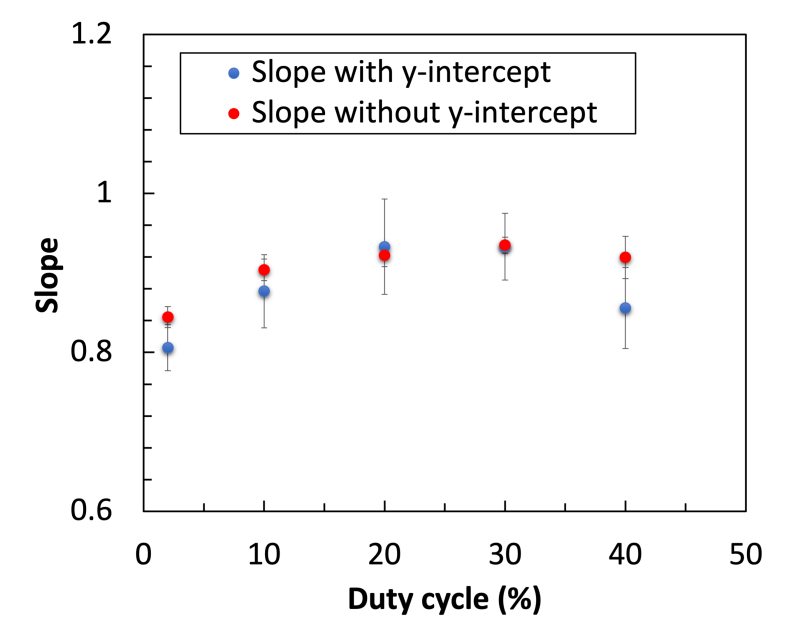

Figure 4.28: Comparison of the slopes of linear fits to the data in Fig. 4.27, with and without the constant term. In all cases, the slope values are overlapped within their range of uncertainty. Inspection of the P-values in Table 4.6 confirms that larger P-values correspond to better agreement between the slopes in the two fits.

A small residual coupling of the RF voltage into the DC supply is likely responsible for any small but statistically significant offsets in the proportionality between the probe voltage measurements and the EIT field determinations.

4.2.7 Smallest measurable RF field

Ultimately, the sensitivity of the non-resonant Rydberg RF field measurements are determined by the probe laser intensity stability, the dynamic range of the lock-in amplifier, and lock-in amplifier noise. The dynamic range limitation can be circumvented to a large degree by measuring the sideband and primary Stark peak amplitudes on consecutive laser scans using different amplifier input sensitivity settings. The latter currently determines the smallest fields that can be measured with our current apparatus, dominated by noise from the 40kHz reference in the output. While it should be possible to improve the sensitivity by several orders of magnitude with a better lock-in or additional filtering, it is useful to determine the smallest RF field that can be measured with reasonable accuracy with the current apparatus.

For small fields, we can directly relate the RF field to known and/or measured parameters,

$$F_{rf} = \frac{2\omega}{\alpha F_{dc}} \sqrt{\frac{A_\omega}{A_0}} \tag{4.4}$$

where the polarizability α depends on which Rydberg state we use for detection, F_{dc} is the strong DC reference which is restricted to the range of fields for which the detection state has not merged with the remainder of the Stark manifold, and $\eta = \frac{A_\omega}{A_0}$ is the measured amplitude ratio. As noted above, the smallest measurable value of η depends on the experimental background noise.

To reduce the background noise, the peak amplitude is taken from the average of 512 traces, requiring a total measurement time of ~ 60 sec. We estimate that the smallest usable sideband amplitude must be larger than the background noise. For example, for background noise of $\pm$ 1mV, the smallest detectable sideband has an amplitude of 1mV. As noted above, to increase the dynamic range of the measurement, the main

peak amplitude can be measured using a different amplification gain setting on the lock-in amplifier by changing the input sensitivity.

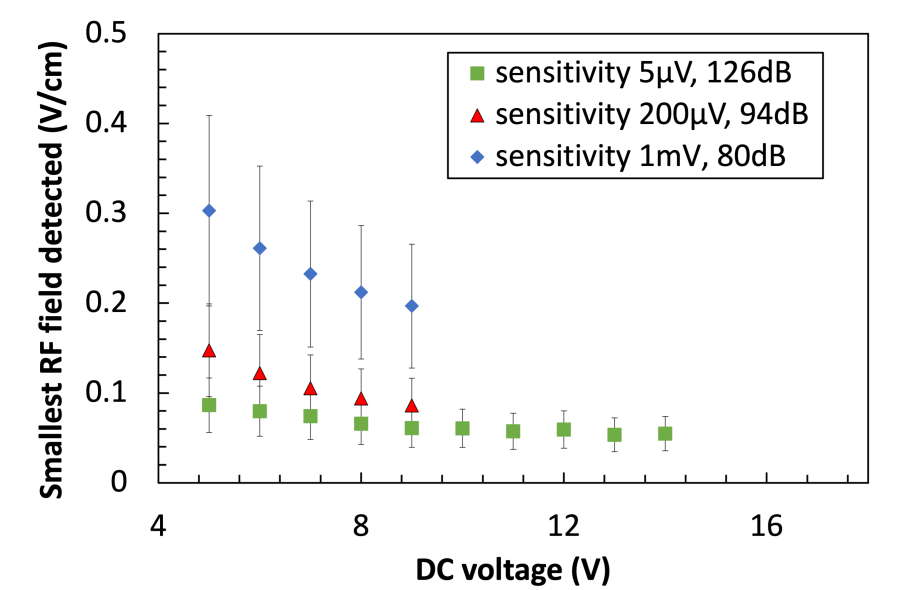

Figure 4.29: Smallest measurable 60MHz RF field vs DC reference voltage across the field plates for the 32s detection state. Measurements using three different gain settings on the lock-in amplifier are shown. Larger gains result in main Stark peak amplitudes corresponding to voltages that are too large for the oscilloscope and/or the lock-in amplifier. In general, larger DC fields improve the RF field detection sensitivity. The smallest measurable field with the current setup and the 32s detection state is 0.056±0.020 V/cm.

Rydberg states with higher principal quantum number can be used to provide a larger polarizability. At the same time, this limits the maximum DC reference field that can be used due to Stark manifold mixing. Measurements analogous to those made with 32s atoms have been made using 35s, 40s, 45s, 50s and 55s states for detection, with the lock-in amplifier input sensitivity set to "$5\mu V$" which is equivalent to 126dB at the optimum detection phase.The optimal DC reference field is selected for each state, expected for 60s state due to the voltage limit too close to zero. The smallest detectable field was found to be 0.0141±0.0050 V/cm using the 50s state and a DC

reference field of 2.84V/cm.

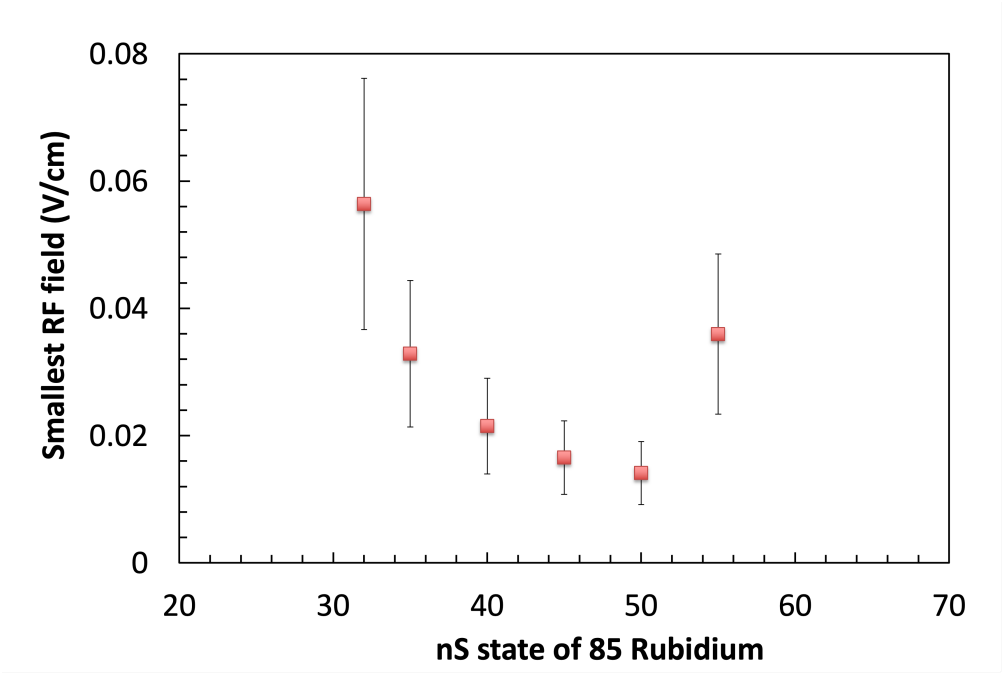

Figure 4.30: Smallest detectable RF field vs ns state of Rubidium. The optimal DC reference fields for the field measurements are found to be: 14.71V/cm for 35S, 8.82V/cm for 40S, 4.98V/cm for 45S, 2.84V/cm for 50V/cm and 0.60V/cm 55S. The smallest measurable field with the current setup is found to be 0.0141±0.0050 V/cm.

4.3 RF detection with unknown DC reference

As discussed previously, accurate measurement of strong RF fields in the presence of a DC reference can be complicated by the coupling of RF power into the DC supply, resulting in RF field dependent changes in the DC reference. A similar coupling of RF power into a voltmeter can limit accurate measurement of the reference voltage applied to field plates. To overcome these issues, we have developed an alternative approach for measuring a (moderate to strong) RF field without direct knowledge of the reference DC field amplitude. The experimental setup is identical to that used for the pulsed EIT RF field measurements described previously.

4.3.1 Theoretical background

The single equation used previously to obtain the RF field from EIT measurements of the sideband to primary Stark peak amplitude ratio is not sufficient for simultaneously determining the DC field as well. However, we can use the measurement of the total Stark shift to obtain additional information on the unknown RF and DC fields. Using the measured Stark shift and amplitude ratios, we can obtain values for both fields from a single EIT spectrum from

$$\begin{aligned} \frac{A_\omega}{A_0} &= \frac{\mathbb{J}_1(\beta)^2}{\mathbb{J}_0(\beta)^2} \\ \Delta &= -\frac{1}{2}\alpha {F_{dc}}^2 - \frac{1}{4}\alpha {F_{rf}}^2 \end{aligned} \tag{4.5}$$

where $\beta = \dfrac{\alpha F_{dc} F_{rf}}{\omega}$.

4.3.2 Demonstration of simultaneous RF and DC field measurement

To test the approach for simultaneous recovery of both the RF and DC fields we use an RF frequency of 80MHz and set the DC voltage to 2.50V without any RF field in present. The frequency separation between the main Stark peak and the zero field peak Δ, as well as the ratio η between the average sideband peak and main peak amplitudes, are measured as a function of increasing RF voltage. The DC and RF voltages on the plate are also directly measured with a high impedance probe.

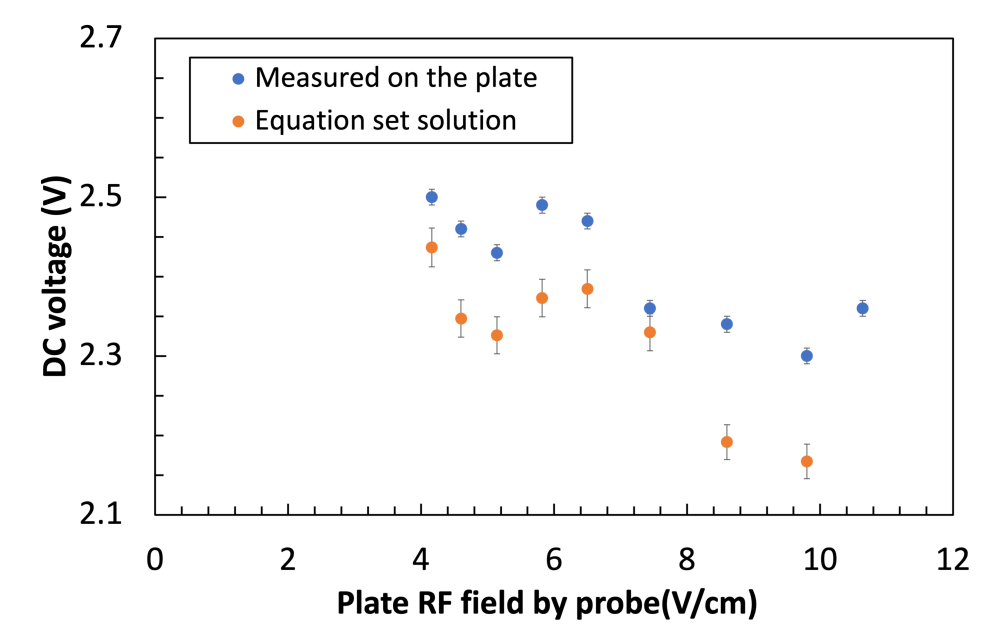

Figure 4.31: DC voltage across the field plates vs applied RF field. The orange dots use the combination of the Bessel function expression for the amplitude ratios and the Stark shift equation to solve for the DC field amplitude. The blue dots are the direct measurements of the DC voltage across the plates using the probe. The DC supply output level on the power supply is not changed during the measurements. The DC voltage is 2.50V for zero RF field. The uncertainty in the direct voltage measurements is smaller than the plotted symbol size.

Fig. 4.31 clearly shows that the DC voltage on the plate is affected by the RF

power supply. The RF field between the plates can be also recovered from the EIT measurements and plotted vs the RF field based on direct probe measurements of the voltage across the plates (Fig. 4.32).

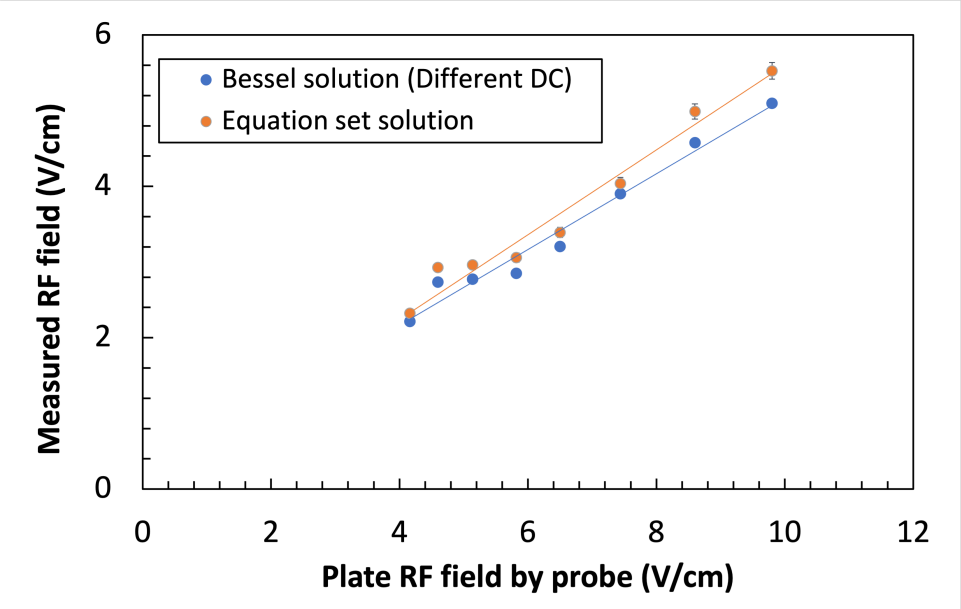

Figure 4.32: EIT measured 80 MHz RF field vs field determined from high impedance probe measurements of RF voltage across the field plates. The orange symbols are the fields determined from the Bessel function expression for the sideband to main Stark peak amplitude ratios combined with the measured Stark shift. The blue symbols use the Bessel function expression for the sideband to main Stark peak amplitude ratios combined with the DC voltage measurements from the direct probe in the Fig. 4.31. Because the static probe voltage measurements are known to be influenced by the RF field, the results shown in orange are assumed to be the most accurate.The fitting result shown with the orange line is F_{EIT}=0.5507F_{probe}+0.0684V/cm, but the P-value for the constant term indicates that it is not statistically significant. The uncertainty in the measured RF field is smaller than the plotted symbol size.

Analogous measurements are made with the DC voltage set to 3V and an RF frequency of 90MHz (Figs. 4.33 and 4.34). The RF fields determined using Eqs. 4.5 vary linearly with the RF field determined from the probe voltage measurements. The y-intercepts for both the 80 and 90MHz cases are not statistically significant, as determined by the P-value from the fits[44].

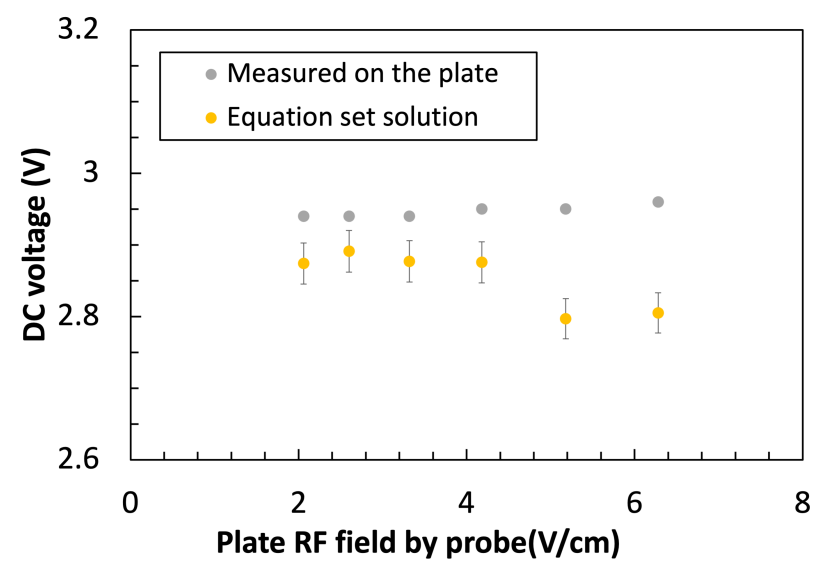

Figure 4.33: DC field determined from EIT measurements vs RF field determined from probe measurements of voltage on the field plates. The yellow dots use the combination of the Bessel function expression for the amplitude ratios and the Stark shift equation to solve for the DC field amplitude. The grey dots are the direct measurements of the DC voltage across the plates using the probe. The DC supply output level on the power supply is not changed during the measurements. The DC voltage is 3.00V for zero RF field.

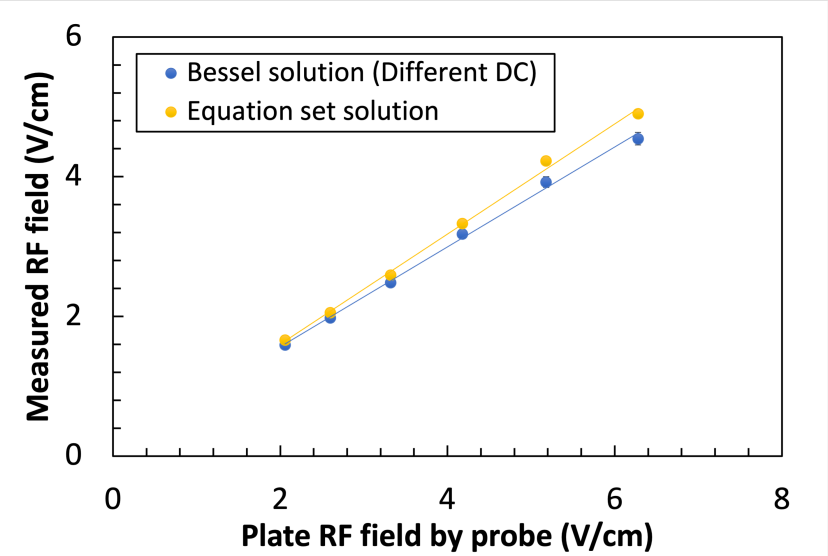

Figure 4.34: EIT measured 90 MHz RF field vs field determined from high impedance probe measurements of RF voltage across the field plates. The yellow symbols are the fields determined from the Bessel function expression for the sideband to main Stark peak amplitude ratios combined with the measured Stark shift. The blue symbols use the Bessel function expression for the sideband to main Stark peak amplitude ratios combined with the DC voltage measurements from the direct probe. Because the static probe voltage measurements are known to be influenced by the RF field, the results shown in yellow are assumed to be the most accurate. The fitting result shown with the yellow line is F_{EIT}=0.7877F_{probe}+0.0221V/cm, but the P-value for the constant term indicates that it is not statistically significant. The uncertainty in the measured RF field is smaller than the plotted symbol size.

As shown in Figs. 4.31 and 4.33, the DC fields between the plates in both 80MHz and 90MHz RF field case are affected by the RF supply, decreasing in magnitude as the RF field increases. Since the RF field also affects the direct probe voltage measurement, it is assumed that the DC field determined from Eqs. 4.5 (in Figs. 4.32 and 4.34), is a more accurate value for the actual field between the plates as compared to that derived from the direct probe voltage measurement. If one uses the measured DC voltage, or the supply voltage at zero RF field, errors in the EIT-based field determination result in non-negligible y-intercepts in fits of the EIT vs probe field values, as shown in Section 4.2.

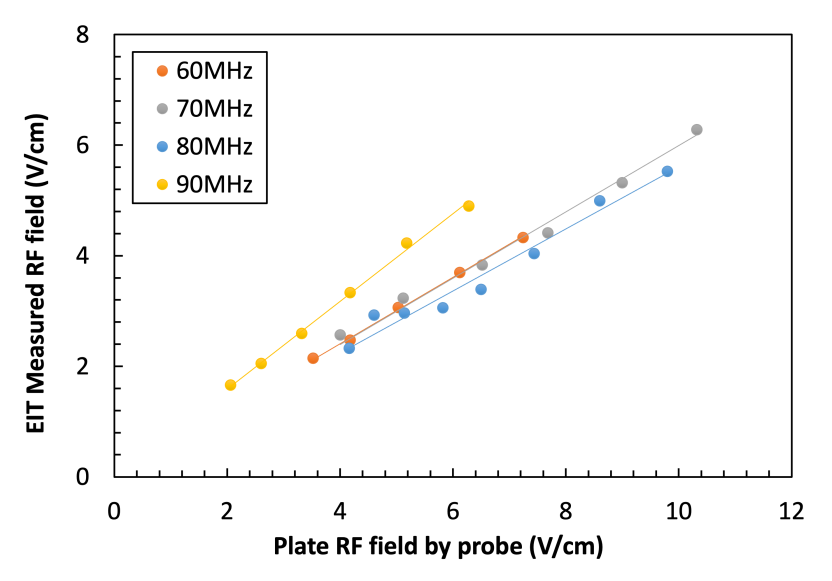

Figure 4.35: EIT vs direct probe measured 60-90MHz RF fields. All the RF field amplitudes are calculated without relying on direct measurements of the DC reference field. Measurements such as these can be used to calibrate the electric RF probe as a function of frequency. The uncertainty in the measured RF field is smaller than the plotted symbol size.

Fig. 4.35 shows a plot of EIT vs probe measurements of 60-90 MHz RF fields. All of measurements do not rely on direct measurements of the static reference field, but from the combined stark shift Δ and the peak amplitude ratio η. The slopes of the linear fits to the 60, 70, 80, and 90MHz data are 0.602±0.013, 0.599±0.028, 0560±0.041 and 0.794±0.021 (all with no significant y-intercept), respectively, providing an accurate calibration of the frequency response of the electric probe.

4.4 RF detection with a synchronous AC reference

As described in the Chapter 3, the reference field in the non-resonant electrometer is not limited to be DC. Depending on the application, RF or low frequency AC fields can work equally well, or better. In this section, we discuss and provide measurements testing the use of low frequency AC fields as the reference. In principle, issues related to the influence of the RF signal field on the DC reference supply might be eliminated or significantly reduced using a capacitively or inductively coupled AC reference.

4.4.1 Experiment Setup

The experimental setup (Fig. 4.36) is the same as described previously except that the the DC reference voltage is replaced with a low frequency AC voltage that is synchronous with the pulse repetition frequency of the coupling laser. The reference is phase locked to the AOM trigger so that the atoms are exposed to the coupling laser at the same phase of the reference field on every laser pulse. In order to achieve this, the 40 kHz oscillator providing the AC reference sine wave and the AOM are triggered from the same delay generator, which allows the user to control the AC phase during the EIT measurement.

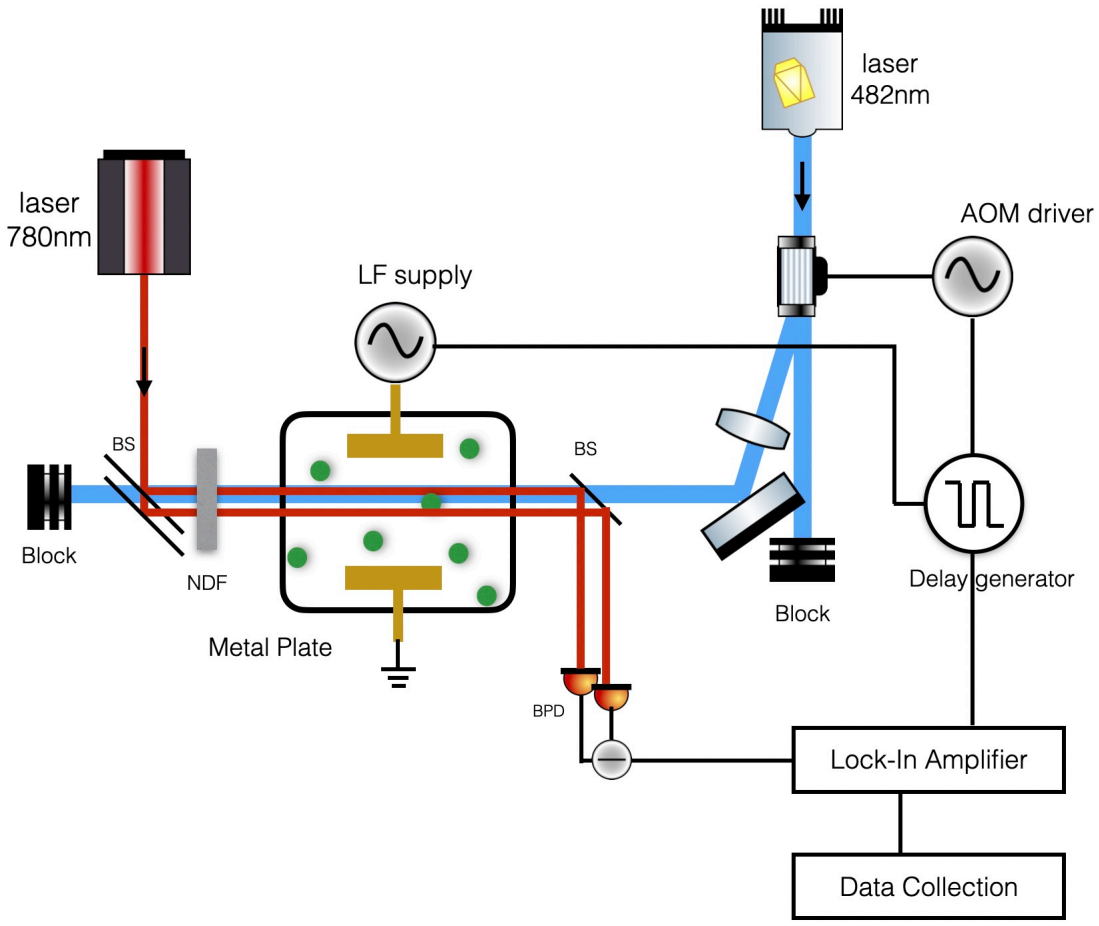

Figure 4.36: Schematic of the experimental implementation for the RF electrometer using an AC reference and pulsed coupling laser experiment. The probe laser configuration remains the same as in the DC reference and cw laser cases. The AOM driver is controlled by a delay generator, which determines how long the AOM driver is on/off during each cycle. The AC oscillator is also triggered by the delay generator, phase-locking the reference AC field with the pulsed coupling laser. The lock-in amplifier receives the transmission signal from the balanced photodiode detector along with the time reference signal from delay generator, and outputs the amplified EIT signal as the coupling laser frequency is scanned.

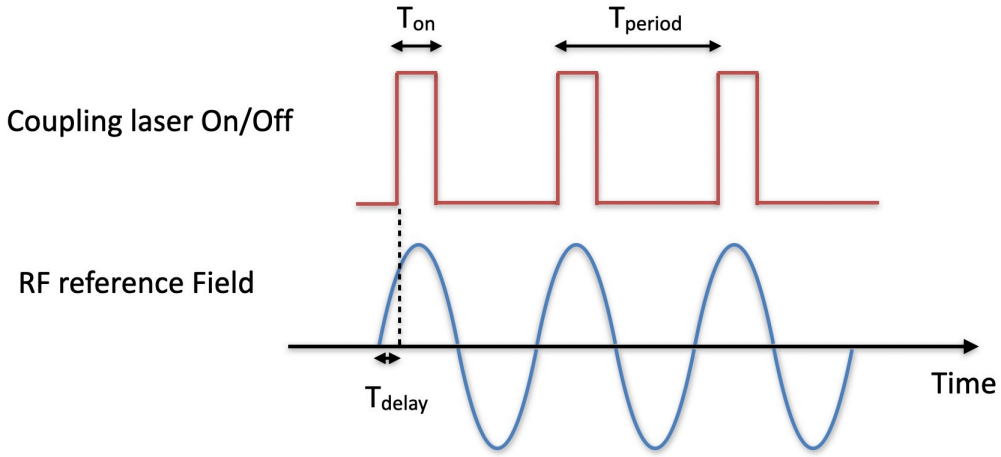

Figure 4.37: Schematic timing of the AC reference field and pulsed coupling laser. The delay generator frequency is set to 40KHz, with a 2% duty cycle for the coupling laser. A40 kHz AC field is produced by a waveform generator that is triggered by the delay generator with a variable time delay T_{delay} relative to the coupling laser pulse.

4.4.2 Pulsed laser duty cycle test

We continue to use a 2% duty cycle for the pulsed coupling laser, so the period for the pulsed laser and AC reference field is $25\mu s$, with a measurement pulse duration of $0.5\mu s$. As the delay time T_{delay} between the coupling laser pulse reference field triggers is varied, so does the phase of the AC reference field during the coupling laser pulse (see Fig. 4.37). Fig. 4.38 shows the effective reference voltage on the field plates as a function of T_{delay}. The reference voltage is derived from EIT measurements of the Stark shift Δ in the absence of any RF field.

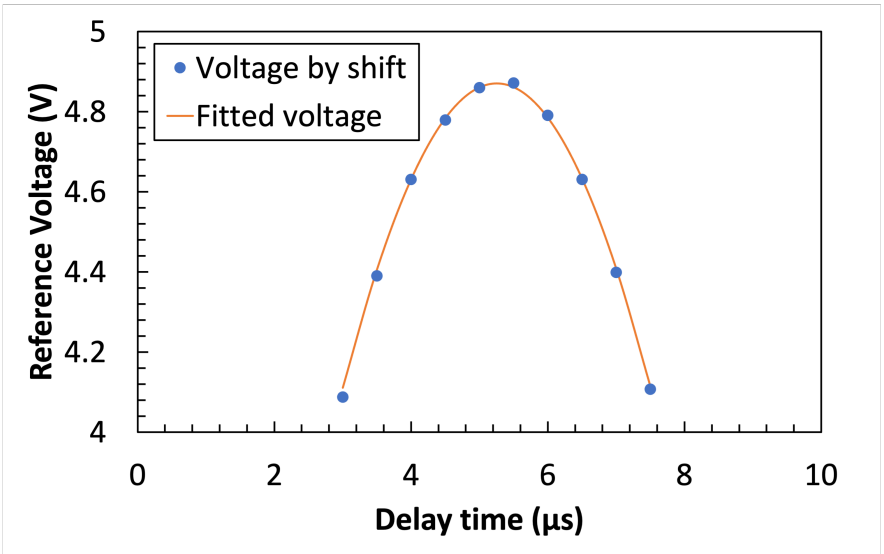

Figure 4.38: Effective reference voltage vs delay time, T_{delay}. The reference voltage is calculated from the measured plate separation and the Stark shift between the zero field peak and main Stark peak in the EIT spectrum. The uncertainty in the measured reference voltage is smaller than the plotted symbol size. The orange line is a 40KHz sine wave fit.

The pulsed coupling laser duty cycle is another factor to consider before using the low frequency RF field as the reference. It is obvious that the duration of the coupling laser pulse needs to be short, otherwise the atoms will experience a changing reference field during the measurement, broadening any EIT peaks that depend on the reference field. Also, to minimize the rate of change in the reference field, T_{delay} should be set to the peak of the measured reference voltage curve (Fig. 4.38).

Fig. 4.39 shows measurements of the effective reference voltage and of the spectral width of the main Stark peak in the EIT spectrum as a function of coupling laser duty cycle. The effective voltage is determined from the measured Stark shift. The reference trigger delay time is set to give the maximum reference voltage, i.e. at $5.25\mu s$.

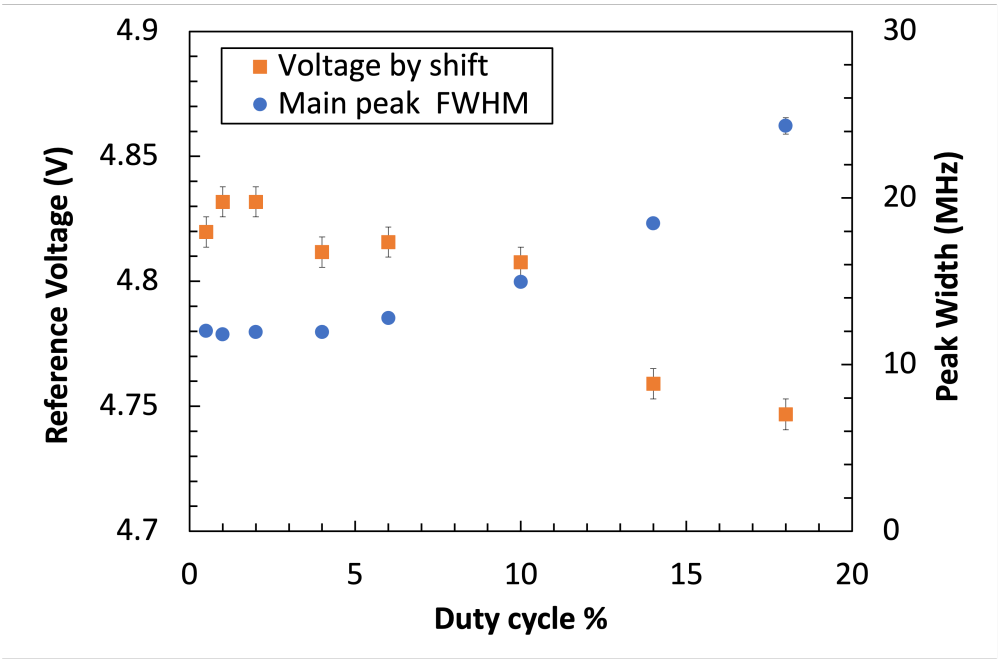

Figure 4.39: Effective reference voltage and main Stark peak width vs coupling laser duty cycle. The reference voltage is calculated from the Stark shift between the zero field peak and the main Stark peak in the EIT spectrum. The decrease in the effective reference voltage, and the increase in the peak width is due to the temporal variation in the reference field during the measurements with longer laser pulse durations. The uncertainty in the main peak width is smaller than the plotted symbol size.

The measurements in Fig. 4.39 show that the duty cycle should be kept under 3%, so that the reference field does not change appreciably during the measurement. These tests confirm the viability of using synchronous AC rather than DC reference fields for RF field measurement using pulsed EIT. The RF field measurement with the synchronous AC reference utilize the same amplitude ratio η through the equations derived for the the DC reference.

4.5 RF detection with a strong RF reference

As described in Chapter 3, replacing the DC reference field with a strong RF reference can also be advantageous for the the measurement of weak RF fields, particularly those at higher frequencies. First, the RF reference can be introduced into the cell without the need for field plates. Second, the amplitude of the difference frequency sidebands resulting from the mixing of the reference and signal RF fields can be much larger than those appearing at the signal RF frequency for a DC field of the same amplitude, by a factor of $\frac{\omega_2}{2\delta}$, where ω_2 is the signal frequency and $\delta = |\omega_1 - \omega_2|$ is the difference between the signal and reference frequencies. The reference frequency can be chosen to make δ as small as possible, limited only by the spectral widths of the EIT peaks (15 to 20 MHz in our current apparatus). Third, by using an appropriate reference frequency, the difference frequency sidebands used for the signal field measurement can fall within 100 MHz or less of the main Stark peak, dramatically reducing the required scan range of the coupling laser frequency for large signal frequencies. The detailed theory is presented in section 3.1.2. The signal field amplitude can be determined using Eq. 3.27 and the measured amplitude ratio η_δ of the average difference frequency sideband to that of the main Stark shifted peak.

4.5.1 Experiment Setup

The experimental setup for implementing the non-resonant Rydberg electrometer with a strong RF reference is shown schematically in Fig. 4.40. For our initial demonstration experiments, the strong reference field is produced by directly connecting an RF generator to the field plates. The weak signal field is generated by a separate RF supply and introduced into the measurement cell using a simple antenna.

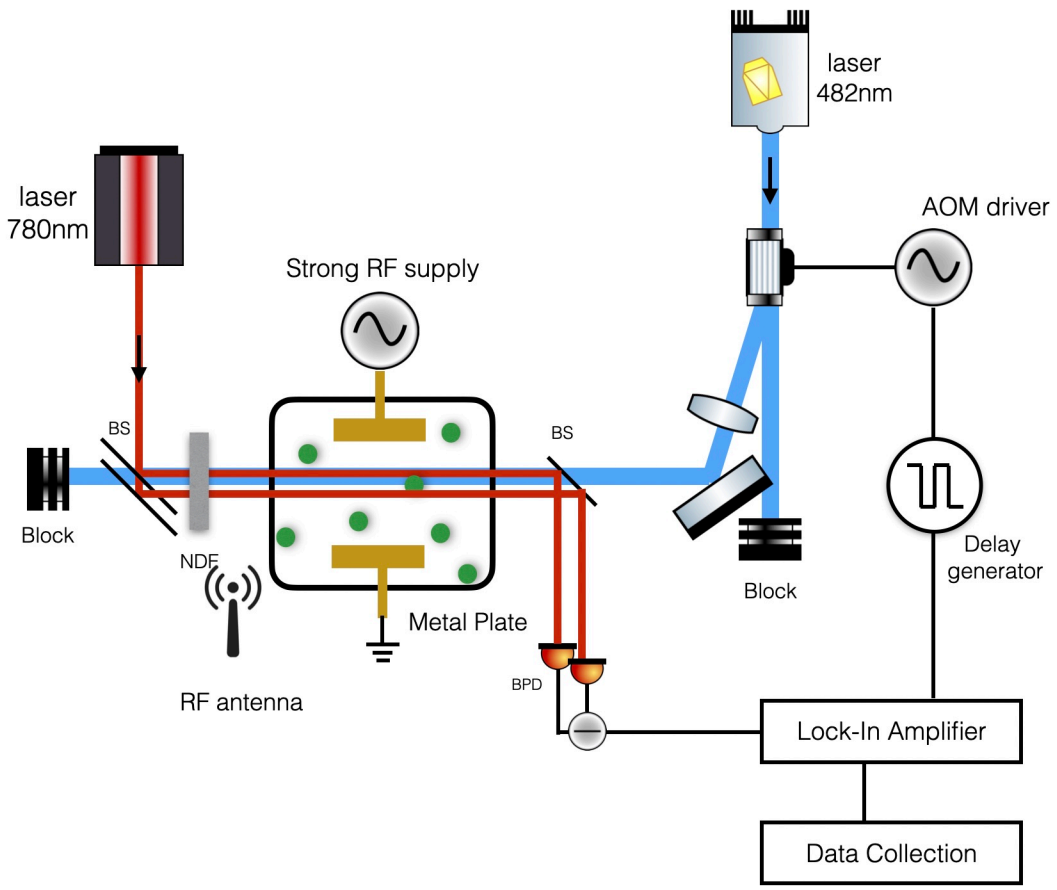

Figure 4.40: Schematic of the strong RF reference Rydberg electrometer setup. The probe laser setup remains the same as for the previously described configurations. The reference RF field is introduced into the detection cell by direct connection of an RF voltage source to the field plates. The reference field amplitude is sufficiently strong to create a measurable Stark shift in EIT spectrum. The RF signal field is introduced into the cell by a simple antenna. As with the DC and AC reference schemes, the signal RF field measured using the Rydberg electrometer can be compared to direct measurements of the voltage across the field plates using a high impedance probe (in this case in the absence of the strong RF reference).

4.5.2 RF field measurement and comparison

To demonstrate the accuracy of the strong RF reference field measurements, we compare them with analogous measurements made with a DC reference (see Fig. 4.42).

For the comparison, the signal RF field frequency is set at 50MHz and the strong RF reference field frequency is set at 90MHz. The DC reference field is set to provide the same Stark shift as the strong 90MHz RF reference (with no signal field present). A typical EIT spectrum is shown in Fig. 4.41.

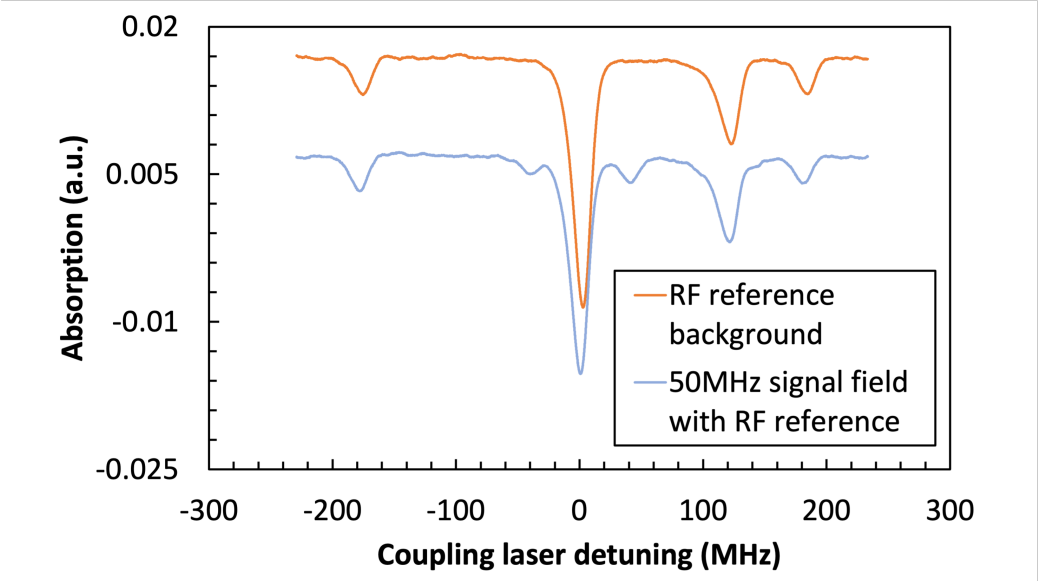

Figure 4.41: EIT spectra in the presence of a strong RF reference and a weaker signal RF field. The spectra shown are the averages of 250 coupling laser frequency scans collected from the lock-in amplifier. The upper orange trace is the EIT spectrum with only the strong 90MHz Rf reference. As the theory predicts in the Fig. 3.14, the main Stark peak is flanked by sidebands at ±180MHz, along with the zero-field peak. The blue trace is the EIT spectrum with the 50MHz signal field plus the 90 MHz reference. In addition to the four peaks in the orange trace (or background trace), there is an extra pair of sidebands appearing at $\pm\delta = 40$MHz away from the main Stark peak. By subtracting the two traces, the average δ sideband amplitude can be used to determine the signal Rf field strength through η_δ.

As outlined in Chapter 3, the signal RF field can be derived from either the amplitude ratio η_δ of the average sideband peaks and main Stark peak or the shift Δ between the main peak and zero field.

$$\eta_\delta = \frac{A_\delta}{A_0} = \frac{\mathbb{J}_1(\beta_-)^2}{\mathbb{J}_0(\beta_-)^2}$$
$$\Delta = -\frac{1}{4}\alpha {F_1}^2/\hbar - \frac{1}{4}\alpha {F_2}^2/\hbar \tag{4.6}$$

where $\beta_- = \dfrac{\alpha\vec{F_1}\cdot\vec{F_2}}{2|\omega_1 - \omega_2|}$.

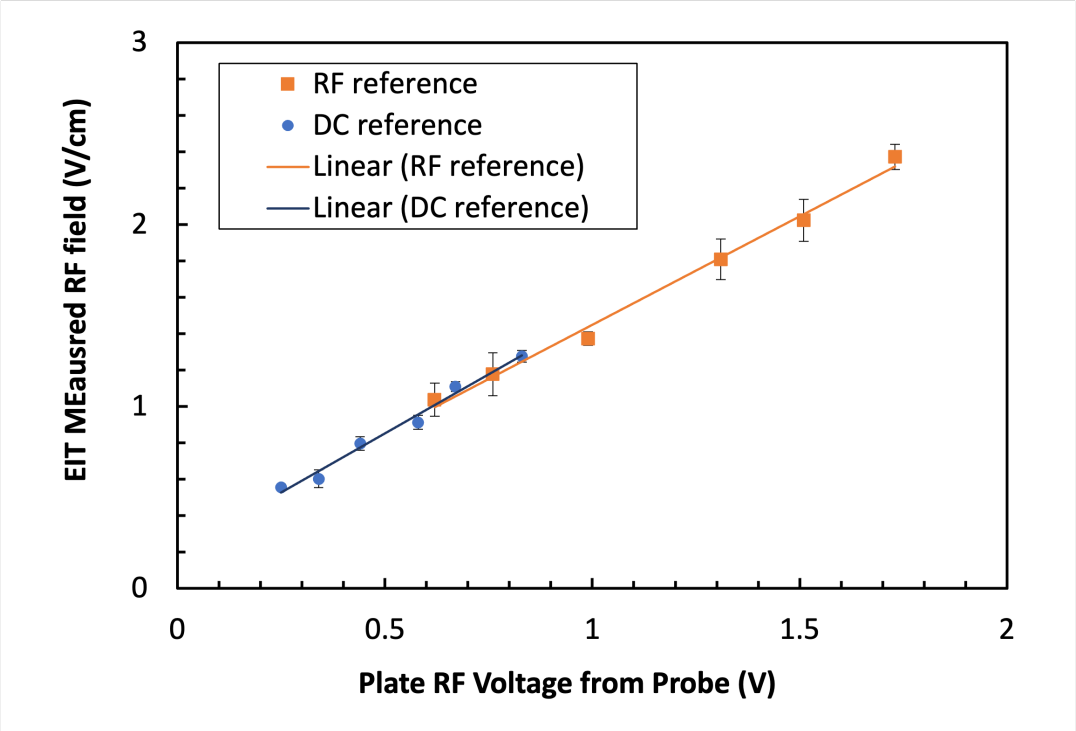

Figure 4.42: Comparison of EIT measurements of RF field amplitude vs probe measurements of RF voltage on the plates for DC and RF reference fields. The RF reference field amplitude is determined from the measured Stark shift. The DC reference field used for the comparison is chosen to give the same Stark shift. The signal RF field measurements are in very good agreement within their uncertainties, demonstrating the effectiveness of the RF reference approach.

For larger signal RF fields, a comparison can be made between the amplitude ratio and peak shift results (see Fig. 4.43). The target field frequency is set at 90MHz while the strong RF reference is set at 40MHz. The amplitude of the RF reference field is set so that the shift of the main Stark peak, Δ is larger than than the RF

difference frequency, δ to avoid any overlap in the zero field and difference frequency peaks.

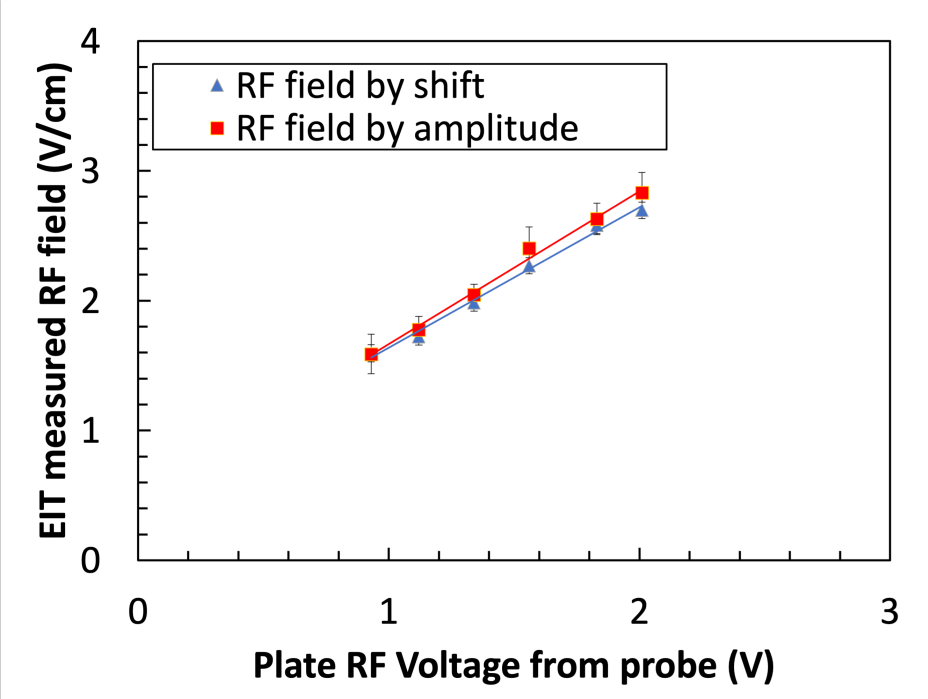

Figure 4.43: Comparison of RF field amplitudes derived from amplitude and Stark shift measurements vs RF voltage on the plates for a strong RF reference. The RF reference field amplitude is determined from the Stark shift with no signal field. The amplitude of an added RF signal field can be determined by measuring the increase of the Stark shift (blue triangles) and through the amplitude ratio expressions (red squares). The two RF signal field measurements are overlapped within their range of uncertainty, so, for larger RF signal fields, either measurement approach can be used.

It is notable that the fits to the RF field vs plate voltage data in Fig. 4.43 have significant y-intercepts. As with the DC reference, this is due to coupling of the RF signal field into the reference signal generator. The measurements in Fig. 4.43 assume that the reference RF field maintains the constant value determined from the Stark shift in the absence of the signal field. However, in the presence of the RF signal field, the RF reference power supply is affected by the RF signal voltage that appears on the field plates. As demonstrated for the DC reference, this issue can be avoided by

using both expressions in Eq. 4.6 to determine both the signal and reference RF field amplitudes rather than assuming a constant reference field value.

As noted previously, use of the strong high frequency RF reference field in place of a DC or low frequency (LF) AC reference can eliminate the need for plates or wires in the measurement cell, as the high frequency RF reference and signal can propagate through free space into the Rb cell. It also extends the measurable frequency range of the signal RF field to much higher frequencies. That range would otherwise be limited by the frequency scanning range of the coupling laser (200 to 300MHz in our current setup) for DC and LF AC reference fields. Compared to the established methods for resonant (or near resonant) RF field detection, our platform can fill the gaps between different resonant frequencies, providing a solution for sensitive non-resonant, self-calibrating, broad band RF field detection into the 1GHz range and higher.

Chapter 5

Conclusions and Outlook

5.1 Weak to strong RF field detection summary

As described in Chapter 3 and demonstrated in Chapter 4, optimal measurement of RF fields of different amplitudes using non-resonant Rydberg EIT requires an appropriate choice of reference field amplitude (and type) and the use of the appropriate equations for extracting the signal field strength from spectroscopic amplitude ratios or frequency differences. Fig. 5.1 shows a plot of limiting values of the parameters β and Stark shift Δ_{rf} for accurately employing different approaches for extracting the RF field from EIT measurements. The specific limits shown assume a 60MHz RF field and Rb 32s detection atoms.

Multiple lines are plotted in Fig.5.1. The three solid curves are related to the parameter $\beta = \dfrac{\alpha F_{dc} F_{rf}}{\omega}$, which is proportional to the product of the static reference field and signal RF field. As shown in Section 3.1.1 and Fig. 3.12, when $\beta \leq 0.2$ (in the region blow the black line in Fig. 5.1), F_{rf} can be directly determined by Eq.3.23 with an error <1%.

$$F_{rf} = \frac{\omega}{\alpha F_{dc}}\beta = \frac{2\omega}{\alpha F_{dc}}\sqrt{\frac{A_\omega}{A_0}}$$

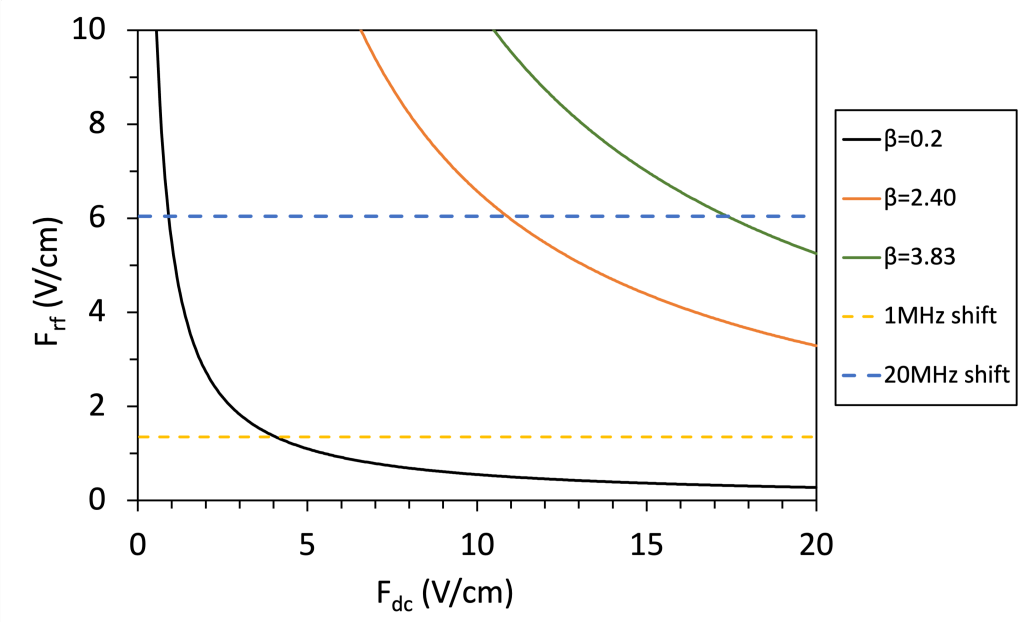

Figure 5.1: Limiting values of β and Δ_{rf} for determining a signal RF field magnitude using different theoretical expressions and aspects of the measured EIT spectrum, plotted vs RF signal field and DC reference field. The calculations assume a 60MHz RF field and 32s detection state. The three solid curves are related to limiting values of β, (proportional to the product of F_{rf} and F_{dc}. The black line shows the upper limit of the small β approximation, in which the Bessel functions in the exact expressions can be replaced by a simplified expression in which β is directly proportional to the square root of the sideband to main Stark peak amplitude, and for which the approximation error is <1%. The red line is the upper limit for using the ratio η of the average first order sideband amplitude to that of the main Stark peak with <1% error. The green line is the upper limit for using the ratio η_2 of the average second order sideband amplitude to that of the main Stark peak with <2% error. The blue dashed line is the lower value of F_{rf} which can be measured directly from the Stark shift, without any reference field present. The yellow dashed line gives the smallest value of F_{rf} for which the combined amplitude ratio and Stark shift equation sets can be used to simultaneously determine both the static reference field and RF signal field.

The measurement of the weakest RF fields falls into this amplitude regime, as discussed in Section 4.2.7.

In Section 3.1.1, we also identified the limits for using different sidebands for the peak amplitude ratio measurements used to determine the RF fields. For the region

between the black and red lines in Fig. 5.1, F_{rf} can be determined using Eq. 3.20, with an error of <1%.

$$\frac{A_\omega}{A_0} = \frac{\mathbb{J}_1(\beta)^2}{\mathbb{J}_0(\beta)^2}$$

In the region between the red and green lines, F_{rf} can be determined by Eq.3.24 with an error of <2%..

$$\frac{A_{2\omega}}{A_\omega} = \frac{\mathbb{J}_2(\beta)^2}{\mathbb{J}_1(\beta)^2}$$

The blue dashed line shows the RF field that results in a 20MHz shift of the main Stark peak relative to the zero field peak, in an RF field alone. The 20MHz value is chosen to be comparable to the observed EIT spectral resolution ($\sim$ 15 to 20MHz). So, for the region above the blue line, the main Stark peak and the zero field peak can be resolved in the EIT spectrum, and the RF field can be determined either using Eq. 3.27 for the Stark shift in the absence of a reference field, or using Eq. 3.29 in terms of the ratio of the 2ω sideband amplitudes to the main Stark peak amplitude, as a function of $\gamma = \frac{\alpha F_{rf}^2}{8\omega}$, using Eq.3.29.

$$\Delta = -\alpha {F_{rf}}^2/4$$
$$or \quad A_{2\omega}/A_0 = (\mathbb{J}_1(\gamma))^2/(\mathbb{J}_0(\gamma))^2$$

Section 4.1.7 demonstrates the application of these two equations when the RF field is strong enough to resolve the zero field and main Stark peaks and to produce observable 2ω sidebands.

The dashed yellow line shows the RF field that, alone, results in a 1MHz shift of

the main Stark peak, relative to the zero field peak. This 1MHz value is chosen to be comparable to the uncertainty of the peak shift measurement. So, for the region between the yellow and blue dashed lines, Eq. 3.8 for the combined Stark shift can be used along with the appropriate amplitude ratio formula to simultaneously determine the magnitudes of the static reference field and RF signal field (see Section 4.3).

$$\Delta = -\frac{1}{2}\alpha {F_{dc}}^2 - \frac{1}{4}\alpha {F_{rf}}^2$$

Fig. 5.2 shows a plot completely analogous to Fig. 5.1 plot, but for a 25s detection state. With the smaller α, all of the lines move to higher values in the DC-RF field plot, illustrating that the various small RF field approximations can be applied over a larger amplitude range.

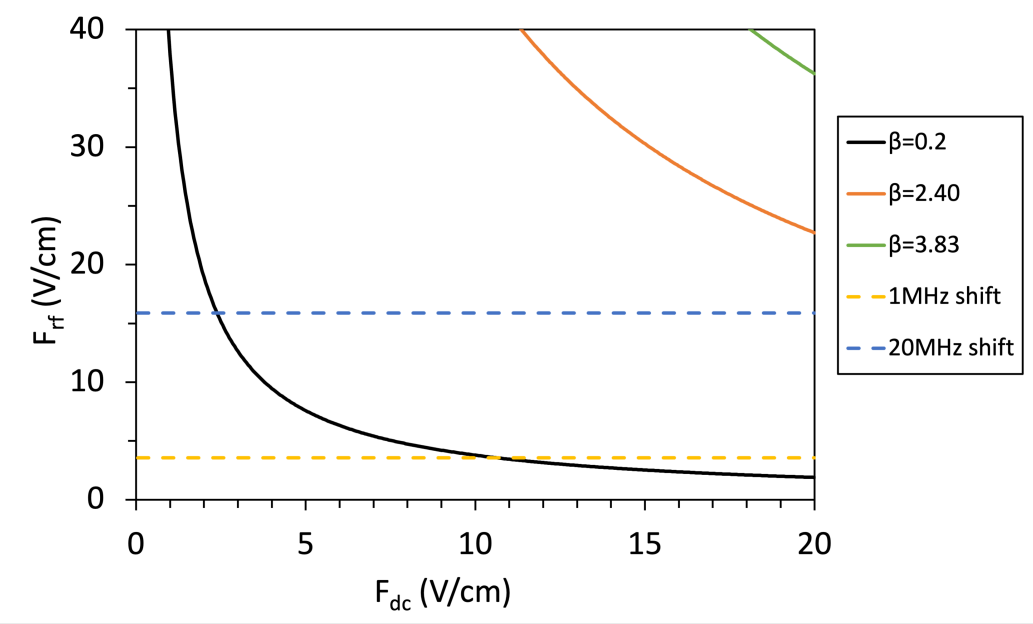

Figure 5.2: Limiting values of β and Δ_{rf} for determining a signal RF field magnitude using different theoretical expressions and aspects of the measured EIT spectrum, plotted vs RF signal field and DC reference field, completely analogous to Fig. 5.1 except that the calculations assume a 25s detection state.

The regimes for non-resonant Rydberg detection of RF fields with a strong RF reference can identified using plots similar to those shown in Figs. 5.1 and 5.2. In this case the limits are defined by curves at constant β_- as a function of F_1 and F_2.

5.2 Non-resonant RF electrometer sensitivity

The smallest RF field measurable with the current apparatus is discussed in section 4.2.7, and can be obtained directly from Rydberg EIT spectra using Eq.3.23. To reach the highest sensitivity from our non-resonant RF electrometer, several parameters can be optimized.

First, instead of using Eq.3.23 with a DC reference field, a strong RF reference field can be employed with Eq.3.37.

$$F_{2,\|} = \frac{2\delta}{\alpha F_1}\beta_- = \frac{4\delta}{\alpha F_1}\sqrt{\frac{A_\delta}{A_0}}$$

By comparing with the DC reference, We can see that when $2\delta < \omega_2$ (i.e. twice the difference frequency is less than the signal frequency), the sensitivity of the electrometer with a strong RF reference exceeds that with a DC reference, by a factor of $\omega_2/(2\delta)$ As noted previously, the smallest useful difference frequency is the spectral width of the EIT peaks. In the current apparatus, that is ∼15-20 MHz. However, it could be significantly reduced, in principle, using colder atoms or a a different EIT scheme in which the probe and coupling lasers have (more) similar wavelengths or larger beam profiles.

For the room temperature cell and current laser excitation scheme, δ should be chosen to be ∼20MHz for the highest detection sensitivity. Thus, for an RF frequency $\omega_2 > 40$MHz, the strong RF reference provides higher sensitivity.

It is also possible to improve on the smallest measurable amplitude ratio $\eta_{min} = \frac{A_{\omega,min}}{A_{0,max}}$ in the EIT spectrum.$A_{\omega,min}$ is generally determined by the noise level of the lock-in amplifier which depends on different gain settings. $A_{0,max}$ is determined

by the signal amplitude before entering the lock-in amplifier and by the maximum voltage output of the amplifier. In principle, with the current apparatus, A_0 could be made as large as 10V (the maximum input level) at the smallest gain setting ($500m$V sensitivity for the current instrument) by employing significantly higher bias voltages on the balanced photodiode (see Fig.2.9). The sideband amplitude could then be measured separately at a higher gain setting, and the main peak amplitude re-scaled by the fractional increase in the amplifier gain. Fig. 5.3 shows the experimentally realized and potentially achievable minimum measurable η values vs lock-in input sensitivity (higher input sensitivity in mV corresponds to lower amplifier gain).

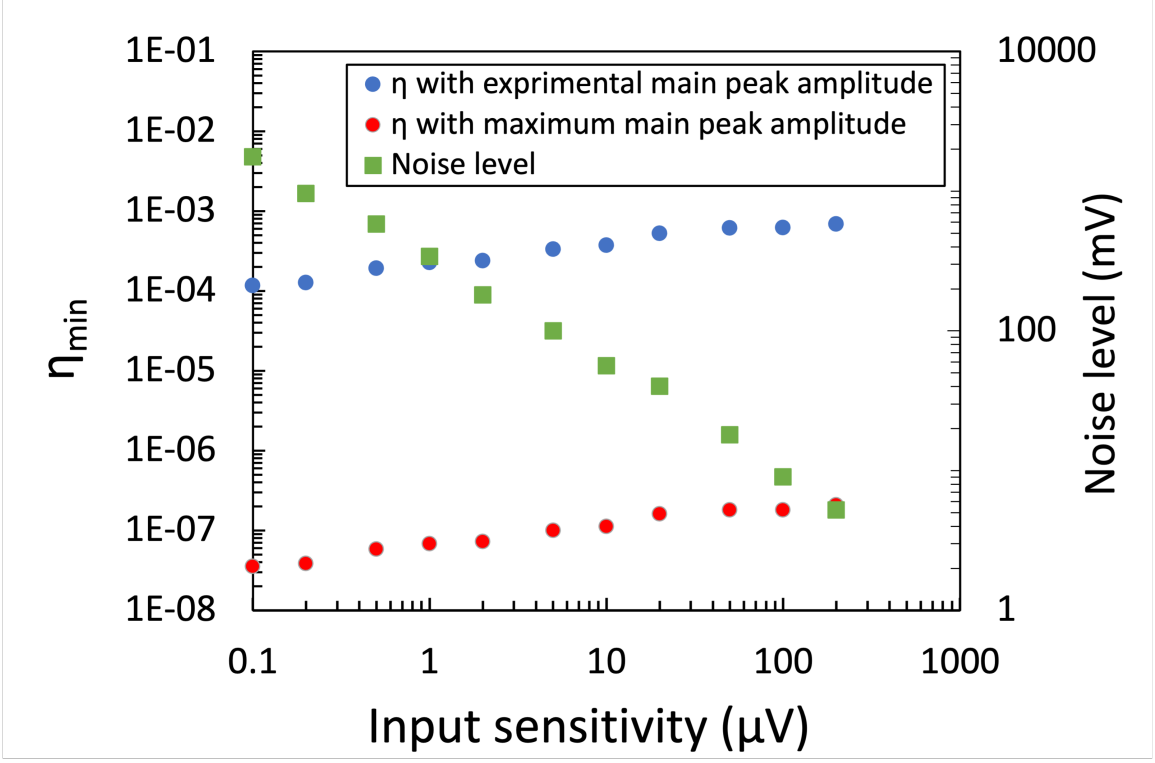

Figure 5.3: Minimum η vs different lock-in input sensitivity setting. Higher input sensitivity corresponds to lower amplifier gain. The green dots are the background noise level, primarily leakage at the lock-in frequency f_r vs input sensitivity setting. The blue dots are the η_{min} calculated assuming the smallest measurable sideband peak amplitude is equal to the amplifier noise level, and a typical measured main peak amplitude of $A_0 = 7.560$V at an input sensitivity of 200μV. The red dots are the η_{min} calculated assuming the smallest measurable sideband peak amplitude is equal to the amplifier noise level, and the main peak amplitude has its largest possible value, $A_0 = 10$V with input sensitivity of $500m$V. By separately measuring and rescaling A_0 the minimum η value is reduced by 3-4 orders of magnitude

In addition, the product of αF_1 in Eq.3.37 should be as large as possible. This has been addressed previously in Fig 4.30, which shows the minimum detectable field vs n using a DC reference field and without rescaling of A_0. From the stark maps, we can solve for the maximum usable static reference field $F_{dc,max}$ (defined by the ns state mixing with the (n-2)f state manifold), and then plot the theoretical maximum product of $\alpha F_{dc,max}$ for each ns state (see Fig 5.4).

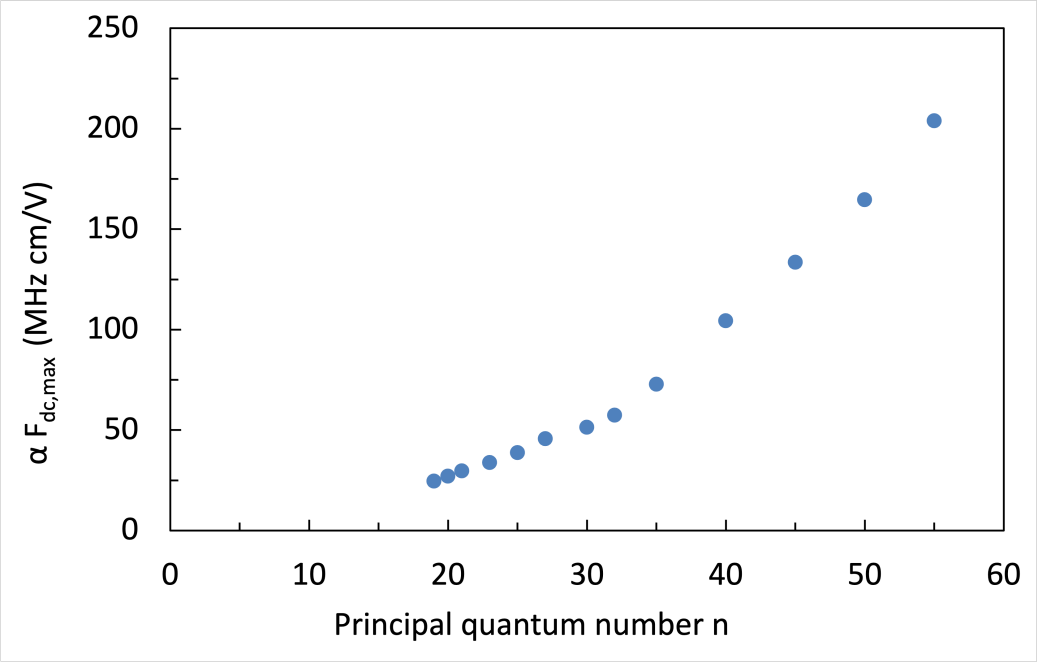

Figure 5.4: Theoretical maximum product $\alpha F_{dc,max}$ vs principal quantum number n of the Rydberg state. The polarizability is calculated for each Rydberg state using Stark maps such as those shown in Fig. 3.1, with $F_{dc,max}$ defined as the crossing point of the ns state with the Stark state adiabatically connected to the (n-2)f level. The product $\alpha F_{dc,max}$ thus obtained is the theoretical maximum in Eq. 3.23.

The maximum reference field needs to be smaller than $F_{dc,max}$ for the adiabatic theory underlying the non-resonant electrometer operation to be valid. In practice, the upper limit for reference field can be identified as the point where the sidebands and main Stark peaks significantly broaden and are difficult to clearly identify. The theoretical maximum RF reference field $F_{1,max}$ is the same as DC reference case, but due to the time-evolving nature of the RF field, $F_{1,max}$ can be more closer to the crossing field point of the Stark manifold before the peak broadening becomes an issue. The maximum DC/RF reference field needs determined individually for each ns detection state.

Putting these all together, the smallest measurable RF field that can be extracted

using 3.37 requires the use of δ_{min}, $(\alpha F_1)_{max}$ and η_{min}, i.e.

$$F_{2,\parallel,min} = \frac{4\delta_{min}}{(\alpha F_1)_{max}} \sqrt{(\frac{A_\delta}{A_0})_{min}} \tag{5.1}$$

With all the parameter optimized and our current apparatus, the smallest field should be approximately 0.1mV/cm, obtained with $\delta = 20$MHz, a lock-in input sensitivity of 100 nV, a $50s$ Rydberg detection state $50s$ and the RF reference field set to 2.84V/cm. Compared to the smallest field actually measured with the apparatus, 14mV/cm, this estimate represents an improvement of over three orders of magnitude, making the non-resonant approach more competitive with various implementations of the resonant Rydberg RF electrometer [10], [11].

Additional future improvements can be made to reduce the background noise in the EIT spectrum, by replacing the older and fairly inexpensive lock-in amplifier that is currently in use with a more advanced lock-in amplifier with less noise due to reference frequency leakage and, potentially, a larger dynamic range. Improved coupling and probe laser power and beam pointing stability could reduce signal noise from the balanced photodiode, and a smaller plate separation could improve the field inhomogeneity for a narrower EIT linewidth at large reference fields.

5.3 Outlook for the non-resonant EIT amplitude-based Rydberg RF electrometer

Currently, using standard EIT spectroscopy for measuring the Autler-Townes splitting of resonantly driven Rydberg atoms, the RF field strength can be determined down to a few mV/cm [9], [10]. Using more accurate measurements involving a reference RF field and a heterodyne measurement, signal RF field strengths down to $\sim 0.2 \mu$V/cm have been reported[45]. These frequency-based measurements are necessarily restricted to resonant frequencies (which, in principal, can be Stark tuned with the addition of a third field), from MHz to THz. By comparison, our non-resonant self-calibrating amplitude-based Rydberg RF electrometer has a list of advantages compared to the resonant approaches.

- Wide frequency response (in principle, MHz to THz with correct choice of detection state)
- Broadband RF detection (demonstrated in Fig. 4.2)
- Direct measurement of RF spectrum (in contrast to other heterodyne non-resonant RF field sensor schemes[46])
- Prior determination of reference field amplitude not required for large signal fields (explained in Fig. 5.1)
- Full frequency range application (MHz to THz) if combined with resonant technique[9]

In the future, higher frequency microwave (MW) reference fields can be used to test the non-resonant electrometer at GHz frequencies. In that case, the reference field can be introduced into the detection cell without the need for metal plates in or around the cell, creating an RF detector with near 360° access and without conductors affecting the RF/MW radiation to be measured. Variation of the linear polarization of the reference radiation will allow for measurements of the directionality of the signal field. Implementation will require a high power MW power supply and the ability to direct the strong MW reference into the Rubidium cell, uniformly throughout the laser-atom interaction region, which is a challenge for our current apparatus.

For higher frequency signal and reference fields, checking for (near) resonant (single or multi-photon) interactions is essential. Theoretically, near resonance conditions can be identified through Stark map calculations. In practice, deviations from the adiabatic, quadratic Stark shift response can be identified by testing the performance of the electrometer for different detection states, as these will have different (near) resonant responses. If the signal RF field of interest is at a resonant frequency between two dipole coupled Rydberg states, then the AT splitting measurement can be performed in the same setup without the need to replacing any components.

Furthermore, our non-resonant amplitude-based RF electrometer can be integrated into a more compact format. The saturated absorption spectroscopy for the probe laser and the Rydberg EIT spectroscopy can be performed in the same Rubidium cell, the size of which can be made significantly smaller if the internal plates are not required to establish the reference field. Reflecting window coatings could be employed to enable beam multiple passes and maintain sufficient optical path length in a significantly shorter cell. The probe and coupling laser beams can be coupled into optical fibers and then sent into the cell, to be less vulnerable to external vibrations

and beam pointing issues. It should be possible to design a movable detector with a volume of only a few cm^3, considerably smaller than traditional classical RF dipole antennas, for sensitive, accurate RF field detection for free space, underground, or underwater scientific and technological applications.

References

[1] P6139A, Tektronix. [Online]. Available: https://www.tek.com/en/p6139a-manual/p6139a-instructions.

[2] M. Kanda, "Standard probes for electromagnetic field measurements," en, no. 41, 1993. [Online]. Available: https://www.nist.gov/publications/standard-probes-electromagnetic-field-measurements.

[3] D. R.Hartree, "The wave mechanics of an atom with a non-coulomb central field. part i. theory and methods," *Mathematical Proceedings of the Cambridge Philosophical Society*, vol. 24, no. 1, pp. 89–110, 1928. DOI: https://doi.org/10.1017/S0305004100011919.

[4] E. Tiesinga, P. J. Mohr, D. B. Newell, and B. N. Taylor. "The 2018 codata recommended values of the fundamental physical constants (web version 8.1)." (), [Online]. Available: https://physics.nist.gov/cuu/Constants/. (accessed: 01.09.2022).

[5] T. F. Gallagher, *Rydberg Atoms*, ser. Cambridge Monographs on Atomic, Molecular and Chemical Physics. Cambridge University Press, 1994. DOI: 10.1017/CBO9780511524530.

[6] B.G.Richards, "Dipole-dipole interactions in a cold rydberg gas," Ph.D. dissertation, University of Virginia, 2017. DOI: https://doi.org/10.18130/V3MB4V.

[7] "Arc: An open-source library for calculating properties of alkali rydberg atoms," *Computer Physics Communications*, vol. 220, pp. 319–331, 2017, ISSN: 0010-4655. DOI: https://doi.org/10.1016/j.cpc.2017.06.015.

[8] "Microwave electrometry with rydberg atoms in a vapour cell using bright atomic resonances," *Nature Physics*, vol. 8, pp. 819–824, 11 2012, ISSN: 17452481. DOI: 10.1038/nphys2423.

[9] "Atom based rf electric field sensing," *Journal of Physics B: Atomic, Molecular and Optical Physics*, vol. 48, 20 Sep. 2015, ISSN: 13616455. DOI: 10.1088/0953-4075/48/20/202001.

[10] C. L. Holloway, J. A. Gordon, S. Jefferts, *et al.*, "Broadband rydberg atom-based electric-field probe for si-traceable, self-calibrated measurements," *IEEE Transactions on Antennas and Propagation*, vol. 62, no. 12, pp. 6169–6182, 2014. DOI: 10.1109/TAP.2014.2360208.

[11] "Electric field metrology for si traceability: Systematic measurement uncertainties in electromagnetically induced transparency in atomic vapor," *Journal of Applied Physics*, vol. 121, 23 2017, ISSN: 10897550. DOI: 10.1063/1.4984201.

[12] S. Kumar, H. Fan, H. Kübler, A. J. Jahangiri, and J. P. Shaffer, "Rydberg-atom based radio-frequency electrometry using frequency modulation spectroscopy in room temperature vapor cells," *Opt. Express*, vol. 25, no. 8, pp. 8625–8637, Apr. 2017. DOI: 10.1364/OE.25.008625.

[13] M. T. Simons, A. H. Haddab, J. A. Gordon, and C. L. Holloway, "A rydberg atom-based mixer: Measuring the phase of a radio frequency wave," *Applied Physics Letters*, vol. 114, 11 2019, ISSN: 00036951. DOI: 10.1063/1.5088821.

[14] A. K. Mohapatra, T. R. Jackson, and C. S. Adams, "Coherent optical detection of highly excited rydberg states using electromagnetically induced transparency," *Phys. Rev. Lett.*, vol. 98, p. 113 003, 11 Mar. 2007. DOI: 10.1103/PhysRevLett.98.113003.

[15] K.-J. Boller, A. Imamolu, and S. E. Harris, "Observation of electromagnetically induced transparency," *Phys. Rev. Lett.*, vol. 66, pp. 2593–2596, 20 May 1991. DOI: 10.1103/PhysRevLett.66.2593.

[16] M. Fleischhauer, A. Imamoglu, and J. P. Marangos, "Electromagnetically induced transparency: Optics in coherent media," *Rev. Mod. Phys.*, vol. 77, pp. 633–673, 2 Jul. 2005. DOI: 10.1103/RevModPhys.77.633.

[17] J. Gea-Banacloche, Y.-q. Li, S.-z. Jin, and M. Xiao, "Electromagnetically induced transparency in ladder-type inhomogeneously broadened media: Theory and experiment," *Phys. Rev. A*, vol. 51, pp. 576–584, 1 Jan. 1995. DOI: 10.1103/PhysRevA.51.576.

[18] M. J. McDonnell, D. N. Stacey, and A. M. Steane, "Laser linewidth effects in quantum state discrimination by electromagnetically induced transparency," *Phys. Rev. A*, vol. 70, p. 053 802, 5 Nov. 2004. DOI: 10.1103/PhysRevA.70.053802.

[19] J. E. Thomas and W. W. Quivers, "Transit-time effects in optically pumped coupled three-level systems," *Phys. Rev. A*, vol. 22, pp. 2115–2121, 5 Nov. 1980. DOI: 10.1103/PhysRevA.22.2115.

[20] L. Hao, Y. Jiao, Y. Xue, *et al.*, "Transition from electromagnetically induced transparency to autler-townes splitting in cold cesium atoms," *New Journal of Physics*, vol. 20, 7 2018, ISSN: 13672630. DOI: 10.1088/1367-2630/aad153.

[21] HTC3000 3 A Low Profile OEM Temperature Controller, wavelength electronics. [Online]. Available: https://www.teamwavelength.com/download/Datasheets/htcseries.pdf.

[22] T. W. Hänsch, "Repetitively pulsed tunable dye laser for high resolution spectroscopy," *Appl. Opt.*, vol. 11, no. 4, pp. 895–898, Apr. 1972. DOI: 10.1364/AO.11.000895.

[23] K. C. Harvey and C. J. Myatt, "External-cavity diode laser using a grazing-incidence diffraction grating," *Opt. Lett.*, vol. 16, no. 12, pp. 910–912, Jun. 1991. DOI: 10.1364/OL.16.000910.

[24] K. Liu and M. G. Littman, "Novel geometry for single-mode scanning of tunable lasers," *Opt. Lett.*, vol. 6, no. 3, pp. 117–118, Mar. 1981. DOI: 10.1364/OL.6.000117.

[25] M. G. Littman and H. J. Metcalf, "Spectrally narrow pulsed dye laser without beam expander," *Appl. Opt.*, vol. 17, no. 14, pp. 2224–2227, Jul. 1978. DOI: 10.1364/AO.17.002224.

[26] M. G. Littman, "Single-mode operation of grazing-incidence pulsed dye laser," *Opt. Lett.*, vol. 3, no. 4, pp. 138–140, Oct. 1978. DOI: 10.1364/OL.3.000138.

[27] User's guide for 6000 Vortex Series tunable diode laser, New Port,Inc. [Online]. Available: https://www.manualslib.com/manual/2057907/New-Focus-Vortex-6000-Series.html#manual.

[28] TA/DL-SHG pro Frequency Doubled High Power Laser System Manual, Toptica Photonics AG. [Online]. Available: https://www.toptica.com/products/tunable-diode-lasers/frequency-converted-lasers/ta-shg-pro.

[29] R. N. Hall, G. E. Fenner, J. D.Kingsley, T. J.Soltys, and R. O.Carlson., "Coherent light emission from gaas junctions," *Phys. Rev. Lett.*, vol. 9, pp. 366–368, 9 Nov. 1962. DOI: 10.1103/PhysRevLett.9.366.

[30] M. I. Nathan, W. P. Dumke, G. Burns, F. H. Dill, and G. Lasher, "Stimulated emission of radiation from gaas p-n junctions," *Applied Physics Letters*, vol. 1, no. 3, pp. 62–64, 1962. DOI: 10.1063/1.1777371.

[31] R. W. P. Drever, J. L. Hall, F. V. Kowalski, *et al.*, "Laser phase and frequency stabilization using an optical resonator," *Applied Physics B*, vol. 31, no. 2, pp. 97–105, 1983. DOI: 10.1007/BF00702605.

[32] E. D. Black, "An introduction to pound–drever–hall laser frequency stabilization," *American Journal of Physics*, vol. 69, no. 1, pp. 79–87, 2001. DOI: 10.1119/1.1286663.

[33] G. Pacheco, "Variable optical attenuator using double acousto-optic modulator," May 2006.

[34] J. I. Kim, R. B. B. Santos, and P. Nussenzveig, "Manipulation of cold atomic collisions by cavity qed effects," *Phys. Rev. Lett.*, vol. 86, pp. 1474–1477, 8 Feb. 2001. DOI: 10.1103/PhysRevLett.86.1474.

[35] D. A. Smith and I. G. Hughes, "The role of hyperfine pumping in multilevel systems exhibiting saturated absorption," *American Journal of Physics*, vol. 72, 5 2004, ISSN: 0002-9505. DOI: 10.1119/1.1652039.

[36] Y. Painchaud, M. Poulin, M. Morin, and M. Têtu, "Performance of balanced detection in a coherent receiver," *Opt. Express*, vol. 17, no. 5, pp. 3659–3672, Mar. 2009. DOI: 10.1364/OE.17.003659.

[37] LB1005 High-Speed Servo Controller, New Port. [Online]. Available: https://www.newport.com/medias/sys_master/images/images/he7/h11/8797219487774/New-Focus-LB1005-Datasheet.pdf.

[38] VFE Series Variable Frequency Source, IntraAction Corp. [Online]. Available: https://www.lambdaphoto.co.uk/intraaction-vfe-series-variable-frequency-source.html.

[39] 83620B Synthesized Swept-Signal Generator, Agilent Technologies. [Online]. Available: https://www.keysight.com/us/en/product/83620B/synthesized-sweptsignal-generator-001--20-ghz.html#resources.

[40] Model DG535 Digital Delay/Pulse Generator, Stanford Research System. [Online]. Available: https://www.thinksrs.com/downloads/pdfs/manuals/DG535m.pdf.

[41] Model SR510 Lock-In Amplifier, Stanford Research System. [Online]. Available: https://www.thinksrs.com/downloads/pdfs/manuals/SR510m.pdf.

[42] F. Gounand, "Calculation of radial matrix elements and radiative lifetimes for highly excited states of alkali atoms using the coulomb approximation.," *Journal de physique Paris*, vol. 40, 5 1979, ISSN: 03020738. DOI: 10.1051/jphys:01979004005045700.

[43] T. Zhou, B. G. Richards, and R. R. Jones, "Absence of collective decay in a cold rydberg gas," *Physical Review A*, vol. 93, 3 2016, ISSN: 24699934. DOI: 10.1103/PhysRevA.93.033407.

[44] S. Greenland, S. J. Senn, K. J. Rothman, *et al.*, "Statistical tests, p values, confidence intervals, and power: A guide to misinterpretations," *European Journal of Epidemiology*, vol. 31, pp. 337–350, 4 Apr. 2016, ISSN: 15737284. DOI: 10.1007/s10654-016-0149-3.

[45] M. Jing, Y. Hu, J. Ma, *et al.*, "Atomic superheterodyne receiver based on microwave-dressed rydberg spectroscopy," *Nature Physics*, vol. 16, 9 2020, ISSN: 17452481. DOI: 10.1038/s41567-020-0918-5.

[46] D. H. Meyer, Z. A. Castillo, K. C. Cox, and P. D. Kunz, "Assessment of rydberg atoms for wideband electric field sensing," *Journal of Physics B: Atomic, Molecular and Optical Physics*, vol. 53, p. 034 001, 3 Feb. 2020, ISSN: 0953-4075. DOI: 10.1088/1361-6455/ab6051.

[47] BC106N-VIS/M - CCD Camera Beam Profiler, Thorlabs Inc. [Online]. Available: https://www.thorlabs.com/thorproduct.cfm?partnumber=BC106N-VIS/M.

[48] A. Lindgård and S. E. Nielsen, "Transition probabilities for the alkali isoelectronic sequences li i, na i, k i, rb i, cs i, fr i," *Atomic Data and Nuclear Data Tables*, vol. 19, no. 6, pp. 533–633, 1977, ISSN: 0092-640X. DOI: 10.1016/0092-640X(77)90017-1.

Appendices

Appendix A

Laser operation, troubleshooting and beam profile

A.1 Operation and troubleshooting of ECDL

The ECDL setup has been discussed in the section 2.2, regarding of this internal structure and frequency control electronics. Here are some more details about how to identify any problems and then adjust the ECDL cavity. If one of the following frequency behavior is observed, then it means the ECDL laser needs to be taken into service.

The ECDL is designed to be free of mod hops (i.e change of N), which is achieved by choosing a well-designed pivot point that makes sure the incidence angle θ_d and the cavity length L as correlated as Eq. 2.1. The mode hop shown in Fig. A.1 is a sign of the pivot point of tuning element (holding the prism) not in the design position. So when the voltage on piezo is increasing, Eq. 2.1 is not met with the same N, resulting in a frequency jumping.

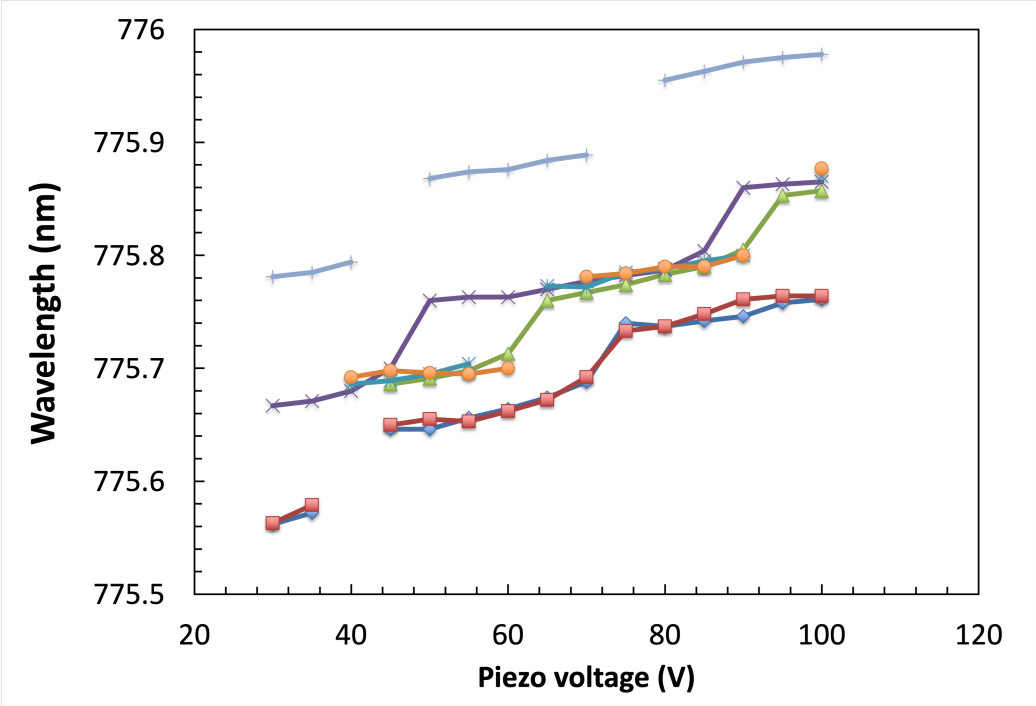

Figure A.1: Wavelength of the output laser beam vs the piezo voltage from a malfunctioning ECDL. Different color line demonstrate the frequency response when the piezo voltage is changing continuously from 30V to 100V or vice versa. The main reason of such non-linear response vs the piezo voltage is due to mode hopping between different N.

The solution for this abnormality is to remount the reflecting prism on the tuning element and then test the frequency response until the frequency vs voltage response behavior is back to normally. Such process is tedious and time consuming. We figured out that, instead of remounting prism, there is an alternative way to solve this issue. We can connect the ECDL to a Lab Computer and then change the temperature setting of the entire laser. With lower or higher temperature, the relative position of different elements is changed, and then the pivot point can be moved into its designed position.

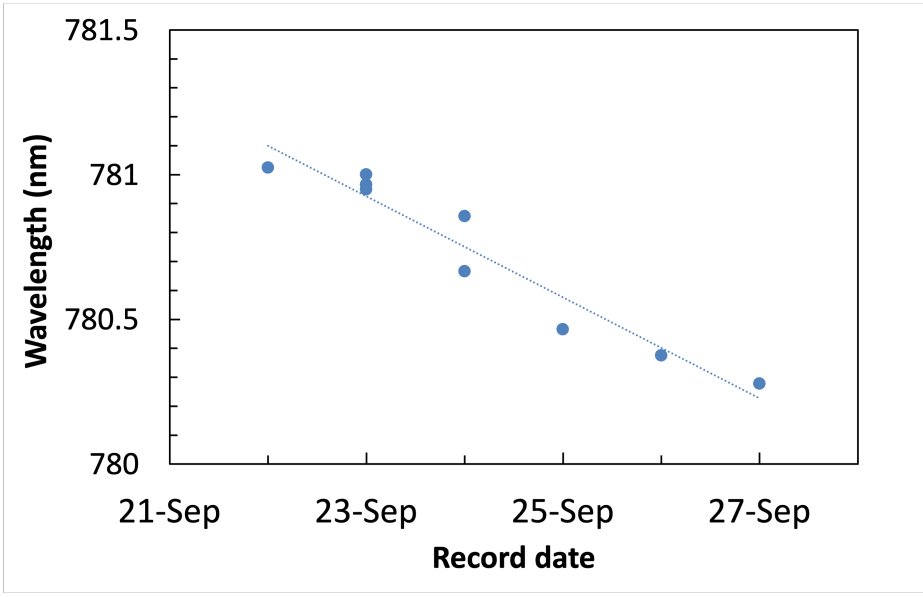

Figure A.2: Wavelength of the output laser beam vs the piezo voltage. The frequency of output laser beam is changing rapidly in days, which is main due to broken piezo, failing to adjust the external cavity length.

The frequency drift of the ECDL in Fig. A.2 is a sign of the cavity length being shorter over time. This is normally due to the mounting screws not fully tightened. Another possible reason is that the piezo is not holding the tuning element in the same position. Therefore a replacement of the piezo is required. In practice, our lab humidity can cause the ECDL frequency to jump up and down as well, but not fixed in one direction as shown here.

Unlike the ECDL in the SHG-pro system has a coarse tuning knob, the ECDL for 780nm laser does not have one. So when a large frequency drifting happens, and the piezo voltage (limited to 117.5V) is not able to compensate, it is required to open up the laser head and adjust the tuning element shown in Fig. 2.2. It is worth mentioning that the tightening of the skewers would cause a large change of the output laser wavelength (up to 0.1nm), which should be considered before manually changing the tuning element position.

A.2 Laser profile and Rabi Frequency

Microscope slides are used in the setup (Fig. 4.1) as beam splitters. The front and back end of the slides create two reflections of the incident beam, each of which has around 5% of the incident intensity (10mW). Due to back end reflected light passing across the slices twice, the beam power of the back-end reflection is smaller than the front end reflected beam. The final power into the Rubidium cell would be controlled by additional Neutral Density Filter (NDF),which has Optical Density (OD) from 1.0 to 5.0 by stacking multiple filterers. The coupling beam power goes up to 80mW and the probe beam power is around 1μW with OD 3.0 filter.

$$T(Transmission) = 10^{OD_{total}} \times 100\% \tag{A.1}$$

Thorlabs beam Profilers shows the size of the two beams and relative position of the balanced probe beam to the overlapped probe beam. The output-beam profile of the ECDL can be well approximated by an elliptical Gaussian function. The long axis is in vertical plane with half maximum intensity radius a and the short axis is in the horizontal plane with half maximum intensity radius b. The peak intensity of the beam, I_0, is related to the total power P in the beam by,

$$I_0 = \frac{PIn2}{\pi ab} \tag{A.2}$$

The probe laser Rabi frequency is 1.05MHz and the coupling laser Rabi frequency is 4.16MHz. These Rabi frequency numbers are calculated by,

$$\Omega = \frac{\vec{F}_{rf} \cdot \vec{d}}{\hbar} \tag{A.3}$$

where $\vec{F}_{rf} = \sqrt{\frac{2I_0}{c\epsilon_0}}$ is the vector electric field amplitude and $\vec{d}$ is the Rydberg transition dipole moment.

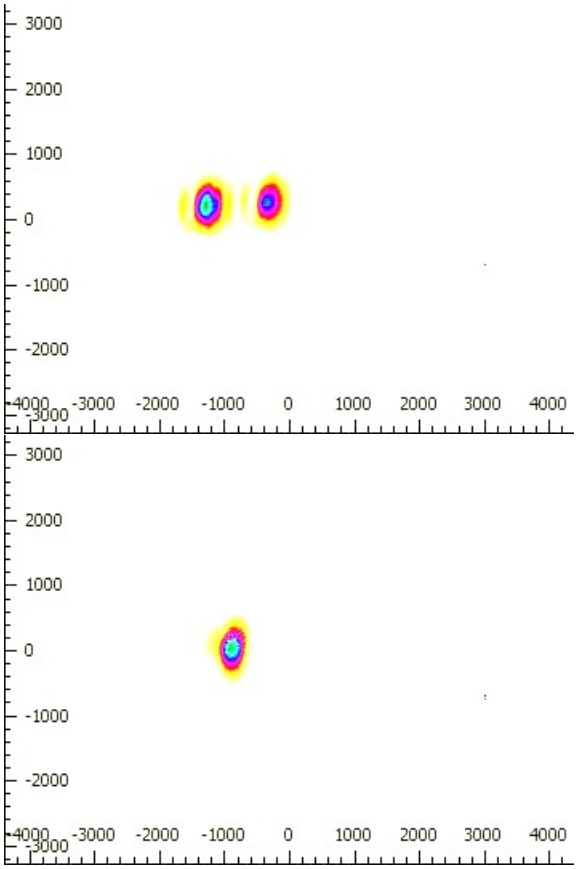

Figure A.3: The couple laser and probe laser beam profile by Thorlabs Beam Profilers 7.0[47]. The number listed in the graph are in units of μm. Upper figure presents the probe laser into the Rubidium cell with two parallel beams. One is the signal beam (beam radius at half intensity maximum is 0.22mm at major axis and 0.15mm at minor axis), and the other is the background reference. Two beams are separated. Bottom figure presents the couple beams into the Rubidium cell (size is 0.17mm at major axis and 0.12mm at minor axis), which is overlapped with the right probe beam in the upper figure.

The ^{85}Rb transition dipole moment from $5S_{1/2}$ to $5P_{3/2}$ is $1.717ea_0$[48], while the dipole moment from $5P_{3/2}$ to $25S_{1/2}$ is $0.021ea_0$ and from $5P_{3/2}$ to $32S_{1/2}$ is $0.013ea_0$[7], in the condition of linearly polarized probe and coupling laser.

Appendix B

Power interference analysis

In this appendix, more experiment results are provided to show the DC power and RF power supply interference. As the Experiment Chapter shows, with a RF field in present, the DC voltage on the plate is varying, thus causing the different measured RF values when using different equation(s). In the section 4.2.6 with the RF antenna setup, the interference is significantly reduced, and the best solution to derive the accurate amplitude reading is to assume the DC field amplitude is unknown as well as shown in section 4.3.

To further demonstrate this interference between two power supplies, different RF power sources and DC power sources are used in the following test. We named the IntraAction frequency synthesizer as the strong RF supply one (RF1) and the Wavetek generator as the weak RF supply two (RF2), according to their max power output. The same DC1/DC2 is used to name the two DC power supplies, HP 6286A and BK precision 1171.

Both RF supplies and DC supplies are wire-connected to the internal plates. In between RF supply and metal plates is the a $4.7\mu F$ capacitor. In between DC supply and metal plates are several clip-on ferrite rings, as shown in Fig. 2.16. RF frequency is set at 80MHz for both RF supplies, while DC reference voltage out the supplies is set at 5.5V monitored by a voltmeter. During the measurement, DC supplies need constant adjustments to sustain at 5.5V.

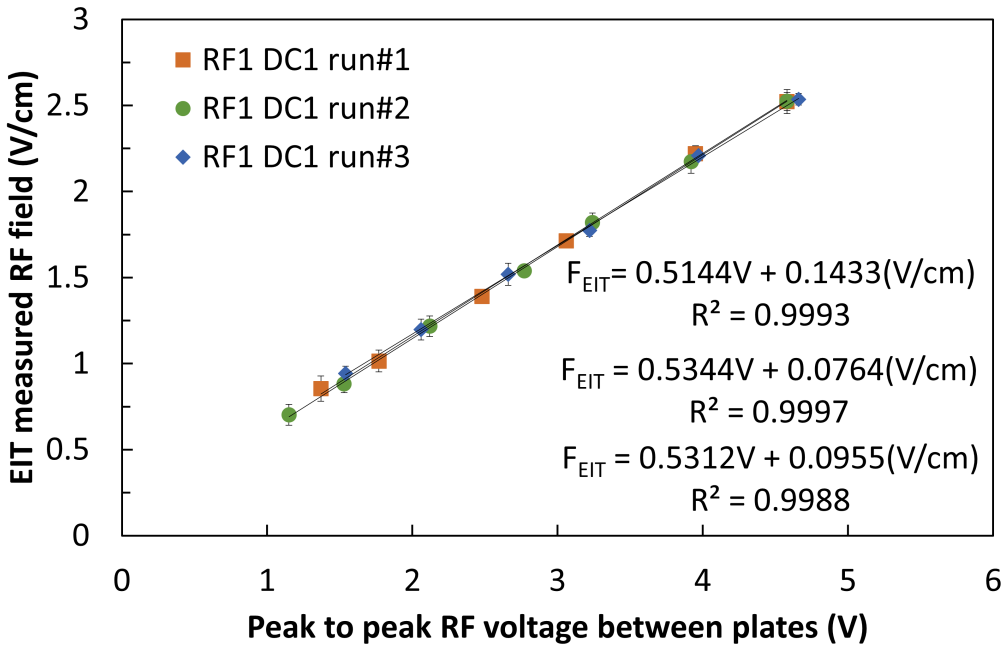

Figure B.1: EIT measured RF field vs RF voltage between the internal plates. This measurement is done with the RF1 and DC1.

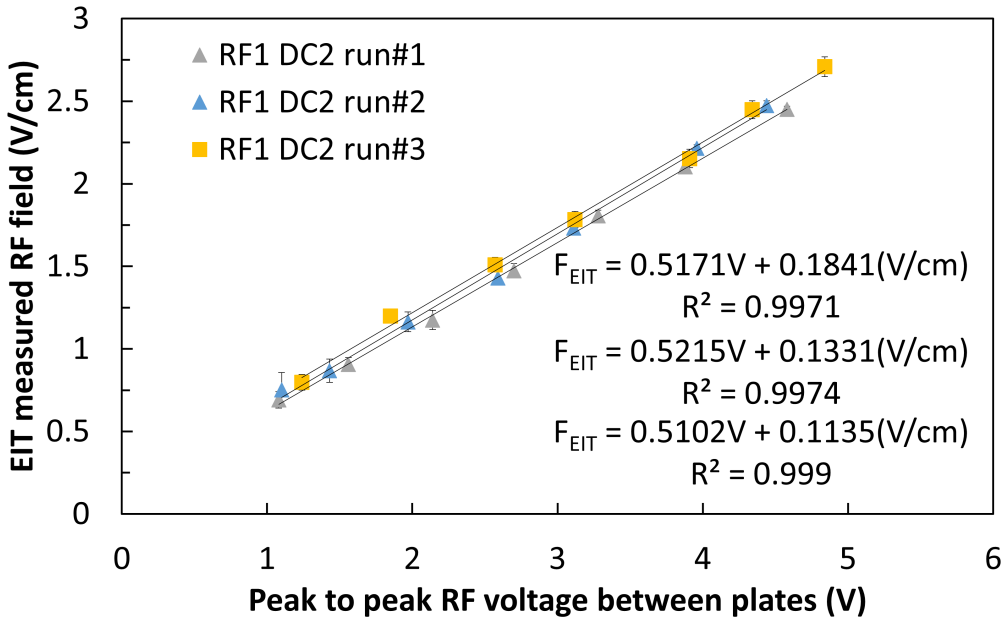

Figure B.2: EIT measured RF field vs RF voltage between the internal plates. This measurement is done with the RF1 and DC2.

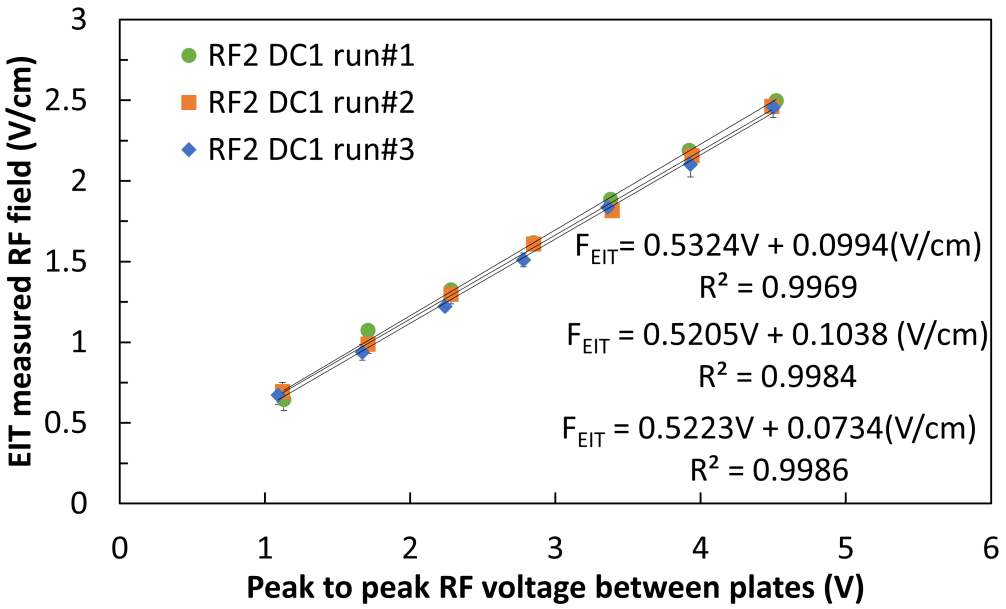

Figure B.3: EIT measured RF field vs RF voltage between the internal plates. This measurement is done with the RF2 and DC1.

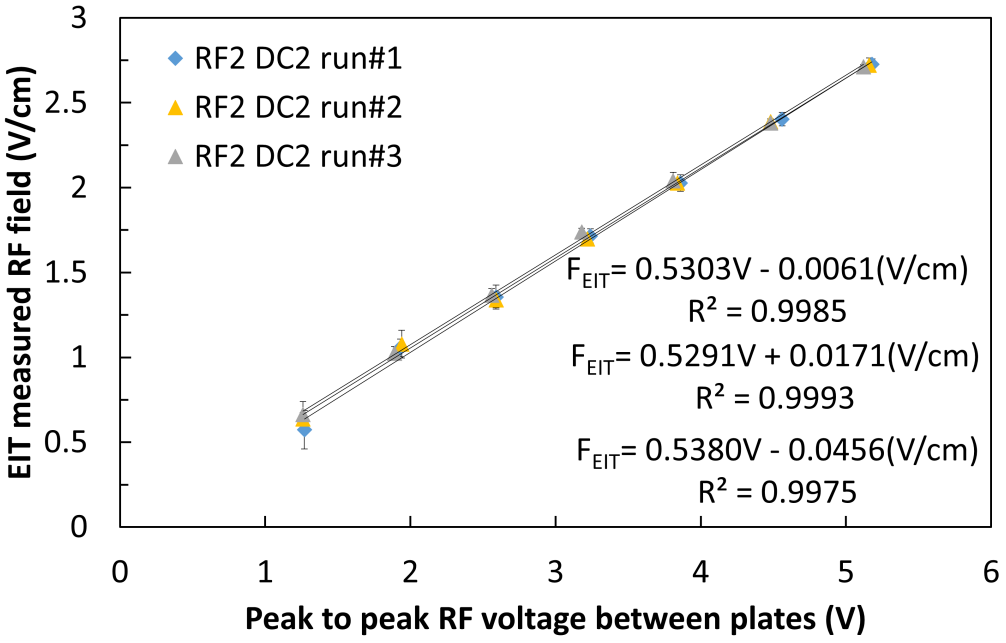

Figure B.4: EIT measured RF field vs RF voltage between the internal plates. This measurement is done with the RF2 and DC2.

The results and the linear fittings are shown in these four plots. In the fitting plots with DC1, the different RF supplies give the similar y-intercepts and slopes, which are overlapped with range of measurement error if plotted together. This DC1 power supply therefore is chosen for all the experiment in the result chapter. The DC2 power supply, in contrast, shows different y-intercepts, as the RF1 DC2 configuration gives the largest y-intercept while the RF2 DC2 configuration gives the smallest y-intercept. The latter is negligible if taking the p-test. This comparison suggests that RF field derived from reference by DC2 depends different RF power supplies. And the RF1 DC2 configuration gives the largest deviation between each run, suggesting the largest voltage fluctuation from DC2. We choose to not use this BK 1171 for other experiments.

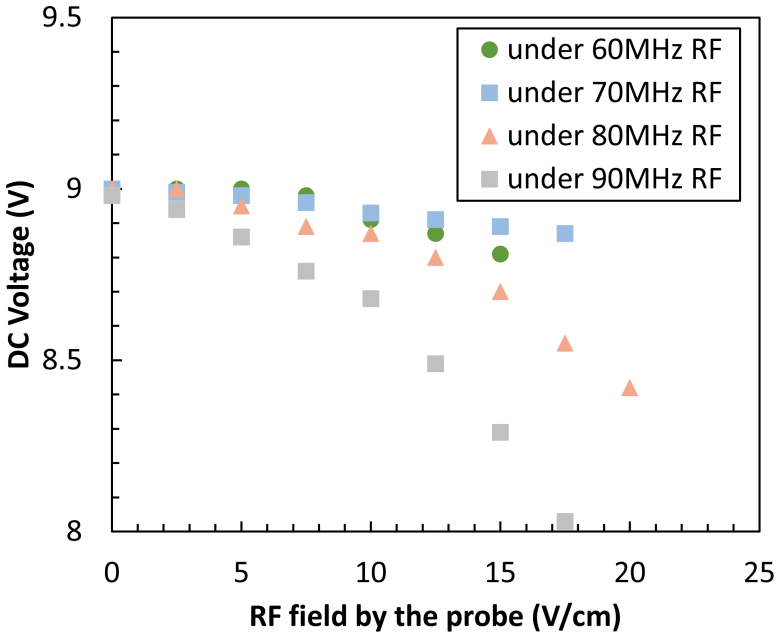

Figure B.5: DC supply voltage output vs RF field by the probe on the plates. DC voltage is set to be 9V with no RF field in present. Then the DC supply output level remains unaltered when the RF field slowly increases. The DC voltage starts to decrease with different amount under different frequency RF fields. The uncertainty in the measured voltage is smaller than the plotted symbol size.

The interference between RF and DC supplies requires constant monitoring the DC voltage from voltmeter and then readjusting. Even with such operation, the DC voltage measured on the plate is not equal to the DC field solved from Eqs. 4.5 (see Figs.4.31 and 4.33).

In conclusion, this appendix shows the importance of determination the reference field amplitude as well as the signal RF field in a single measurement as demonstrated in section 4.3, in the F_{rf} amplitude range explained in Fig. 5.1.